

https://dspace.org/

Electrocatalytic detection of biomarkers of tuberculosis and cervical cancer

Peteni, Siwaphiwe

2024-07
University of the Witwatersrand, Johannesburg
https://hdl.handle.net/10539/45457
Peteni, Siwaphiwe. (2024). Electrocatalytic detection of biomarkers of tuberculosis and cervical cancer. [PhD thesis, University of the Witwatersrand, Johannesburg. WIReDSpace. https://hdl.handle.net/10539/45457

Downloaded from a DSpace repository. https://dspace.org/

Electrocatalytic detection of biomarkers of tuberculosis and cervical cancer



UNIVERSITY OF THE
WITWATERSRAND,
JOHANNESBURG

Siwaphiwe Peteni

A thesis submitted to the Faculty of Science, University of the Witwatersrand, Johannesburg,

in fulfilment of the requirements for the degree of

Doctor of philosophy in Chemistry

Supervisor: Prof. Kenneth I. Ozoemena

July 2024

Declaration

I solemnly declare that this thesis is my own work. It is being submitted for the Degree of Doctor of Philosophy at the University of the Witwatersrand, Johannesburg. It has not been submitted before for any degree or examination at any other University.

Signature: …S.Peteni…… Date: 31 July 2024……

Dedication

This thesis is dedicated to my family who have been the pillar of strength since the beginning of this study.

Acknowledgements

First, I would like to thank God for the gift of life and for giving me this opportunity to do my PhD. I learnt that indeed those who put their trust in Him do not faint, but they soar high on wings like eagles **ISAIAH 40:31**.

I would like to extend my utmost gratitude to my supervisor Professor Kenneth Ozoemena who gave me an opportunity to work with him. I would like to thank him for his tireless contribution to my work, without his guidance I wouldn't have travelled thus far. Thank you for simplifying and guiding my wild ideas, shaping them and making them more sounding. I would like to thank Dr Oluwafunmilola Ola, Dr Frankie Rawson from the university of Nottingham and Prof Leshweni J. Shai from the university of Tswane for giving me an opportunity to work with them, and for sponsoring my HPV based research.

I would like to thank my colleagues/ group (MEET), I will not mention each by name as there are many to name. I would like to thank them for their endless advice, for making the laboratory a fun place to work in and mostly for sharing scientific knowledge. I would like to thank Celestine Ozoemena for training me on how to fabricate immunosensors. I would like to thank Patrick Mwonga for computational modelling. The CATMAT group for the scientific impartation of knowledge, I thank you. I would like to thank Prof Nil Coville for allowing me to use his microwave and furnance at the initial stages of my work. I would like to thank Prof Caren Billing who allowed me to use her instrument MVP300, to run my electrochemistry experiments. I would like to thank Prof Rudolph Erasmus for running Raman spectroscopy for me. I would like to thank the MMU team for training me on how to use SEM and XRD. I would like

to thank NMMISA for running my XPS. The cenetr of computational modelling in Cape town is also acknowledged. The university of Western cape for running my HRTEM.

I would like to thank my family for their tireless prayers and constant check-ups, especially my mom. I would like to thank my friend Sivuyisiwe Mapukata for the push and the encouragement and many of my friends which I did not mention by name. Lastly, I would like to thank Sinawo Landzela, for his support.

To the National Research Foundation (NRF) and the Department of Science and Innovation (DSI) for funding this three-year programme under Freestanding, Innovation and Scarce Skills Development Fund PhD scholarship and for one PhD extension programme. The University of Nottingham via the Global Challenges Research Fund scheme for funding some of the research.

Research outputs

1. Kenneth I. Ozoemena, Suhail Musa, Refiloe Modise, Adewale K. Ipadeola, Lesego Gaolathle, **Siwaphiwe Peteni**, Guy Kabongo, Fuel cell-based breath-alcohol sensors: Innovation-hungry old electrochemistry, Current Opinion in Electrochemistry 10, 82 - 87 (**2018**)
2. **Siwaphiwe Peteni**, Okoroike C. Ozoemena, Tobileo Khawula, Aderemi B. Haruna, Frankie J. Rawson, Leshweni J. Shai, Oluwafunmilola Ola, Kenneth I. Ozoemena*,* Electrochemical Immunosensor for Ultra-Low Detection of Human Papillomavirus Biomarker for Cervical Cancer**,** ACS Sensors 8 (7), 2761–2770*,* (**2023**)
3. **Siwaphiwe Peteni**, Thapelo P. Mofokeng, Aderemi Haruna, Patrick Mwonga, Kenneth I. Ozoemena, Metal organic framework derived cobalt nanoparticles confined in carbon matrix for an indirect detection of tuberculosis biomarker methyl nicotinate (in progress)

Conferences

1. **Siwaphiwe Peteni**, Kenneth Ozoemena, Electrochemical detection of volatile organic compounds of tuberculosis using metal organic framework derived carbon. 70th Annual Meeting of the International Society of electrochemistry ISE), Durban, South Africa, August 2019 (poster presentation)

2. **Siwaphiwe Peteni**, Kenneth Ozoemena, Electrochemical detection of volatile organic compounds of tuberculosis using metal organic framework derived carbon. Energy Storage and Industry 4.0: Challenges and prospects (ENSTIN 2019), Pilanesburg, South Africa, July 2019 (poster presentation)

3. **Siwaphiwe Peteni**, Okoroike C. Ozoemena, Aderemi B. Haruna, Frankie Rawson, Leshweni J. Shai, Oluwafunmilola Ola, and Kenneth I. Ozoemena, Electrochemical detection of Human papilloma virus as a biomarker for cervical cancer, 33rd International CATSA conference, Mossel Bay, South Africa, 2023 (poster presentation)

Professional organisations

1. Member, South African Chemical Institute.
2. Member, International Society of Electrochemistry

Awards, honours, and prizes

1. Awarded NRF freestanding and innovation Doctoral scholarship, 2018-2020.
2. Awarded NRF freestanding and innovation Doctoral scholarship extension, 2021.

ABSTRACT

The need for simpler, low cost and efficient diagnostic methods remains a matter of urgency. This has opened numerous streams of research. Electrochemistry is a simple, cost effective and efficient method that has been used for the detection of several diseases such as tuberculosis (TB) and human papilloma virus (HPV). TB has been ranked amongst the most problematic diseases in HIV/AIDS burdened communities, this alone calls for concern. Biomarkers of TB not only indicate *mycobacterium* infection but can also assist in the early detection of TB which is highly beneficial for the infected person and the health care system. HPV is the causative agent for cervical cancer. Cervical cancer is ranked as the fourth disease that causes mortality amongst women. With that in mind, HPV-16 L1 early detecting means possible early detection of cervical cancer.

In this thesis, methyl nicotinate (MN), which is one of TB's biomarkers was detected in phosphate buffer solution (PBS, pH 6.0) and commercial human serum using cobalt nanoparticles supported on carbon derived from trimesic acid (TMA) (abbreviated as Co-NPs@C_{TMA}) and biphenyldicarboxylic acid (BPDC) (abbreviated as Co-NPs@C_{BPDC}) as electrocatalysts. These electrocatalysts were obtained using microwave-assisted metal-organic framework process with TMA and BPDC as ligands. XRD data showed that these electrocatalysts are cobalt nanoparticles with dominant {111} and {200} phase with traces of cobalt oxide (CoO). XPS and Raman data showed that Co-NPs@C_{BPDC} is defect-rich compared to the Co-NPs@C_{TMA} counterpart. BET showed that Co-NPs@C_{BPDC} has higher surface area and pore size and volume than the Co-NPs@C_{TMA} catalyst. Both electrocatalysts showed reversible cobalt nanoparticle oxidation and reduction reactions, in the absence and in the presence of the MN, thereby

allowing for a facile indirect electrochemical detection of this biomarker. The calibration curves showed low limit of detection (LoD) of 0.47 and 0.147 µM for Co-NPs@C_{TMA} and Co-NPs@C_{BPDC}, respectively. The higher performance of the latter is attributed to its enhanced physico-chemical properties compared to the former.

Next, HPV-16 L1, which is the conventional high-risk antigen that is present in cervical cancer, was detected using onion-like carbon (OLC) and polyacrylonitrile fibre integrated with OLC (OLC-PAN) as electrode platforms. Two electrode platforms were used; onion-like carbon (OLC) and its polyacrylonitrile (OLC-PAN) composites. Both platforms led to the detection in a wide linear concentration range (1.95 fg/ml to 50 µg/ml), excellent sensitivity (>5.2 µA/log([HPV-16 L1, fg/mL]) and ultra-low detection of *ca*. 1.0 and 1.4 fg/ml for OLC-PAN and OLC-based immunosensors, respectively. The high specificity of detection was proven by experimenting with an anti-Ovalbumin antibody (anti-Ova) and native Ovalbumin protein (Ova). An immobilized antigenic HPV-16-L1 peptide showed insignificant interaction with anti-OVA in contrast with the excellent interaction with anti-HPV-16 LI antibody. The immunosensors showed satisfactory stability of ~ 3 days of re-usability. The application of the immunosensor as a potential point-of-care diagnostic (PoC) device was investigated with the screen-printed carbon electrode which showed the ability to detect ultra-low (~ 0.7 fg/ml) and high (~ 12 µg/ml) concentrations. This study opens the door of opportunity for further investigation with other electrode platforms and realization of PoC diagnostic devices for screening and testing of HPV biomarker for cervical cancer.

Content

DECLARATION	**i**
DEDICATION	**ii**
ACKNOWLEDGEMENTS	**iii-iv**
RESEARCH OUTPUTS	**v**
CONFERENCES	**v-vi**
PROFESSIONAL ORGANIZATION	**vi**
AWARDS	**vii**
ABSTRACT	**viii-ix**
LIST OF FIGURES	**xv-xix**
LIST OF TABLES	**xx**
LIST OF SCHEMES	**xxi**
LIST OF SYMBOLS	**xxii**
LIST OF ABBREVIATIONS	**xxiii-xxvi**

Table of contents

Chapter one

1.1 Introduction 1

1.1.1 Background and motivation 1-7

1.1.2 Aim 8

1.2 Objectives 8

1.2.1 Objectives 8

1.2.2 Objectives 8-9

1.3 Outline of the thesis 9-10

Chapter Two

Literature review

2.1 Introduction 11

2.1.1 Sensors 11-14

2.1.2 Sensitivity 15

2.1.3 Limit of detection (LOD) and limit of quantification (LOQ) 15

2.1.4 Selectivity 15

2.2 Electrocatalysts 15

2.2.1 Metal organic framework 16-18

2.2.2 Synthesis methods of MOFs 19

2.2.3 Microwave assisted synthesis (MAS) 19-21

2.2.4 Metal organic framework as sacrificial templates 22-24

2.2.5 Onion like carbon 24

2.2.6 Synthesis of OLC 25-29

2.2.7 PAN fibers/carbon nanofibers 30-31

2.2.8 Synthesis of CNFs 31-34

Chapter Three

Experimental methods and characterization techniques

3.1. Experimental 35

3.1.1. Material 35-36

3.1.2. Synthesis of metal-organic framework (Co-MOF) and cobalt nanoparticle derived carbon (Co-NPs@C_{TMA} and Co-NPs@C_{BPDC}) 36-37

3.2 Synthesis of Onion like carbon (OLC) and onion like carbon/polyacrylonitrile composite (OLC-PAN) 38

3.2.1 Synthesis of OLC 38

3.2.2 Synthesis of OLC-PAN 38

3.3 Characterization techniques 40

3.3.1 Powder x-ray diffraction (PXRD) 40

3.3.2 X-ray photoelectron spectroscopy (XPS) 40

3.3.3 Raman spectroscopy 40-41

3.3.4 Scanning electron microscopy (SEM) and energy dispersive x-ray spectroscopy (EDX) 41

3.3.5 High Resolution Transmission electron microscopy (TEM) 41

3.3.6 Brunauer-Emmett-Teller (BET) 42

3.4 Density functional theory (DFT) 42-43

3.5 Experimental details for Electrochemical Measurements 43

3.5.1 Electrode modification 43-44

3.5.2 Cyclic voltammetry (CV) 45-46

3.5.3 Square wave voltammetry (SWV) 46

3.5.4 Differential pulsed voltammetry (DPV) 46-47

Chapter Four

Electrochemical detection of methyl nicotinate

4.1. Brief introduction 48

4.2 Characterization 49

4.2.1 XRD of Co-MOF TMA, Co-MOF BPDC, Co-NPs@C_{TMA} and, Co-NPs@C_{BPDC} 49-50

4.2.1.1 Raman of Co-MOF TMA, Co-MOF BPDC, Co-NPs@C_{TMA}, and Co-NPs@C_{BPDC} 51-53

4.2.2 X-ray photoelectron spectroscopy (XPS) 54-55

4.2.3 Scanning electron microscope (SEM) 56

4.2.4 Energy dispersive x-ray microscope (EDX) 57

4.2.5 High resolution transmission microscopy (HRTEM) 57-59

4.2.6 Surface area and pore volume 60

4.3 Density functional theory (DFT) calculations

4.3.1 Predicting of electrochemical interaction of Co {111}{200} towards MN 61-65

4.4 Electrochemical studies

4.4.1 Voltammetric responses in ferri/ferro-cyanide 66-72

4.5 Methyl nicotinate detection

4.5.1 Cyclic voltammetry 72-75

4.6 Limit of detection 75-77

4.6.1 Selectivity studies 78-79

4.7 Preliminary gas sensing 82-84

4.8 Conclusion 84-85

Chapter Five

Electrochemical detection of HPV 16-L1

5.1 Brief introduction 86

5.2.1 Physicochemical characterization 85

5.2.2 TEM and SEM Characterisation 86-87

5.2.3 X-ray diffraction and raman spectroscopy 87-88

5.2.4 Surface analysis 88

5.2.5 XPS 88-90

5.3 Cyclic voltammetry

5.3.1 mass transport and electrode kinetics 90-93

5.4 Electroanalytical Performance of the Immunosensors Towards HPV-16 L1 93-100

5.5 Specificity studies and sensor re-usability 100-102

5.6 Proof of concept 102-103

5.7 Conclusion 103-104

Chapter Six

Conclusion and recommendations

6.1 Conclusion 105-106

6.2 Recommendations 106-107

References 108-129

List of figures

Figure 2.1: Components of a sensor and the analytes that could be used

Figure 2.2: Three electrode setup

Figure 2.3: Shows the connection between the metal node and ligand

Figure 2.4: Shows the different ligands that can be used for MOF synthesis **Figure 2.5**: Different synthetic routes of MOFs

Figure 2.6: Electromagnetic waves generated during microwaving

Figure 2.7: Conventional heating vs microwave heating

Figure 2.8: Different materials that can be derived from MOFs

Figure 2.9: Metal organic framework derived cobalt oxide on carbon Co_3O_4@C) and metal nanoparticles on carbon

Figure 2.10: OLC synthesized by different methods

Figure 2.11: Structural transformation of ND to OLC

Figure 2.12: Functional groups that can be introduced on the surface of OLCs (A) and (B) doping of OLCs

Figure 2.13: Differences between CNFs and CFs

Figure 2.14: Different types of CNFs

Figure 2.15: Basic electrospinning setup

Figure 2.16: Different electrospun nanofibers with their applications

Figure 3.1: Shows (A) Cobalt metal organic framework (Co-MOF BPDC) and (B) Co- MOF TMA

Figure 3.2: Snapshots of the biomolecules as received it their delivered package
Figure 3.3: Prepared concentrations of HPV-16 L1 antigen (from the highest to lowest concentration)
Figure 3.4: Three electrode set-up
Figure 4.1: X-ray diffraction of parent MOFs (A) Co-MOF TMA and (B) Co-MOF BPDC, (C) Co-NPs@C_{BPDC} and (D) Co-NPs@C_{TMA}
Figure 4.2: Raman spectra of (A) Co-MOF TMA, (B) Co-MOF BPDC, (C) Co-NPs@C_{BPDC} and, (D) Co-NPs@C_{TMA}
Figure 4.3: Deconvoluted spectras of (A) and (B) Co2p of Co-NPs@C_{TMA} and Co-NPs@C_{BPDC}, (C) and (D) O1s of Co-NPS@C_{TMA} and Co-NPs@C_{BPDC}, respectively and (E) and (F) C1s of Co-NPs@CTMA and Co-NPs@CBPDC, respectively
Figure 4.4: Scanning electron microscope images of (A) Co-MOF TMA (B) Co-MOF BPDC, (C) Co-NPs@C_{TMA}, (D) Co-NPs@C_{BPDC}, respectively
Figure 4.5: Energy dispersive x-ray spectra of (A) Co-MOF TMA, and (B) Co-NPs@CTMA
Figure 4.6: High resolution transmission microscopic images of (A) Co-NPs@$C_{TMA,}$ (C) Co-NPs@C_{BPDC} at 50 nm and, (B) Co-NPs@C_{TMA} with (I) and (II) fft and its corresponding inverse fft and (D) Co-NPs@C_{BPDC} with (III) and (IV) fft and its corresponding inverse fft at 5 nm, respectively

Figure 4.7: Isosurface Potentials@+/- 0.039564 isovalue(a.u.), {blue (+) and red (-) shades for Methyl nicotinate Oxygen has higher –ve potential compares to Nitrogen

Figure 4.8: Adsorption sites of methyl nicotinate at the surfaces of Co{111} and Co{200}.

Figure 4.9: Partial density of states of Co{111}; (A) and, (B) before adsorption of MN and, (C) and (D) after adsorption of MN and, of Co{200}; (E) and, (F) before adsorption of MN and (G) and (H) after adsorption of MN, respectively.
Figure 4.10: D-band centres of Co{111} and Co{200}
Figure 4.11: Cyclic voltammograms of the modified electrodes in 3mM $[Fe(CN)6]^{3/4}$in 0.1 M KCl at 20 mVs^{-1}.
Figure 4.12: Scan rate studies of (A) bare GCE electrode, (B) GCE-CoMOF TMA, (C) GCE-CoMOF BPDC, and υ vs current plots D) bare-GCE, (E)

GCE CoMOF TMA, (F) GCE-CoMOF BPDC, and log υ vs log current plots (G) bare-GCE, (H) GCE-CoMOF TMA, (I) GCE- CoMOF BPDC, respectively

Figure 4.13: Scan rate studies of (A) GCE-Co-NPs@C_{TMA}, (B) GCE-Co-NPs@C_{BPDC}, and υ vs current plots of (C) GCE-Co-NPs@C_{TMA}, (D) GCE-Co-NPs@C_{BPDC} and, log(υ) vs log(current) plots (E) GCE- Co-NPs@C_{TMA} and, (F) Co-NPs@C_{BPDC}, respectively, in 3mM $[Fe(CN)6]^{3/4}$ in 0.1 M KCl

Figure 4.14: Comparative cyclic voltammograms of (A) Co-NPs@C_{BPDC} in PBS and, in MN and, (B) Co-NPs@C_{TMA} in PBS and MN, at 20 mV/s and, (C) Co-NPs@C_{BPDC} and Co-NPs@C_{TMA} in MN solution of pH 6 at 50 mV/s

Figure 4.15: Scan rate studies of MN (A) Co-NPs@CTMA (B) Co-NPs@CBPDC (C) scan rate vs current plot of Co-NPs@CTMA or Co-NPs@CBPDC (D) log(scan rate) vs potential plots of Co-NPs@CTMA or Co-NPs@CBPDC, respectively.

Figure 4.16: Concentration studies of MN using differential pulsed voltammogram for (A) Co-NPs@CTMA and its concentration vs change in current plot (B), and (C) Co-NPs@CBPDC and its concentration vs change in current plot (D), respectively.

Figure 4.17: Differential pulsed voltammogram of MN, AA and UA (A) Co-NPs@CTMA, and (B) Co-NPs@CBPDC

Figure 4.18: Gas sensing set up for detection of MN

Figure 4.19: Scan rate studies of (A) CSPE (black, with MN), and CSPE- (red, with MN) (B) Scan rate studies of CSPE-Co-NPs@CBPDC with MN

Figure 4.20: Linear scanning voltammogram showing the concentration studies of Co-NPs@CBPDC

Figure 5.1: TEM images of (A) OLC and (B) OLC-PAN, SEM images of (C) OLC and (D) OLC-PAN

Figure 5.2: XRD of (A) OLC, OLC-PAN, and (B) raman spectra of OLC, OLC-PAN

Figure 5.3: (A) Wide scan spectra of OLC-PAN, and deconvoluted spectra of (B) C1s, (C) O1s and (D) N1s of OLC-PAN.

Figure 5.4: Comparative cyclic voltammogram of bare-GCE (pink), GCE-OLC (red) and GCE-OLC-PAN (blue) at 50 mV/s in 0.1 mM of $Fe(CN)6]^{4-}$/$[Fe(CN)6]^{3-}$) and 3mM KCl

Figure 5.5: Scan rate studies of bare-GCE (A) and GCE-OLC (E) and GCE-

OLC-PAN (G) with plots anodic current vs scan rates (B), (E), (H) and log anodic current vs log scan rate (C), (F) and (I), respectively
Figure 5.6: A typical fabrication pathway for HPV-16 L1 immunosensors. The reagents in each path are identified in the experimental section
Figure 5.7: Comparative cyclic voltammograms of (A) GCE-OLC, GCE-OLC-Ab-BSA, and GCE-OLC-Ab-BSA-Ag, and (B) GCE-OLC-PAN, GCE-OLC-PAN-Ab-BSA, GCE-OLC-Ab-BSA-Ag at 50 mV/s

Figure 5.8: (A) Concentration studies of HPV-16 L1 (Ag) and (B) linear plot of change in current vs log [HPV-16 L1]
Figure 5.7: (A) shows concentration studies of Anti- HPV 16 L1, (B) shows linear plot of change in current vs log [Anti-HPV 16 L1].
Figure 5.9: (A) Square wave voltametric responses of GCE-OLC-PAN-OvaAb-BSA towards Ova-antigen ($7.8x10^{-15}$ fg/ml) and HPV-16 L1 antigen ($7.8x10^{-15}$ fg/ml), (B) Bar chart describing the responses of HPV-16-L1 antibody towards HPV-16 L1 ($7.8x10^{-15}$ fg/ml) after detection-stripping cycles.*reg means the regeneration of the surface.
Figure 5.10: (A, B**) Set-up of a s**creen-printed carbon electrode (SPCE) modified with HPV-16 L1 antibody immunosensor, (B) typical square wave voltammetric responses towards antigenic HPV-16 L1.

List of tables

Table 4.1: BET surface area of Co-NPs@C_{TMA} and Co-NPs@C_{BPDC}

Table 4.2: Summary of electrochemical parameters of electrodes in 3mM $[Fe(CN)6]^{3/4}$ in 0.1 M KCl

Table 4.3: Comparative studies MN-based studies with literature

Table 5.1 : Summary of CV parameters of bare-GCE, GCE-OLC and GCE-OLC-PAN

Table 5.2: summary of CV parameters of GCE-OLC and GCE-OLC-PAN sensor platforms.

Table 5.3: reports on the values obtained in this work in comparison to literature

List of schemes

Scheme 2.1: The reaction mechanism for the reaction involved in the formation of MOF

Scheme 3.1: Synthesis methodology of Co-MOF BPDC which was converted to Co-NPs@C_{BPDC}

List of symbols

^{o}C – Degree celsius

M – Molar

Ω – Ohms

cm – Centimeter µL – microliter mM – millimolar

∆Ep -change in electrode potential

∆G – Gibbs energy C – Coulomb

Ʊ – Scan rate

F – Faraday’s constant T – Temperature

K – Kelvin

R – Universal gas constant µA – microAmpere

fg – Femtogram

List of abbreviations

1D – 1dimensional

2D – 2dimensional

3D – 3dimensional

AA – Ascorbic acid

Ag/AgCl – Silver/silver chloride

AuE – Gold electrode

Al_2O_3 – Aluminium oxide

A.E- activation energy

B.E- binding energy

Amp – Amplitude

antiHPV 16 L1 - anti-HPV16 L1 antibody [Cam Vir 1] (anti-HPV-16)

antiOva - anti-Ovalbumin antibody

A – Ampere

B – Boron

BPDC – Biphenyl dicarboxylic acid

CCEI – cervical cancer elimination initiative

CE – Counter electrode

CFs – Carbon fibers

CIN – Cervical intraepithelial neoplasia

CNFs – Carbon nanofibers

$Co(NO_3).5H_2O$ – Cobalt nitrate

Co-TNA – Cobalt titania nanoarrays

CV – Cyclic voltammetry

CVD – Chemical vapor deposition

DFT – Density functional theory

DNA – Deoxyribonucleic acid

DMF - *N,N* dimethyl formamide

DPV – Differential pulsed voltammetry

eV – electron volt

EG – Ethylene glycol

ELISA – Enzyme-linked immunosorbent assay

EDC ethyl-3-(3-dimethylaminopropyl) carbodiimide

FC – Flow cytometry

GCE – Glassy carbon electrode

GC-MS – Gas chromatography and mass spectroscopy

h – Hour

hCG – Human Chorionic gonadotropin

HCl – Hydrochloric acid

HIV/AIDS – Human immunodeficient virus/acquired immunodeficient syndrome

HPV – Human papilloma virus

HRTEM – High-resolution transmission electron microscope

kV – kilovolts

L-M – Ligand to metal

LMICs – Low and middle income countries

LOD – Limit of detection

LOQ – Limit of quantification

LBPT - liquid-based pap test

MAS - Microwave assisted synthesis

min – Minute

MN – Methyl nicotinate

MOF – Metal organic framework

MW – Magnetic wave

KH_2PO_4 - Mono-potassium phosphate

N – Nitrogen

ND – Nanodiamonds

NHS - N-hydroxysuccinimide

Ova - Native Ovalbumin protein

OLC – Onion like carbon

PDOS – Partial density of state

POC – Point of care

PAN – Polyacrylonitrile

PBS – Phosphate buffer solution

PCR – Polymerase chain reaction

Pt – Platinum

PVA – Polyvinyl Alcohol

PVP- Polyvinylpyrrolidone

PXRD – Powder X-ray diffraction

HPV 16 L1 - Recombinant HPV-16 L1 protein (HPV-16)

RE – Reference electrode

RHE – Reversible hydrogen electrode

RIA–Radioimmunoassay

IHC -Immunohistochemistry

SEM – Scanning electron microscope

SPE – Screen printed electrode

SPGE – Screen printed graphite electrode

STDs- Sexually transmitted disease

SWV – Squarewave voltammetry

TB – Tuberculosis

TMA – Trimesic acid

UA – Uric acid

VIA - Visual inspection acetic acid

VOB – Volatile organic biomarkers

VOC – Volatile organic compound

WE – Working electrode

WHO – World Health Organization

XPS – X-ray photon spectroscope

Chapter one

Introduction

1.1 Introduction

This chapter gives a brief background on the scope of research covered during the period of the study, the rationale, aims, and objectives of this research. The aim of this work was achieved by two sectioned objectives.

1.1.1 Background and motivation

Public health plays a pivotal role in our societies, which are heavily burdened by communities that are battling with different diseases. Years after the discovery of a human immunodeficient virus and acquired immunodeficient syndrome (HIV and AIDs), it remains endemic with no known cure and no signs of slowing down. This remains a heavy burden to the health care system, particularly for children in Africa, the sub-Saharan region, and Asia, according to the global tuberculosis report [1,2]. HIV and AIDs are associated with a couple of opportunistic diseases, such as tuberculosis (TB), and sexually transmitted diseases (STDs), to name a few.

Tuberculosis (TB) is one of the most devastating poverty-associated diseases the world has ever seen. The effect of TB is mostly visible in sub-Saharan Africa. According to the World Health Organization (WHO), over 95% of TB deaths occur in low-and middle-income countries [3]. TB is said to be among the top 5 causes of death for women aged 15 and 44 and children. TB is the leading killer of HIV-positive.

patients; one in every three HIV deaths is associated with TB infection. Also, according to WHO, HIV-positive patients are 20 to 30 times more likely to develop active TB disease than HIV-negative people. In fact, it has been revealed that about 1.2 million new cases of TB amongst HIV-positive patients, 74% of them live in Africa. In 2021, TB was reported to be the second killing disease after COVID-19, with cases of 1.6 million people died in 2021 alone, according to the World Health Organization (WHO).

To “end TB”, WHO has an important TB elimination strategy known as the **“End TB Strategy”**. In this strategy, point-of-care (POC) early detection of TB is highly encouraged since a late detection of this disease has the potential to increase the chances of infecting other people. Early diagnosis of diseases is an essential tool for patient survival and treatment. One of the reasons why TB is regarded as a poverty-related disease is because it mostly affects people in disadvantaged communities where there is limited access to primary health care, which in turn poses a lot of problems in terms of diagnosis, management, and treatment. There is a pressing need for the development of diagnostic tools for early diagnosis of TB, which will be easy to handle, highly sensitive, low-cost and be able to reach disadvantaged communities. It is to be noted that TB diagnosis involves all the various aspects of clinical manifestation of the TB disease, ranging from latent and active TB to HIV/TB infection-infection, drug-resistant and extra-pulmonary TB. Many diagnostic tools have been used to diagnose to curb the spread; these include polymerase chain reaction (PCR), enzyme-linked immunosorbent assay (ELISA) and gene-Xpert etc; however, these techniques present some drawbacks such as the high cost and requirement of a stationery lab, the use of a highly sophisticated machinery and the use of a trained technician [4–6]. In the face of these challenges, there is a rising need to search for better.

alternatives for the diagnosis of TB. These alternative attempts must be cheap, simple, rapid, portable, selective, and sensitive for detection.

The conventional TB diagnosis involves the use of a blood sample. However, the use of exhaled human breath promises to revolutionise TB detection due to its attractiveness as an analyte for fast, non-invasive, POC diagnostics. Mycobacterium tuberculosis has been documented to give off four volatile organic compounds (VOCs) containing biomarkers known as (i) methyl nicotinate, (ii) methyl p-anisate, (iii) methyl phenylacetate, and (iv) o-phenyl anisole [7]. These VOBs can be detected on exhaled breath of TB-infected patients/persons. Interestingly, these four predominate TB VOBs are detectable even before the visual appearance of TB colonies in samples, which means that they could potentially been useful in the detection of latent TB infection. Volatile organic biomarker compounds (VOCs) containing biomarkers from exhaled breath presents a new platform for use as a specimen for the detection of TB. VOCs containing biomarkers result from oxidative stress or metabolism. These compounds may give clues about the profile of an individual's state of health. The gold standard analytical technique for detecting VOBs is gas chromatography integrated with mass spectroscopy (GC-MS) [8]. However, GC-MS is fraught with several disadvantages and high cost, POC-unfriendliness, high cost, and the need for highly skilled personnel and a controlled laboratory setting. On the other hand, electrochemical biosensing is a promising tool for early detection of various diseases, including TB.

Electrochemical sensing is more advantageous than the available diagnostic regimes for TB in that it is inexpensive, provides the needed POC, can be easily managed, is selective, does not require large amounts of sample to be tested, and operators need not be highly skilled [9]. Presently, the use of electrochemical methods for the detection of TB VOBs is hugely limited. Literature reports indicate that there are only

a few research groups that have worked on this study, Misra's group [10–12] and Banks' group [13], Bairagi et.al. [14] and Chen et.al. [15] and Willis et.al. [16]. The former [10–13] used a cobalt-modified titanium oxide nanotube array (Co-TNA) for the detection of the four TB-specific VOBs, while Banks' group [13] succeeded in detecting only two of the VOBs by using screen-printed graphite electrode (SPGE). Bairagi et.al used carbon film which was made from cobalt oxide nanoparticles on reduced graphene oxide, while Chen et.al used GCE modified with SnO_2 and La_2O_3 on reduced graphene oxide [14,15], Willies et al used SPE to detect MN and MPA, the SPE was used in an electroactive solution which contained copper and sodium chloride as a supporting electrolyte, it is believed that the two VOBs bind with the Cu, the oxidation state of Cu was used to monitor the reaction [16]. In a review by Ozoemena and Carrara [9], the authors clearly indicated that these existing preliminary studies provide an important step for future development of high-performance electrochemical breath-based diagnostics ("E-Breathnostic") for latent and active TB infections.

Human papillomavirus (HPV) is also an infection that increases in patients with HIV and AIDS, a sexually transmitted disease belonging to the papillomaviridae family. There are over 200 genomic species of HPV, which are ranked from low to high risk. The high-risk genomes such as HPV-16 and HPV-18 are associated with many cancers, such as cervical, vaginal, and anal, to name a few. The low-risk HPVs are known to be benign and, in most cases, they can be cleared by the body without any grievous harm while high risk HPVs are associated with malignancy which are responsible for the cancers mentioned above. HPV-16 and 18 are responsible for the encoding of two oncogenes, i.e. E6 and E7, which are responsible for the progression to cancer [17,18]. Both high-risk HPV-16 and HPV-18 are thought to be responsible

for 93 to 100% of cervical cancer cases [19], with HPV-16 being the most dominant viral strain that affects the cervix, followed by the HPV-18 strain. Globally, cervical cancer is the fourth most common cancer among women. The goal of the WHO Cervical Cancer Elimination Initiative (CCEI) is to reduce the incidence rate of Cervical Cancer to a threshold of 4 cases per 100,000 women-years or fewer in every country of the world [20]. But from, the global estimate in 2020, where 604 127 new cases were recorded, with the death of 341 831 occurring in low-income and middle income, shows that the result in 2020 was more than the threshold set initiative (CCEI) [21]. The persistence of HPV infection leads to the so-called cervical intraepithelial neoplasia (CIN). If detected early (i.e., when the dysplastic cells are confined within the surface epithelium of the cervix), the CIN can easily be cured. If not detected at the early stage, they can penetrate the basement of the membrane to become invasive cervical cancer and spread into the nearby organs, e.g. the uterus, bladder, rectum, and pelvic lymph nodes, causing death. The mortality rate of cervical cancer in the poorest countries has been estimated as 2-fold higher than for the wealthy countries [22]. In many low- and middle-income earning countries (LMICs), no organised cervical cancer screening programs exist. LMICs bear the most significant burden of human immunodeficiency virus (HIV) infection while, persistent high- risk HPV infection is more common among HIV-infected women. Thus, the risk of cervical cancer is increased in women with HIV/AIDS. This underscores the urgent need for the development of low-cost diagnostic devices for HPV.

There are several diagnostic methods for the detection of HPV [23] which include Papanicolaou (Pap) smear (aka cervical or vaginal cytology), direct visual inspection of the cervix with acetic acid (VIA) or iodine (VILLI), polymerase chain reaction (PCR), enzyme-linked immunosorbent assay (ELISA), radioimmunoassay (RIA), immunohistochemistry (IHC), and flow cytometry (FC). These methods suffer from

several shortcomings. For example, the Pap smear which is the most frequently used diagnostic method has reduced the mortality rate of cervical cancer by up to 50%; however, it is fraught with poor sensitivity (between 50 and 60%) [24]. Pap smear is not sustainable in under-resourced LMIC settings with low socio-economic and educational level, limited skilled cyto-screener and cytopathology workforce [25]. Despite a high prevalence of cervical cancer, lack of follow-up and poor adherence to treatment are major impediments for program success. The low-cost VIA and VILLI methods require a trained workforce to deliver and are characterised by poor specificity which can result in the substantial over-treatment of patients. Also, it is very difficult to detect small ectocervical and endocervical lesions under visual inspection so, with a once-in-a-lifetime screen or wide screening intervals, pre-cancer can be missed and progress to invasive cancer. PCR, ELISA, RIA, IHC and (PCR), enzyme-linked immunosorbent assay (ELISA), radioimmunoassay (RIA), immunohistochemistry (IHC), and FC are efficient but have the disadvantages that they are invasive, expensive, time-consuming, and bulky (i.e., limited to large hospitals). Considering that the pap smear method is the most employed technique for the detection of HPV infection in the LMICs, there is a need to design and develop a diagnostic method that complements it, but with advantages of better sensitivity and selectivity (since the level of antibodies in both symptomatic and asymptomatic patients is generally very low), less invasive, and easier to use (preferably self-use) to allow for increased coverage in the communities of the LMICs. Electrochemical detection methods meet the above criteria: they are characterised by their simplicity, high sensitivity, and selectivity and, importantly, electrochemical sensors can be miniaturised (smaller devices) for hand-held, point-of-care diagnostic testing an screening devices that require little training for operation in a given community setting. Today, most electrochemical methods of detecting HPV have been focused on nucleic

acid (DNA) sensors [26–29].

To our knowledge, the use of protein biomarkers for the electrochemical detection of HPV is largely unknown. There are only two reports that attempted the utilisation of HPV protein biomarkers. First, Piro et.al. [30] reported the use of a very complex conjugated electro-co-polymer to encapsulate the antigenic HPV-16-L1 on a glassy carbon electrode and used it to detect just a single concentration of the anti-HPV-16-L1 antibody. Second, Valencia et.al. [31] reported the detection of anti-peptide antibodies of HPV-L1 by using a gold electrode modified with a peptide (SPINNTKPHEAR) derived from the HPV-L1, a technique that involved a lot of preparation steps and only tested or suited for the detection of anti-HPV in serum samples (screening).

With these challenges that have been highlighted, electrochemistry offers several advantages. Not much work has been done in this scope, which offers a huge opportunity to do a thorough study of these biomarkers with the focus on methyl nicotinate for this work. Metal organic framework derived materials have not been used on the electrochemical detection of TB, so for the first time this work reports on the use of MOF derived materials as catalyst for an indirect detection of a TB biomarker. Also, not much work has been done in electrochemistry for the detection of HPV, most research has looked on the DNA sensors. Onion like carbon and PAN as a hybrid material will be investigated for the detection of HPV. The advantages of these materials will be highlighted in Chapter two.

Aim

The crux of this study is the synthesis of Co-NPs@C derived from metal organic framework and OLC and OLC-PAN composite as platforms for the electrochemical detection of TB and cervical cancer biomarkers, respectively, experimentally and theoretically.

1.2 The aim of this study was achieved by the two objectives sectioned into two as highlighted.

1.2.1 Objectives

- To synthesize cobalt based metal organic framework (Co-MOF) using different two ligands (biphenyl dicarboxylic acid (BPDC) and trimesic acid (TMA)
- Use Co-MOF as sacrificial templates for Co-NPS@C_{TMA} and Co-NPs@C_{BPDC}
- To characterize the synthesized materials using powder X-ray diffraction (PXRD), scanning electron microscopy (SEM), Brunauer-Emmett Teller (BET), high resolution transmission electron microscopy (HRTEM), X-ray photon spectroscopy (XPS)
- To determine the electrochemical properties of the synthesized material in a redox probe (ferri-ferro solution) in PBS of pH 6
- To test the material towards the detection of MN using CV, and DPV

1.2.2 Objectives

- To synthesize onion like carbon (OLC), polyacrylonitrile (PAN), OLC-PAN hybrid

- To characterize the synthesised materials using powder X-ray diffraction (PXRD), scanning electron microscopy (SEM), Brunauer-Emmett Teller (BET), transmission electron microscopy (TEM), thermogravimetric analysis (TGA), X-ray photon spectroscopy (XPS)
- To determine the electrochemical properties using a redox probe (ferri-ferro) in PBS of pH 7.4
- To test the material towards the detection of HPV-16-L1 antigen using CV and SQW
- To screen for HPV-16-L1 antibodies using CV and SQW

1.3 Outline of the thesis

Chapter one (Introduction): This chapter summarizes the introduction, the rationale and the motivation of the study, and its objectives.

Chapter two (Literature Review):

This chapter gives a detailed background:

- On the theory of sensors, there are different types of transducers used in sensors.
- The different types of detection methods.
- Material used, and what informed the choice of material.

Chapter three (experimental methods and characterization techniques):

This chapter covers the chemical species used, the synthesis of the catalysts of interest and the schematics of how the electrodes were prepared. It also gives a summary on the parameters of the different techniques used.

Chapter four (results and discussion):

This chapter presents the results obtained from the microwave synthesis of metal organic framework, the pyrolyzed material to Co-NPs@C. The application of the material towards the detection of methyl nicotinate. It also discusses the detection limit obtained on the material used. The discussion on density functional theory was also used to determine the interaction between the material of interest and MN.

Chapter five (results and discussion):

This chapter gives detailed discussion on the results obtained for OLC and OLC-PAN. A brief mentioning of how the immunosensor was fabricated, the detection of HPV-16 L1 antigen and the screening of HPV-16 L1.

Chapter six (conclusion and recommendations):

This chapter gives a summary of findings from Chapters Four and Five, as well as recommendations.

Chapter Two

Literature review

2.1 Introduction

2.1.1 Sensors

A simpler definition of a sensor is a device that detects/responds to a stimuli and converts the response into a valuable output signal; these can be physical or chemical sensors. Chemical sensors convert reaction interactions (e.g., certain species' concentration or total composition) into an electrical output signal (see Figure 2.1). Sensors are classified according to their transducing elements, such as optical, thermal, mass, and electrochemical sensors, amongst others; the most common are electrochemical sensors [32]. Sensors consist of two main functioning parts: a receptor and a transducer [33,34]. The conversion of reaction interactions into a form of energy that can be measured by the transducer takes place at the receptor element of the sensor [35]. The receptor elements of a sensors can be grouped according to their functioning principles. In sensors, electrodes act as transducers, there are many different electrodes that have been used for different sensing purposes, these include glassy carbon electrodes (GCE), gold electrode (AuE), screen printed electrode (SPE) which come in different types, depending on the type of active material used etc [36]. Electrochemical can be further classified as voltammetry, amperometry and potentiometry. This study focuses on voltammetry because (i) simplicity (ii) high sensitivity (iii) detects multiple analytes at various oxidation/reduction potentials.

Voltammetry includes cyclic voltammetry (CV), square wave voltammetry (SWV), differential pulsed voltammetry (DPV) to mention a few. A three-electrode system is utilized: a working electrode (WE), reference (RE) and counter/auxiliary electrode (CE) and connected to an output reader such as a computer. Figure 2.2 gives a clear pictorial representation of the three-electrode system setup [37]. In voltammetric sensing, the current is taken with respect to potential. Oxidation/reduction occurs as a result of applied potential; this reaction occurs at the WE, the RE makes sure the potential measured by WE is accurate, and CE completes the whole circuit for ion transfer. Ag/AgCl is often used as the RE, while platinum (Pt) is often employed as a CE. The cyclic voltammetry is highly used because a lot of information can be determined at the working electrode/analyte interface. The shape of CV is influenced by a lot of factors such as reversibility of the reaction, the analyte reduction potential, the sweep rate etc. When the potential is applied at the electrode, the chemical species are either oxidized or reduced on the surface of the electrode, the resulting signal is used to quantify the reacting species, Figure 2.2 shows a basic electrochemical setup [37,38]. Sensors have found widespread use in fields like medicine for early detection of disease, for example high or low levels of dopamine have been associated with medical abnormalities and behaviours, and therefore, monitoring the levels of dopamine is crucial [39,40]. In the environments for environmental monitoring chemical such as phosphates, nitrogen etc on the soil, for detection of drugs of abuse etc [41,42].

The work on sensors dates decades back, when two biosensing-based discoveries were made in 1956 and 1962, where an oxygen electrode designed by Clarke and the glucose sensor were discovered, respectively [38,43]. Since then, the research on sensors has surged over the decades and has made a tremendous contribution to societies. The attractiveness of sensors is their ability to be miniaturized into small

portable devices that can be easily handled in our homes, offices etc. For example, since the discovery of glucose sensor which monitors blood glucose to assist mostly individuals living with diabetes, it has seen so much success and has saved so many people's lives. The research on glucose sensors is still an ongoing topic with the need to improve due to the ongoing technological advances constantly. Another sensor that has been endowed with a lot of success is a pregnancy tester; the sensor detects the presence of human chorionic gonadotropin (hCG) [44]. This hormone is detected in the urine or blood of a pregnant individual, these are amongst the sensors that have hit the market and have played a crucial role in the sensor field. As indicated earlier the attractiveness of sensors is their ability to be miniaturized into small portable devices, and these mentioned sensors have served that purpose [45]. A lot can be said about sensors but cannot be contained only in this work. Electrochemical sensors have some key merits that make them very popular and very useful. These include selectivity, limit of detection, high sensitivity etc.

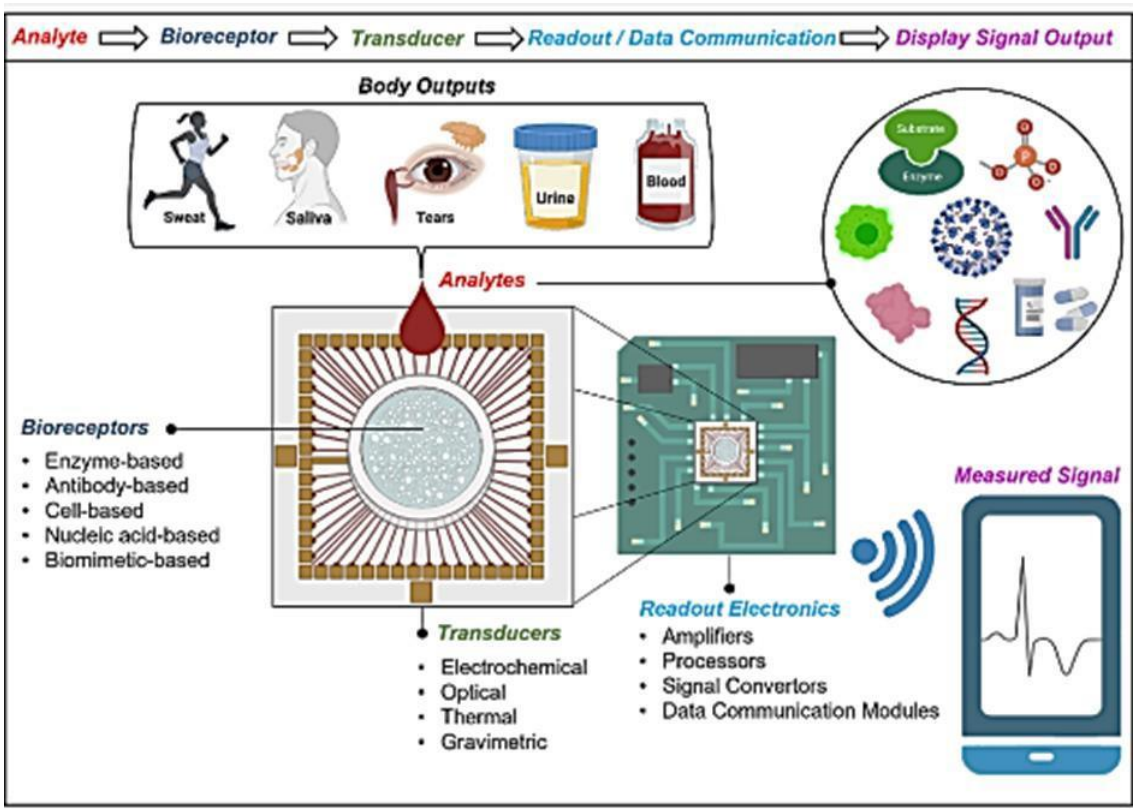


Figure 2.1: Shows the components of a sensor and the analytes that could be used [46]

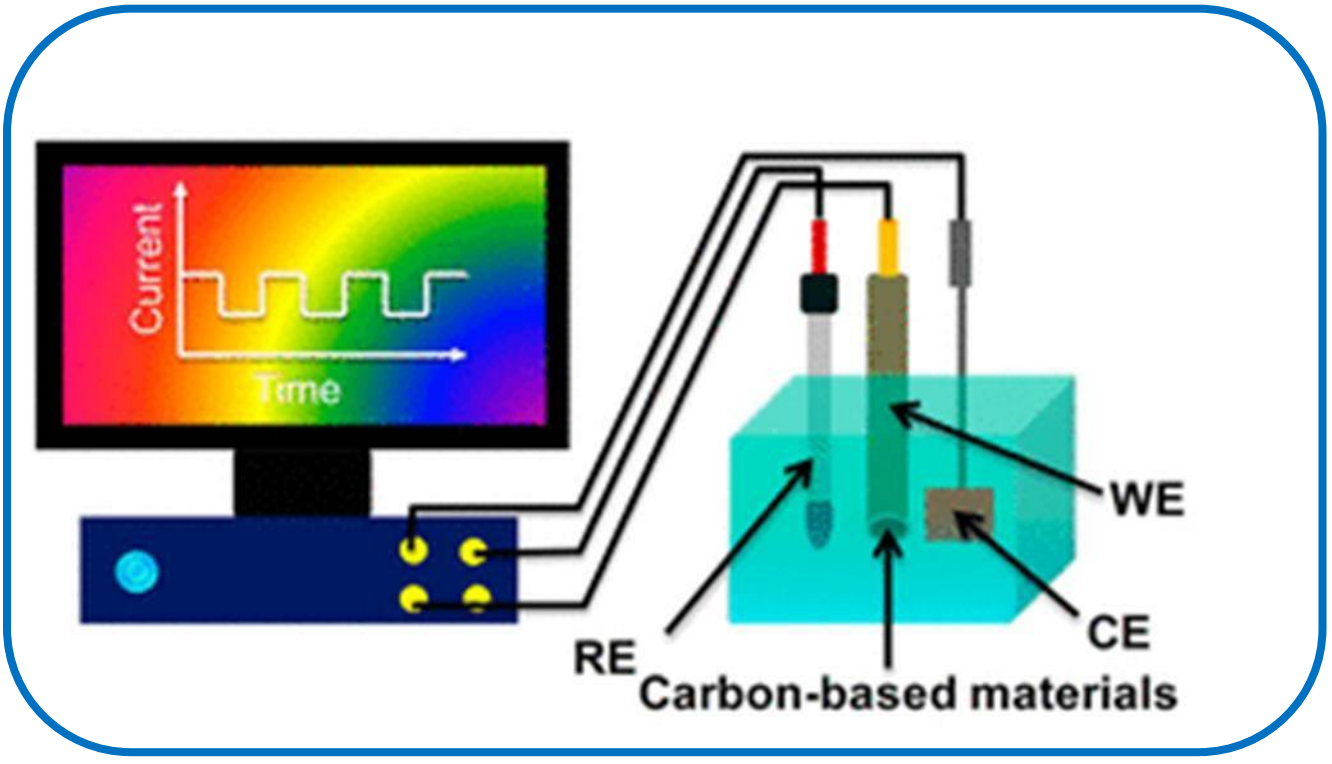


Figure 2.2: Shows three electrode setup [37]

2.1.2 Sensitivity

The sensitivity of a sensor is highly important; it is the slope of the linear part of a calibration curve of the current vs concentration plot. The information on the sensitivity of a sensor gives us how a sensor quickly responds to a stimulus.

2.1.3 Limit of detection (LOD) and limit of quantification (LOQ)

LOD refers to the minimum/smallest concentration a sensor can detect with accuracy and precision, while LoQ is the smallest concentration that can be detected with accuracy and quantification; the equations are shown below in equation below. (2.1) and equation (2.2) where s, m and LoQ are the standard deviation of the plot, the slope of the fitted plot of current against the analyte concentrations for voltammetric measurements.

$$LOD = \frac{3s}{m} \qquad 2.1$$

$$LOQ = \frac{10s}{m} \qquad 2.2$$

2.1.4 Selectivity

The ability of a sensor to detect a specific analyte of interest amongst interferant species is quite useful as there is no isolated environment. In most cases analyte is detected in the presence of other chemical/physical species.

2.1 Electrocatalysts

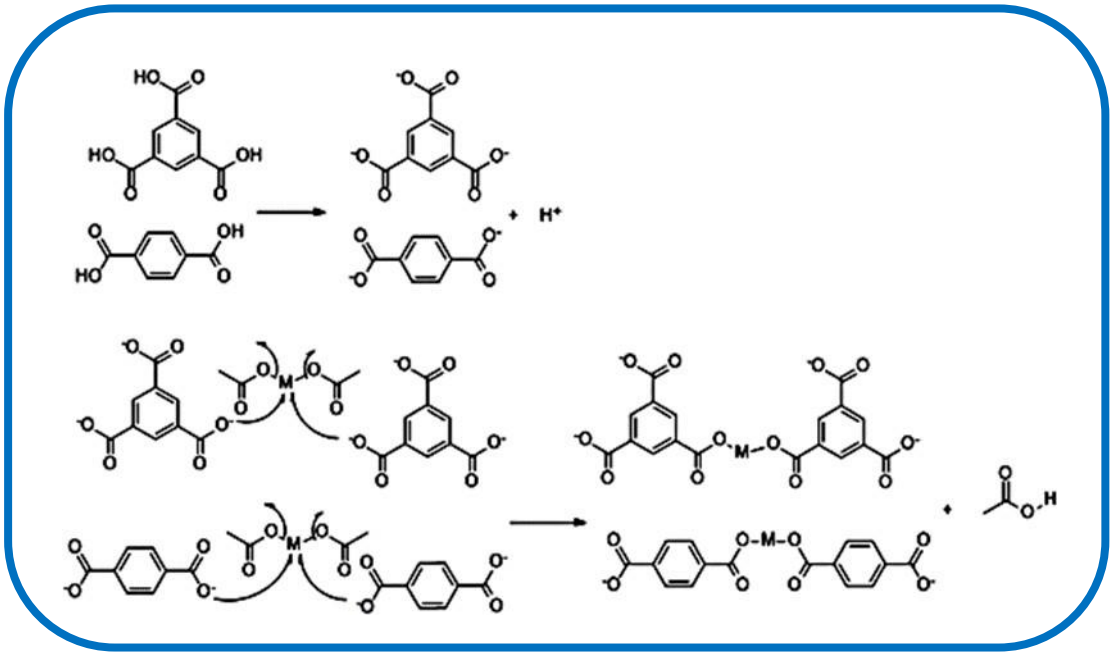
Electrocatalysts play a pivotal role in the field of sensors, a desirable catalyst should have high surface area, high conductivity, and be stable both in air and in solution.

The catalysts that are discussed in this session were chosen because they possess the above-mentioned desired properties.

2.2.1 Metal organic framework

Metal-organic frameworks (MOFs), also known as coordination polymers, are a bridge between inorganic and organic chemistry [47]. This class of molecules consists of an inorganic moiety and an organic species, they are joined together through coordination bonds. The metal acts as the connecting point while the ligand/s are used as supports. The ability to tune the properties of MOFs to suit applications of interest has aroused a lot of research interest on MOFs, which has grown over the years [48]. The use of different organic linkers with different lengths has afforded the ability to tune its pore sizes and surface area (see Figure 2.3). The ligands play a role in the properties of MOFs. The ligands act as the support centres between the metal and the ligand to form the MOF structure, which can be 1D, 2D, or 3D. Carboxylic acid, phosphonates, sulphides, and nitrogen are the commonly used ligands, carboxylic acid being the frequently used ligand [49]. Different modification on the structure of MOFS is possible, this is done to improve the properties of MOFs. Functionalizing of MOFs can be using organic linkers with functional groups or through the mixing of a linker with functionalized co-linker(s) [50]. Also, post-synthesis of MOFs can be done. Solvents also play a role in the geometry of MOFs, the metal salts and different metal to ligand, ligand to ligand to metal ratio, etc. [51–53]. The mechanism of MOF formation depends on the ligand and metal used. In the case of utilizing a carboxylic acid functionalized ligand, the mechanism involved in the synthesis of MOFs includes the generation of an anionic species from the ligand, the metal loses two electrons in the s orbital, where the ligand donates electrons to the metal to form a L-M bond, through continuous coordination of L-M a continuous network of L-M forming 1,2 or 3-dimensional

structures [49], the summary of the mechanism of carboxylic acid functionalized ligand with metal is summarized in Scheme 2.1 [52]. Different lengths of ligands have been used for the synthesis of MOFs, although MOFs are highly praised for their high specific surface area and simple synthesis, they have poor conductivity. Highly conducting material is important in electrochemistry [54,55]. To overcome the poor conductivity while taking advantage of the properties of MOFs, they have been used as sacrificial templates to make metal or metal oxide nanoparticles supported on carbon, highly porous carbon, metal oxides etc. Figure 2.4 gives a summary of how MOFs can be utilized for different application and the different types of materials that can be derived from it. As mentioned how MOFs can be utilized as templates for different types of materials with improved conductivity, a rise in the number of studies has been notable. Another attractive feature about MOFs is its ability to be used with other highly conducting materials to improve its conductivity and be applicable in electrochemistry. A growing trend on the use of MOF derived catalysts has also been growing in the field of energy conversion and energy storage [56,57].



Scheme 2.1: Reaction mechanism for the reaction involved in the formation of MOF [52]

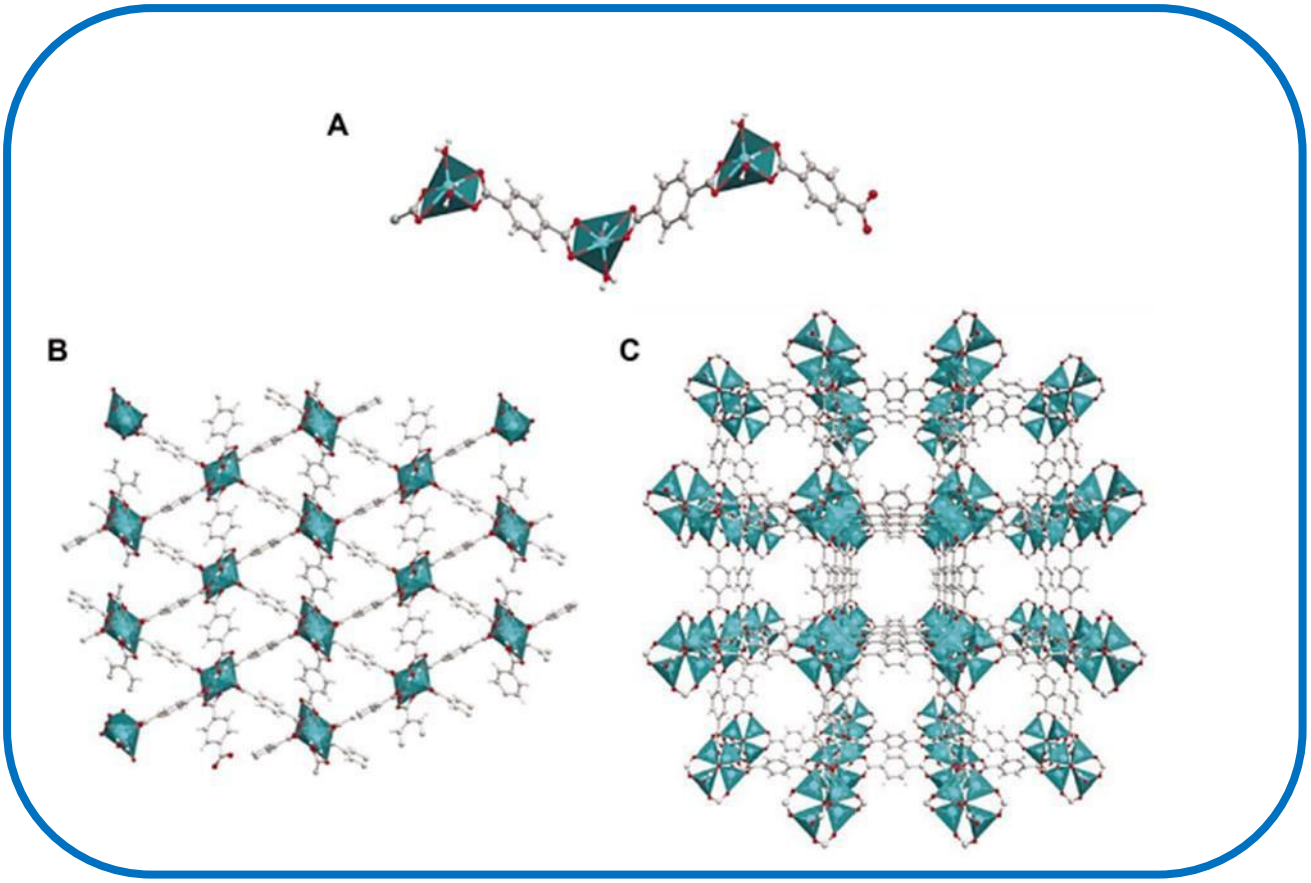


Figure 2.3: Shows the connection between the metal node and ligand [49]

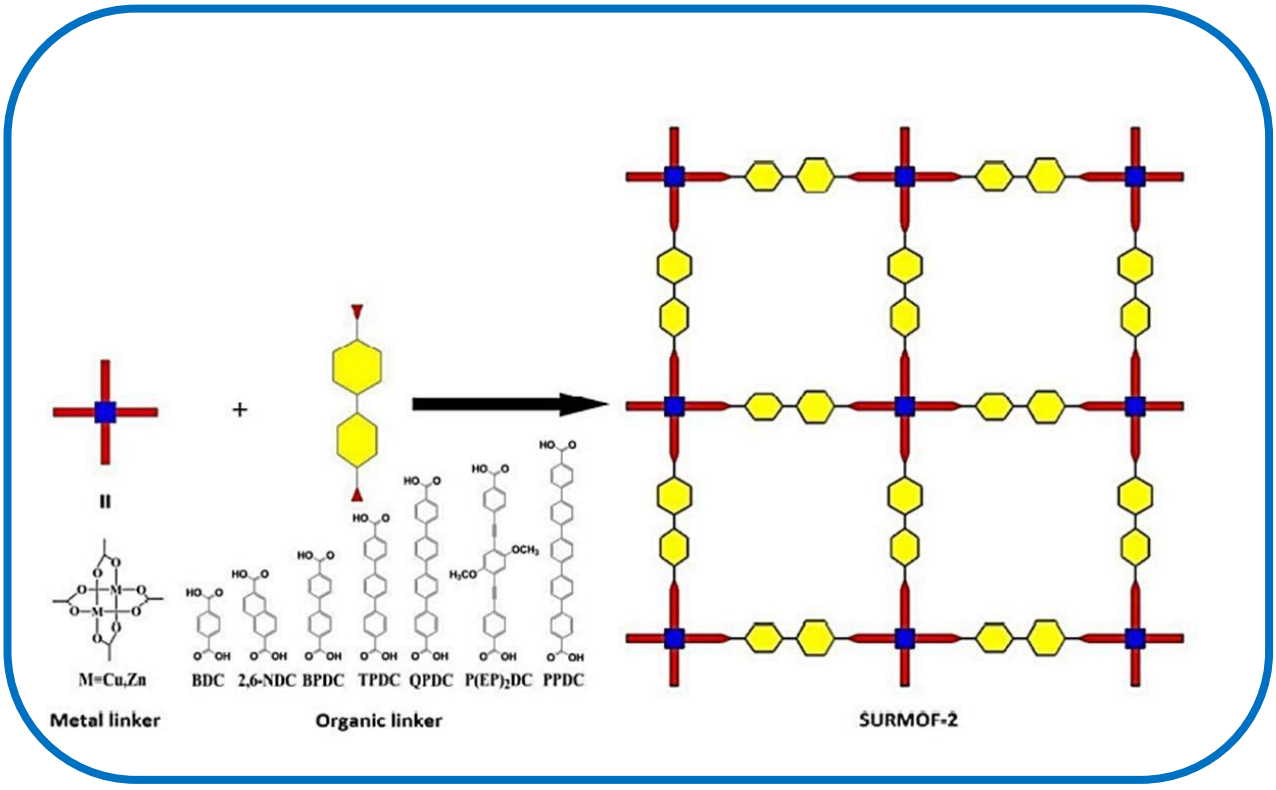


Figure 2.4: Shows the different ligands that can be used for MOF synthesis [58]

2.2.2 Synthesis methods of MOFs

While there are many ways to achieve novel MOFs, such as the use of ligands, the length and the functionalities of the ligands, the use of different metal centres, the synthetic route plays a vital role. There are various ways in which MOFs can be synthesized, namely hydrothermal route, microwave-assisted synthesis, electrochemical [59,60], mechanochemical synthesis, diffusion method and solvent evaporation and ionothermal synthesis. Each synthetic method has its own advantages and disadvantages. In this work, microwave assisted method was used for the synthesis MOFs.

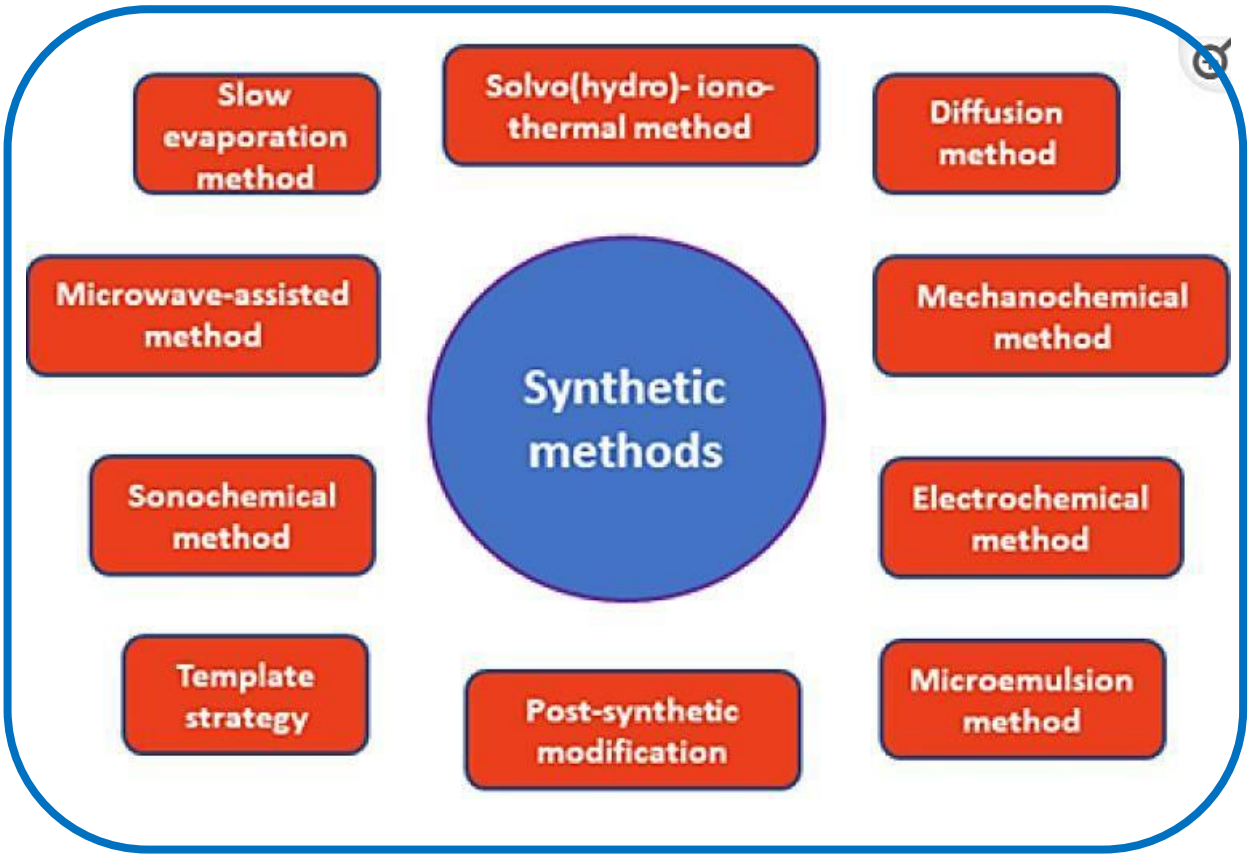


Figure 2.5: Different synthetic routes of MOFs [61]

2.2.3 Microwave-assisted synthesis (MAS)

Unlike the conventional hydrothermal synthesis of MOFs, which is an analogue to microwave-assisted synthesis (MAS), MAS offers advantages such as shorter reaction time, control of phase and morphology and distribution of particle size etc. MAS “uses dielectric volumetric heating as an alternative heat source, resulting in faster and more selective reactions due to even distribution of heat. Microwave dielectric heating drives chemical reactions by taking advantage of the medium's ability to convert electromagnetic radiation into heat. This occurs when dipoles or ions present in the reaction composition align in an applied electric field because of microwave irradiation (MW). As the electric field oscillates, the dipoles or ionic fields attempt to realign with the oscillating electric field, losing energy in the form of heat due to molecular friction and dielectric losses. A MW radiation can pass unhindered through the walls of the reaction vessel, which couples directly with molecules and ions of the reaction mixture. This reduces the likelihood of the reaction mixture to boil. In fact, heating the solvent above its boiling point is known to occur under MW conditions. Because dielectric heating is generated only within an absorbing material that converts MW energy to heat, reaction vessels must be transparent to the electromagnetic waves [62]. Unlike the traditional heating method where heat comes from the outside source, resulting in uneven heat distribution, because of this uneven heat distribution the yields, the morphology may be highly affected, (Figure 2.7) [63]

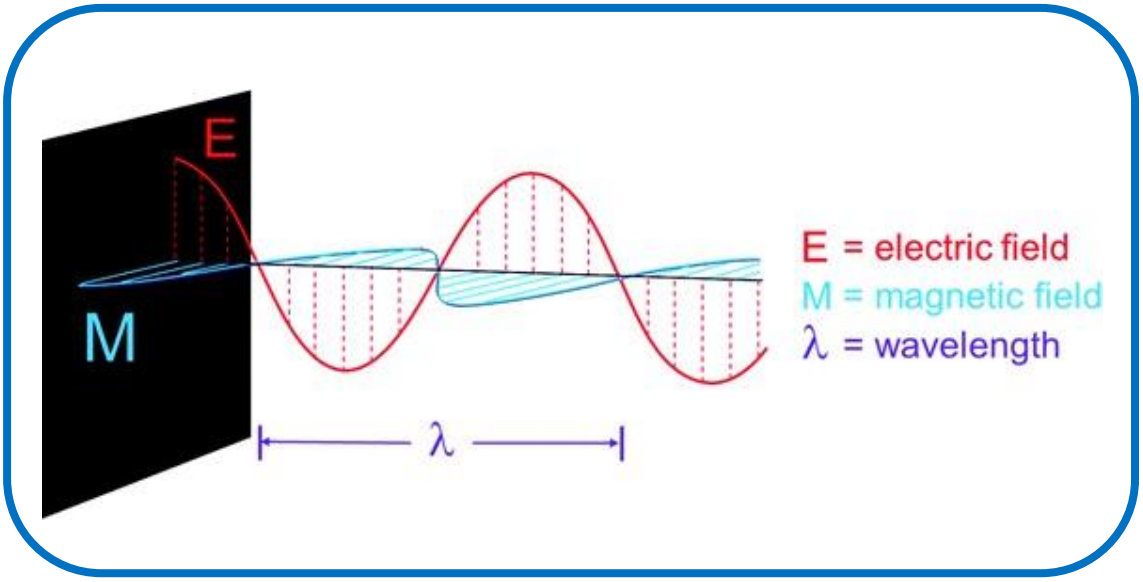


Figure 2.6: Electromagnetic waves generated during microwaving [62]

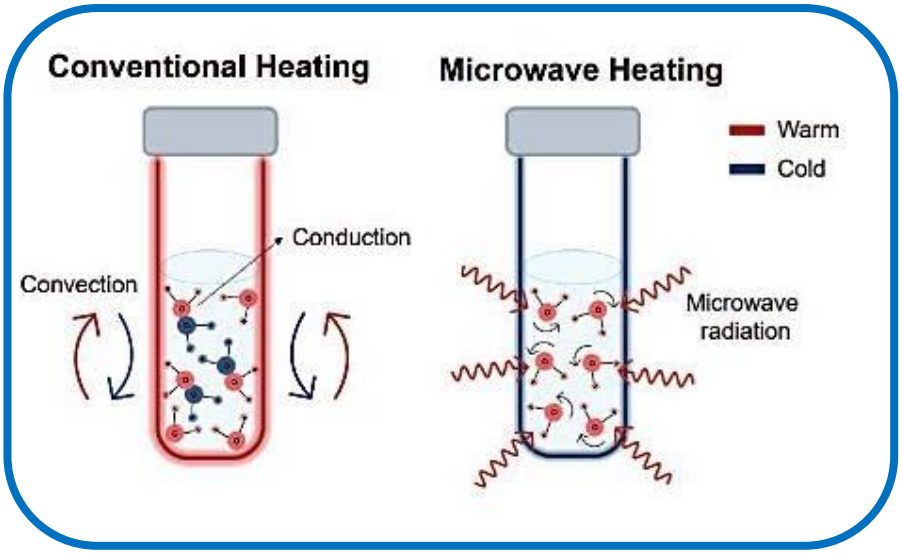


Figure 2.7: Conventional heating vs microwave heating [63]

2.2.4 Metal-organic framework as sacrificial templates

With the highly attractive properties of MOFs, their use as sacrificial templates has been an area to explore [48]. The conversion of MOFs to metal oxide or metal nanoparticles on carbon has been through a pyrolysis or carbonization method by which the MOF is heated at a certain temperature for a set period, with or without the flow of a gas [64]. The advantages of using MOFs as templates for nanomaterial is their ability to have properties inherited from parent MOF/s, see Figure 2.8 for material

derived from MOFs. MOFs have also been used to make spinel oxide. In this work MOFs were used as sacrificial template to make cobalt nanoparticle supported on carbon material (Co-NPs@C).

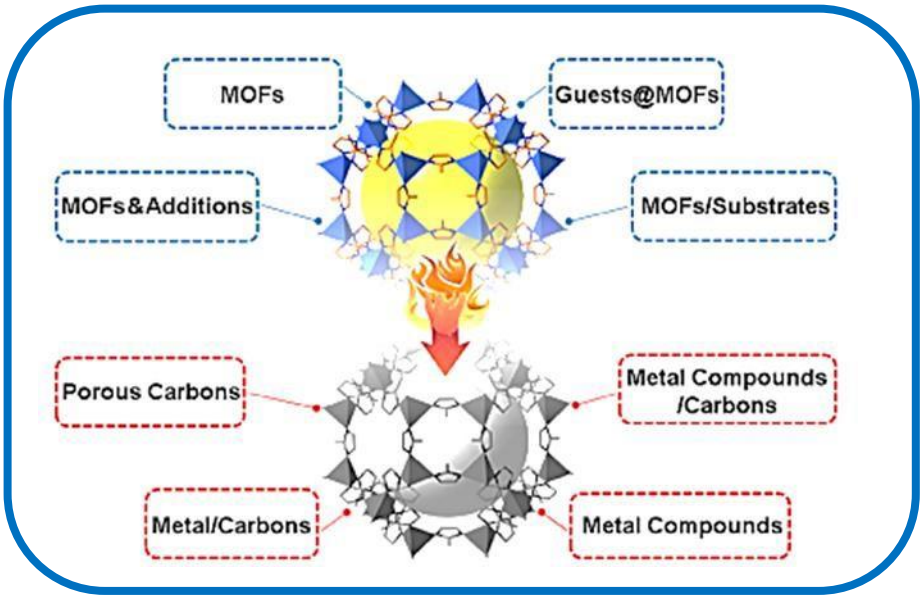


Figure 2.8: Different materials that can be derived from MOFs [65]

The use of nanosized based material for different types of applications has been growing over the years. Nano size-based material have unique properties that are different from their bulk counterparts, these properties are due to their nanosized nature. Transition metals (TM) are generally known for their multiple oxidation states [66]. Metals in the first row of TM have a partially filled d-orbital, making them good electron acceptors or donors. The choice of using cobalt is due to its abundance in the earth's crust [67] and because cobalt was reported to be good in detecting the MN. Cobalt is not only essential in chemistry but also plays an essential role in the biochemistry of human beings. Cobalt is found in our dietary food such as green vegetables; it also plays an essential role in vitamin B12 and is found in some enzymes as cofactors [68]. These highlight some of the important uses of cobalt. Cobalt in the nanosized form has shown some interesting properties such as ferromagnetic

behaviour, good catalytic activity for application in HER or OER, in sensor etc [69–71]. These compounds have been applied in vast fields, such as lithium batteries, supercapacitors, oxygen evolution reactions and gas storage [60,72,73]. The porous nature and its high surface area are what make this material attractive for electrochemical sensing purposes amongst other applications [74]. Due to the cumbersome structure of MOFs, they mostly possess poor conductivity. Hence, the use of MOFs as sacrificial templates for the synthesis of metal or metal oxide nanoparticles that are supported on carbon is becoming a trend, not only that but material derived from MOFs possess some properties that are inherited from the parent MOFs. MOF derived metal or metal oxide supported on carbon are obtained through the pyrolysis of MOFs in gaseous or in air environment. The metal centre in MOFs during pyrolysis is converted to metal or metal oxides depending on the environment they are conducted under, the ligand is converted to graphitic carbon [75,76]. The metal or metal oxide are dispersed on the graphitic layer of carbon or are encapsuled within he carbon matrix, making a core-shell structure, see Figure 2.9[77]. These materials have been applied in many fields such as pollutants adsorption, batteries, hydrogen evolution reactions (HER) and oxygen evolution reactions (OER) [78,79].

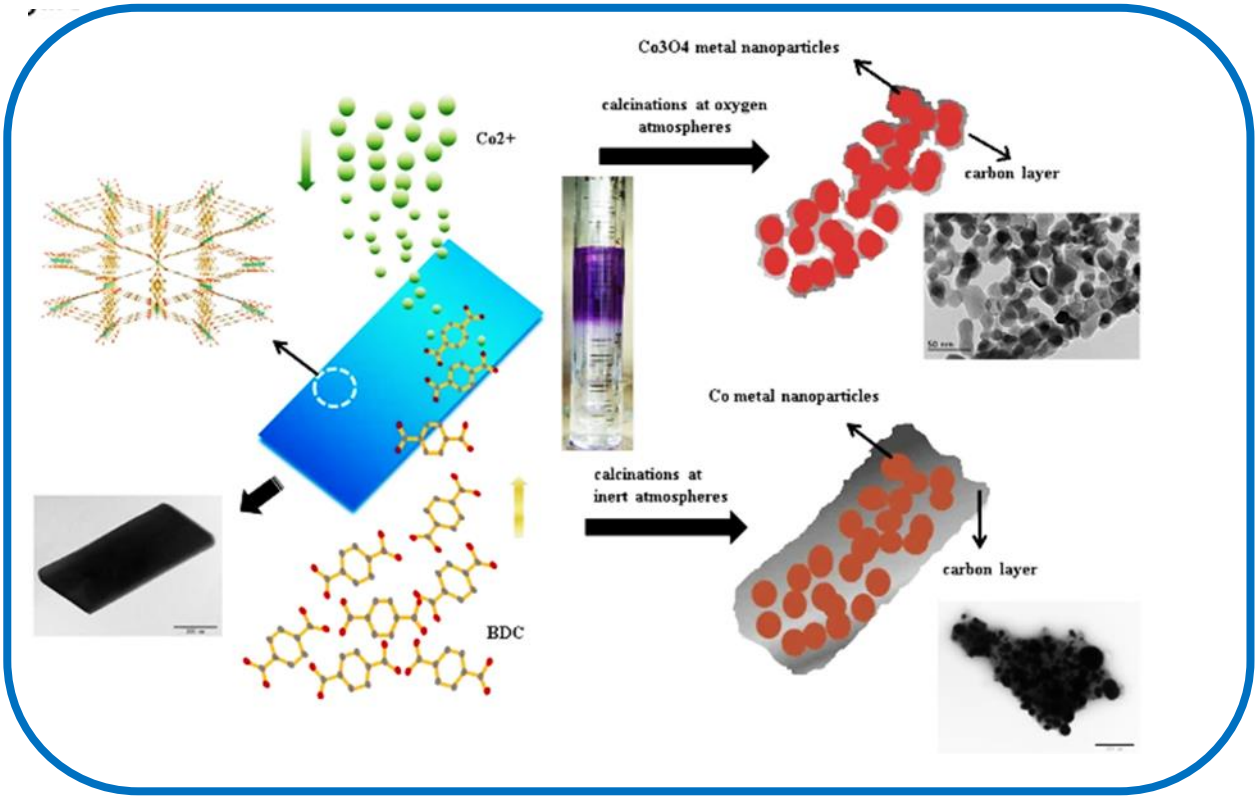


Figure 2.9: Metal organic framework derived cobalt oxide on carbon (Co_3O_4@C) and metal nanoparticles on carbon [80].

2.2.5 Onion like carbon

Onion-like carbon as the name suggests are characterized by their many layers that resemble an onion. OLCs are nanosized materials with sizes ranging from 10 nm up to 100 nm. They are fullerene_ like material that roll up in a “Russian doll” like manner [81]. They were discovered in 1980 by Sumio Iijima as by-products of carbon black synthesis and were later studied thoroughly by Daniel Ugarte in 1992 [82]. Their structure is dominated by sp^2 hybridized carbons, which makes them to have defective nature. They have been studied in different fields for their intrinsic properties such as high specific surface area, high thermal and chemical stability, high conductivity. They have been applied in fields like energy storage [83], sensor/biosensors [84,85], biomedical applications[86,87] etc. Different synthetic methods allow for introduction of different properties and functionalities, hence their vast use in different fields.

2.2.6 Synthesis of OLC

There have been many different reported synthetic routes for the synthesis of OLC, the most used is the denotation of nanodiamonds at high temperatures under gaseous or inert atmosphere. The other methods use the combustion of a carbon containing precursor/s, some use the assistance of a metallic catalyst. Other methods include mechanical milling, carbon ion implantation, underwater arc discharge between graphite electrodes, annealing of acetylene black in the presence of an iron catalyst, or heating of a carbon filament in liquid alcohol. As an alternative, onion-like carbon can also be derived via nanodiamond phase transformation, plasma spraying of nanodiamonds, laser irradiation of nanodiamonds in liquid alcohol, electron beam irradiation of carbon materials, or direct plasma treatment of coal, to name a few. Each method introduces different properties to the OLC nanoparticles; although these methods are utilized, some suffer from severe disadvantages such as low purity, some although they have nano size, and some do not possess the multilayers, which is characteristic of the OLCs and show poor yields. The denotation of nanodiamonds is frequently used method due to the advantages it possesses. The use of nanodiamonds is a multistep process, at different temperatures, transformation in the structure of the nanodiamonds takes place. Meanwhile, various nanodiamond precursors, heating rates, annealing temperatures and durations are worth investigating to find how each parameter affects the overall structure of the OLCs (see Figure 2.10) [88]. In this work the denotation of NDs was adopted because of the advantages highlighted above.

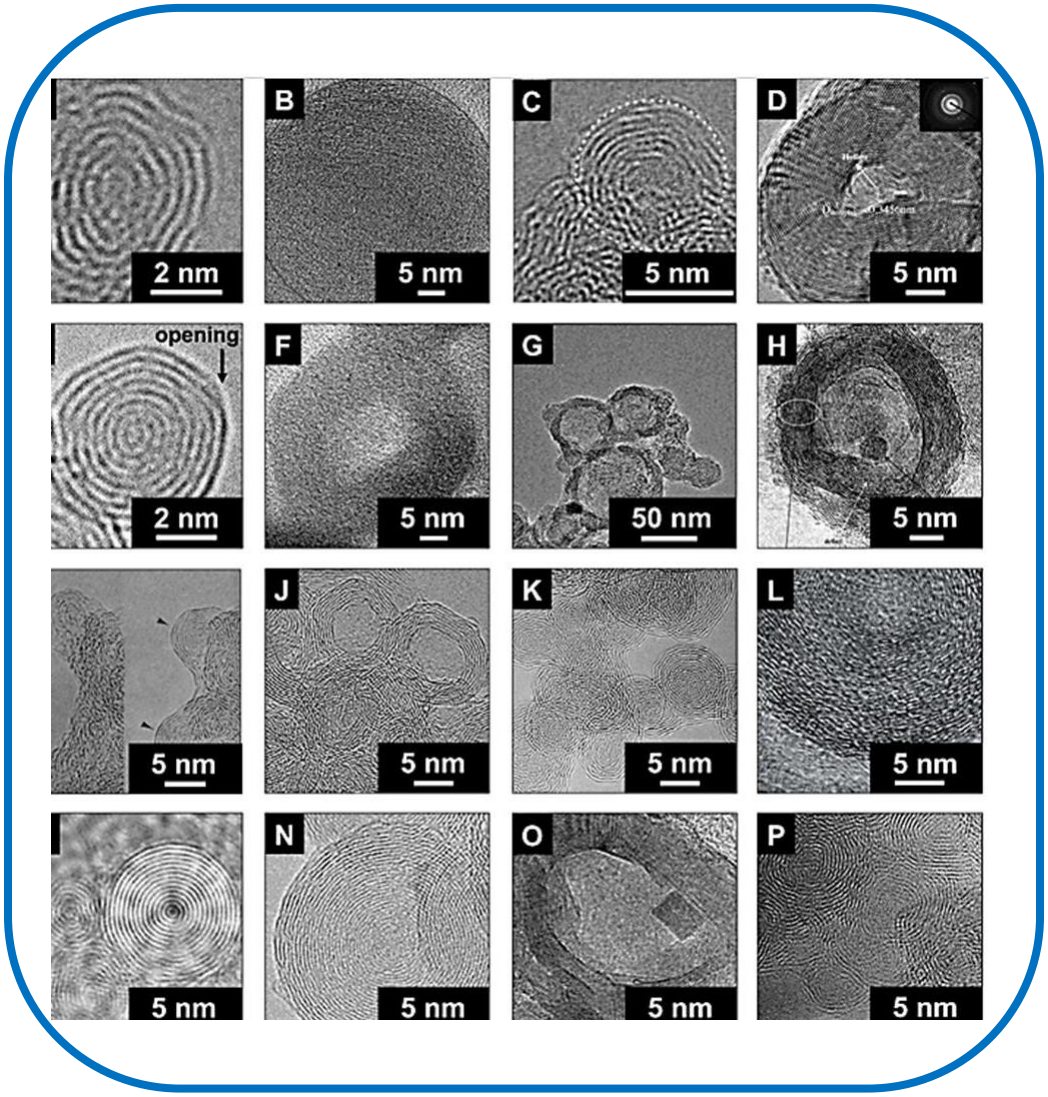


Figure 2.10: OLCs synthesized by different methods [88]

The thermal conversion of nanodiamonds into OLCs involves more than one step. Normally, it begins with the removal of moisture and the disengagement of oxygen-containing surface functional groups from sp^3-hybridised carbon upon heating to about 200 °C. As the temperature is further increased, functional groups such as carboxyl, anhydride, and lactone groups are effectively removed, leading to the generation of CO and CO_2 gases. The disengagement of the functional groups leads to the formation of dangling bonds on the carbon atoms, which merge to form π-bonds, indicating the onset of graphitization at 800-900 °C. Structural defects of the nanodiamond surface due to the synthesis or detachment of functional groups on the surface increase the reactivity of carbon atoms on the surface, which facilitates the process of phase

At temperatures between 1100 °C and 1300 °C, the initially highly disordered carbon shells of the NDs gradually become more graphitic and exhibit a lower defect density, forming a fully transformed, highly ordered OLCs at 1800-2000 °C [88]. A pictorial summary of the transformation of nanodiamond to OLCs is shown below (Figure 2.11). The changes in the ND structure are also reflected in the color changes, with the ND initially having an off-white color. As the temperature is altered, a gradual change in color is observed, resulting in a deep black color at the end of the reaction. The versatility of the OLC structure allows for functionalizing and doping. Functionalization introduces functionalities on the surface, while doping involves the introduction of mostly heteroatoms such as nitrogen (N), boron (B), sulphur (S) etc in the matrix of the structure. Functionalizing does not alter the properties of OLC, while doping has a significant impact on factors such as conductivity, thermal stability, and degree of defects (see Figure 2.12A and B).

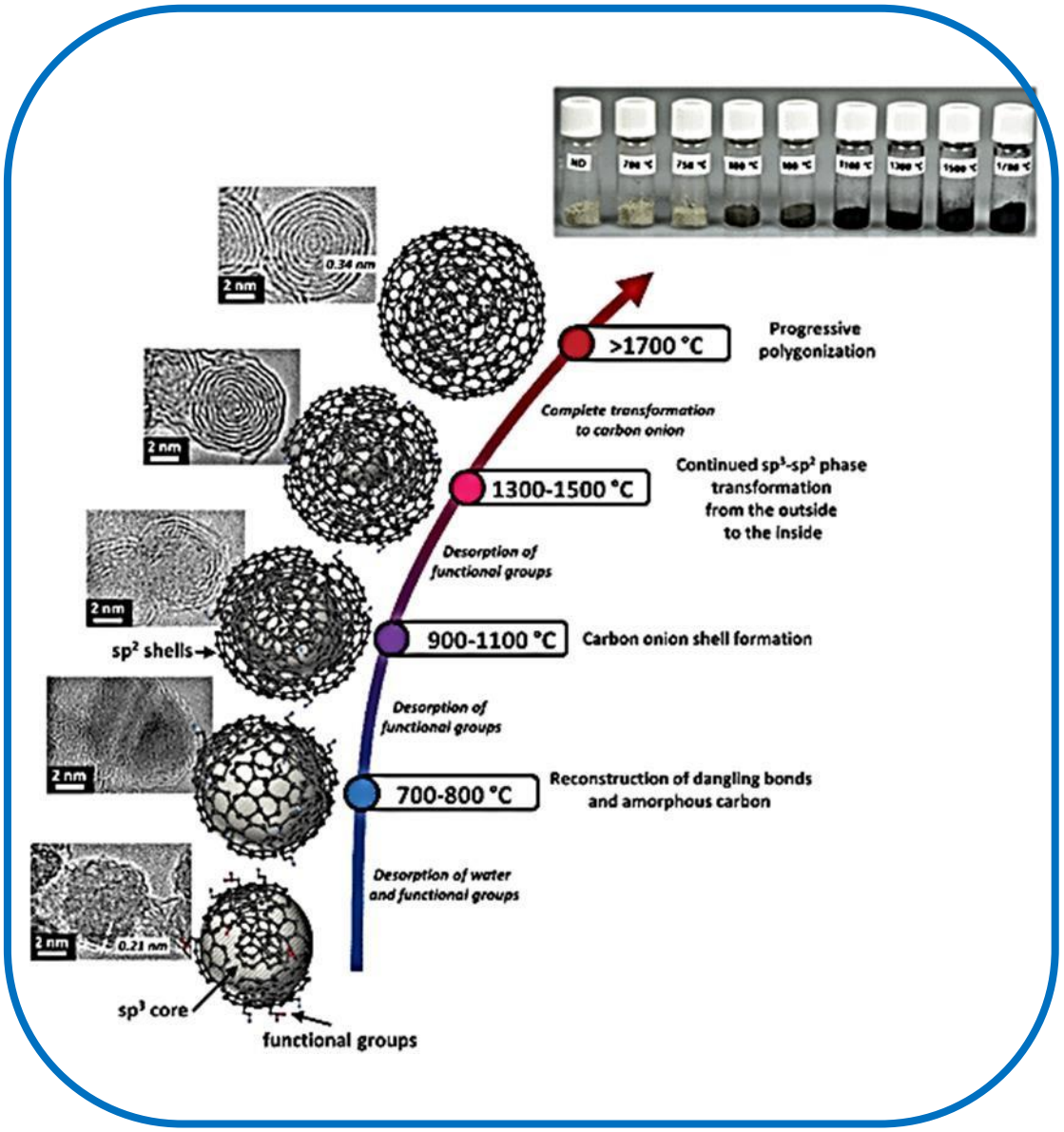


Figure 2.11: Structural transformation of ND to OLC [88]

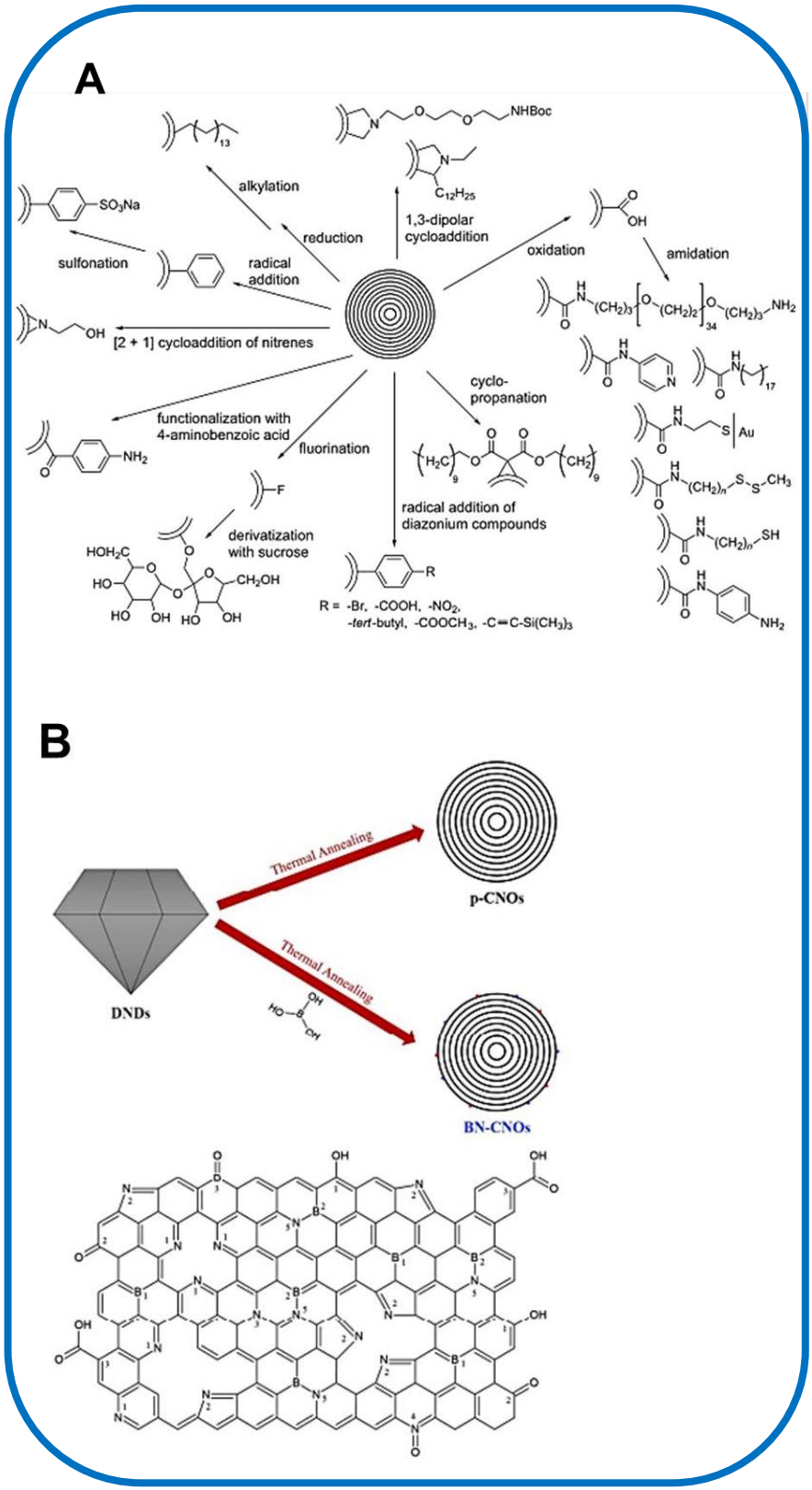


Figure 2.12: Functional groups that can be introduced on the surface of OLCs (A) and (B) doping of OLCs [89,90]

2.2.7 PAN fibers/carbon nanofibers

Carbon nanofibers (CNFs) is one of the most important materials in the carbon fiber (CFs) family, is a 1D carbon material with stacked graphene layers with a particular orientation to the fiber axis. There are clear distinct differences between CNFs and CFs, one of which is their size. The size of CNFs is in the range of 50-200 nm, while the CFs have sizes which are up to micrometres in diameter; the differences between CNFs and CFs are shown in **Figure 2.13**.

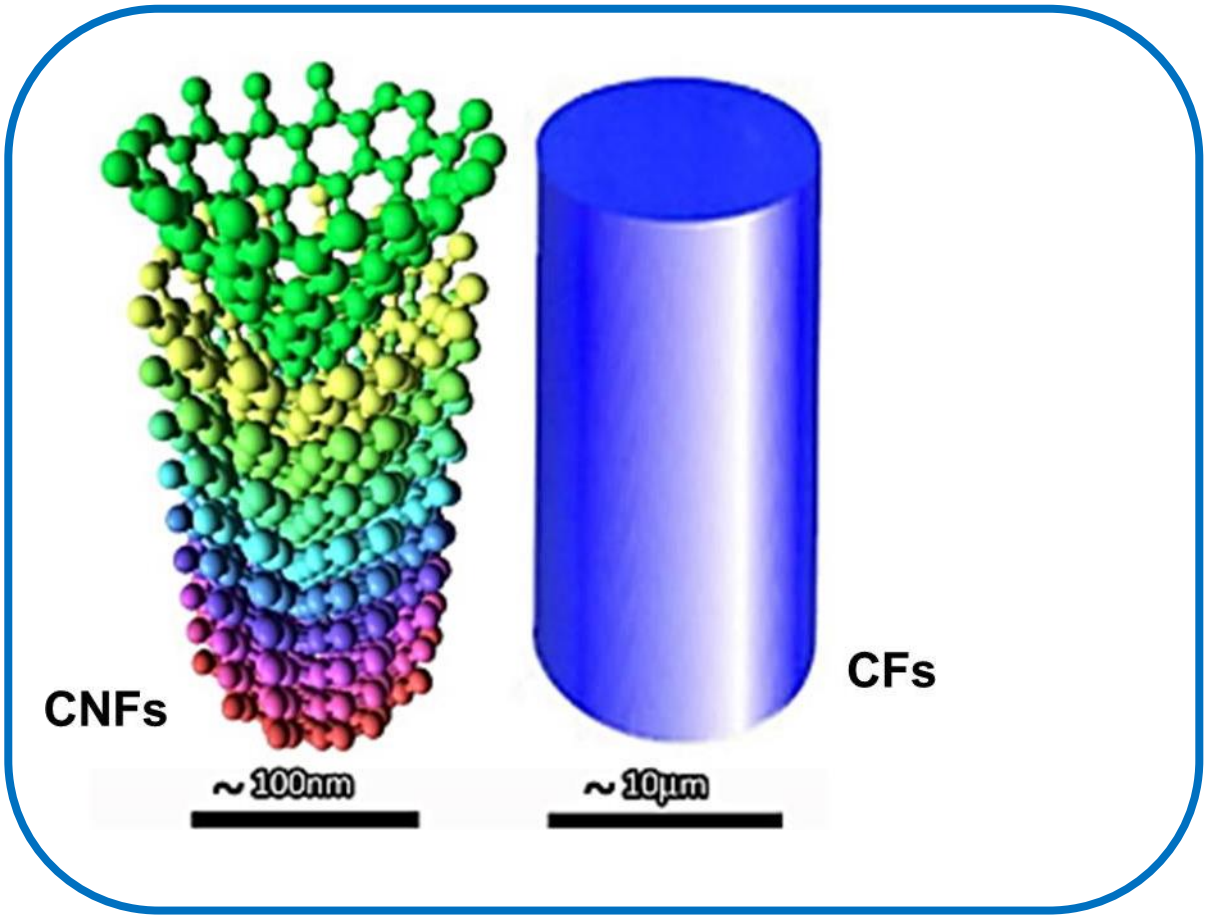


Figure 2.13: Differences between CNFs and CFs [91]

Different polymers, such as PVP, PVA, etc, have been used for the synthesis of CNFs. Polyacrylonitrile (PAN) is one of the best raw materials to produce high-performance PAN-fibers [92]. PAN-based fibers have been used in industries like the automotive, aerospace, sports goods etc, due to their characteristics such as high modulus and

strength, low density, thermal, corrosion resistance. The type of the CNFs includes fishbone, platelet, and parallel type. The most common is the parallel type.

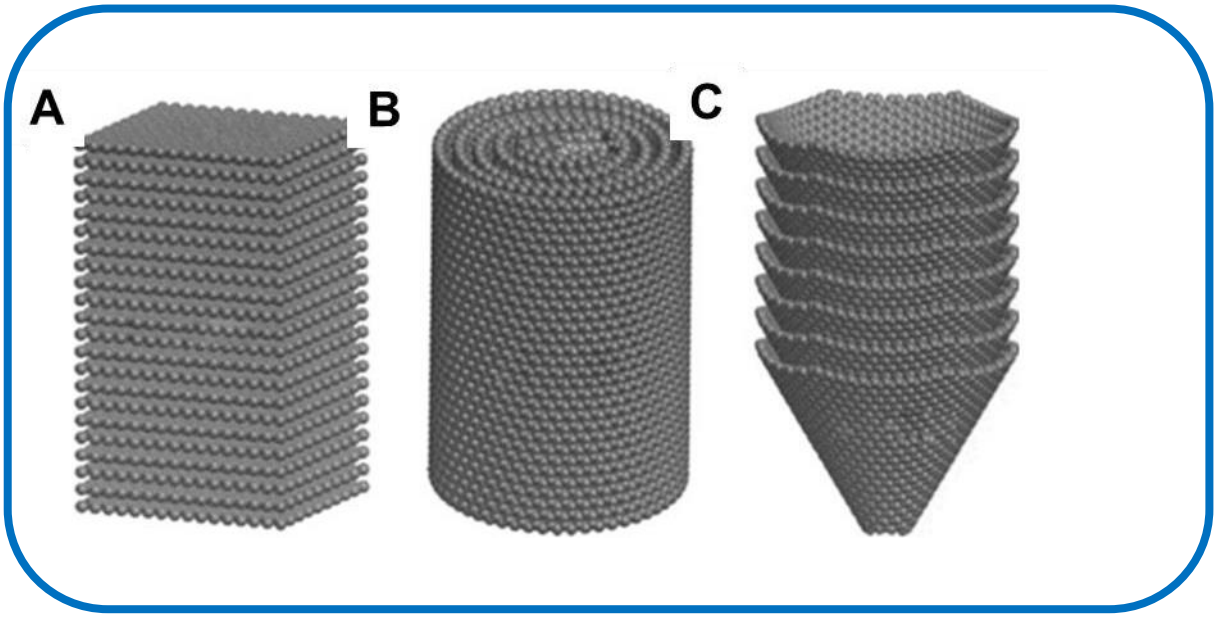


Figure 2.14: Different types of CNFs [93]

2.2.8 Synthesis of CNFs

There are different mostly utilised methods for the synthesis of CNFs, such as chemical vapour deposition (CVD) and electrospinning methods [94]. In this work CNFs/PAN-based fibers were produced through an electrospinning method. The electrospinning apparatus is a simple set-up that includes three main components: a high-voltage power supply, a reservoir for the polymer solution (e.g., a syringe with a small-diameter needle) with or without a flow control pump, and a metal screen. A high-voltage power supply with adjustable regulation that can provide up to 50 kV DC, and depending on the number of electrospinning nozzles, several independently operating outputs are required.

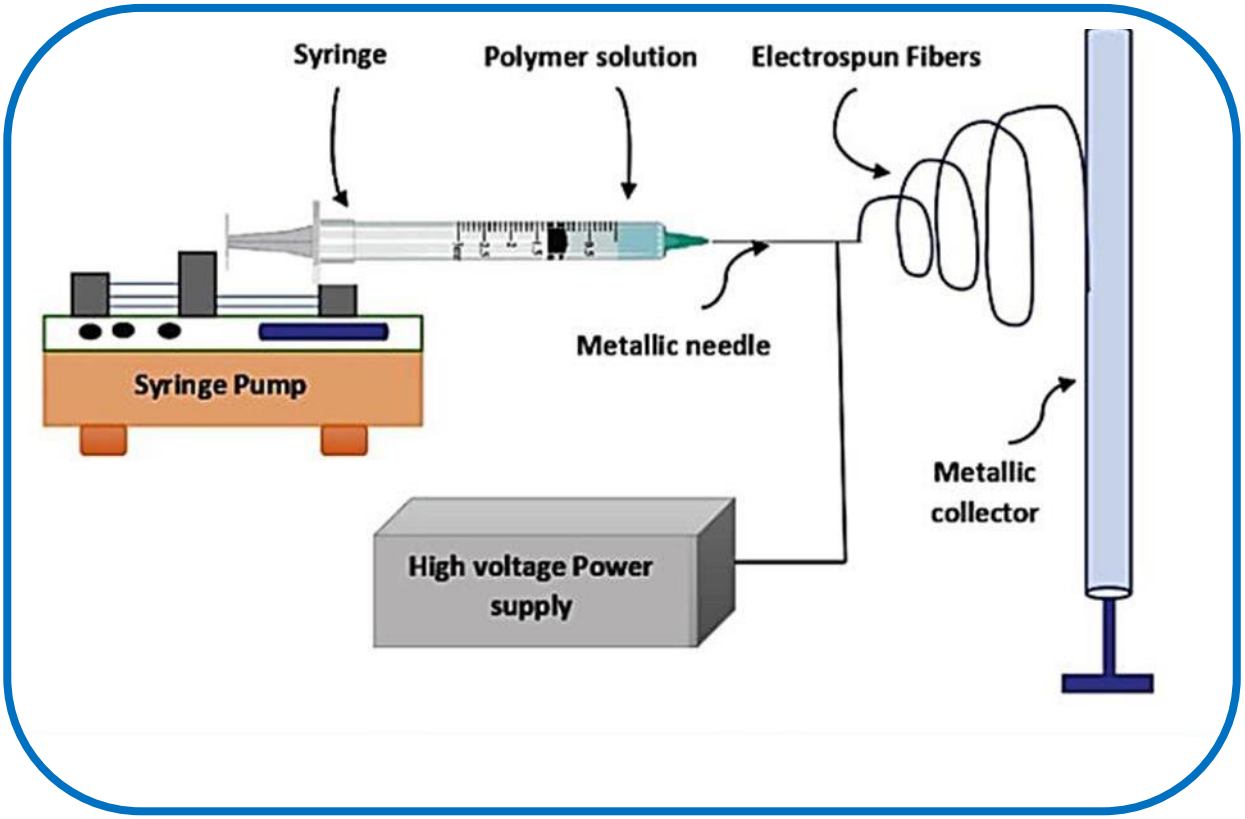


Figure 2.15: Basic electrospinning setup [95]

The polymer solution is stored in a reservoir and connected to a power supply to produce a charged polymer jet. Charging of the polymer solution can be accomplished using either a syringe with a metal needle or a capillary with a metal tip in the polymer solution. If the syringe is not placed horizontally, the polymer flow can be driven by gravity. However, to eradicate experimental variables, a syringe pump is used to control the exact flow rate. The fibre collection screen should be conductive and can be either a stationary plate or a rotating platform or substrate. The polymer fibres are insulators, and they are stabilized through the annealing process to form carbonised fibres [96], and they have been applied in energy conversion and storage as support, also in biomedicine, in sensors, to name a few. There are numerous factors that affect the final product of CNFs. The viscosity of the polymer solution and viscosity of the polymer solution have an important role in the diameter and shape of the electrospun fibre. It is controlled by polymer properties together with the molecular weight and

polymer solution concentration. When the concentration of polymer in a solution is high, the viscosity of the solution also increases. When the viscosity is too high, it is difficult to pump the solution via the syringe pump, or the solution may dry at the needle tip before electrospinning starts. Higher viscosity results in increased diameter fibres and lower deposition regions. The polymer concentration also plays the most important role in stabilizing the structure of the fibres because it influences properties such as the viscosity of the solution, surface tension, and conductivity of the material. Surface tension is the attraction between molecules in a liquid that is influenced by intermolecular interactions. During electrospinning, the charges on the polymer solution must be high enough to overcome the solution's surface tension. When a high voltage is applied, the polymer jet begins to form from the needle's tips and elongates and stretches toward the collector, breaking up into droplets due to the solution's lower surface tension. Surface tension causes bead formation when the polymer concentration is low. If the surface tension is low, the formation of the jet begins at a lower voltage. The surface tension of polymer solution can be changed by varying solvents and by adding surfactants. During electrospinning, the charged liquid (melt/solution) stretches to form fibers due to charge repulsion. In electrospinning, the choice of solvent plays an essential role since the process is affected by the solvent's evaporation rate. The volatility or vapor pressure of the solvent determines the evaporation rate and, as a result, the solidification rate of the jet. High volatility is not suitable for spinning fibers because the jet may solidify immediately after leaving the spinneret. If the volatility is too low, the fibers will still be wet when deposited onto the collector. The solvent volatility modifies the surface fiber morphology and nano-membrane structure. The permittivity of a solvent has a substantial impact on the electrospinning process and fiber morphology. The bead formation and diameter of the electrospun fiber are reduced when a solution with a greater permittivity is used.

Higher permittivity increases bending instability and the traversed jet path of the electrospinning jet, resulting in smaller fiber diameter and a larger deposition area. Solvents such as N, N-dimethylformamide (DMF) can be used to increase the permittivity of polymer solutions [95,97].

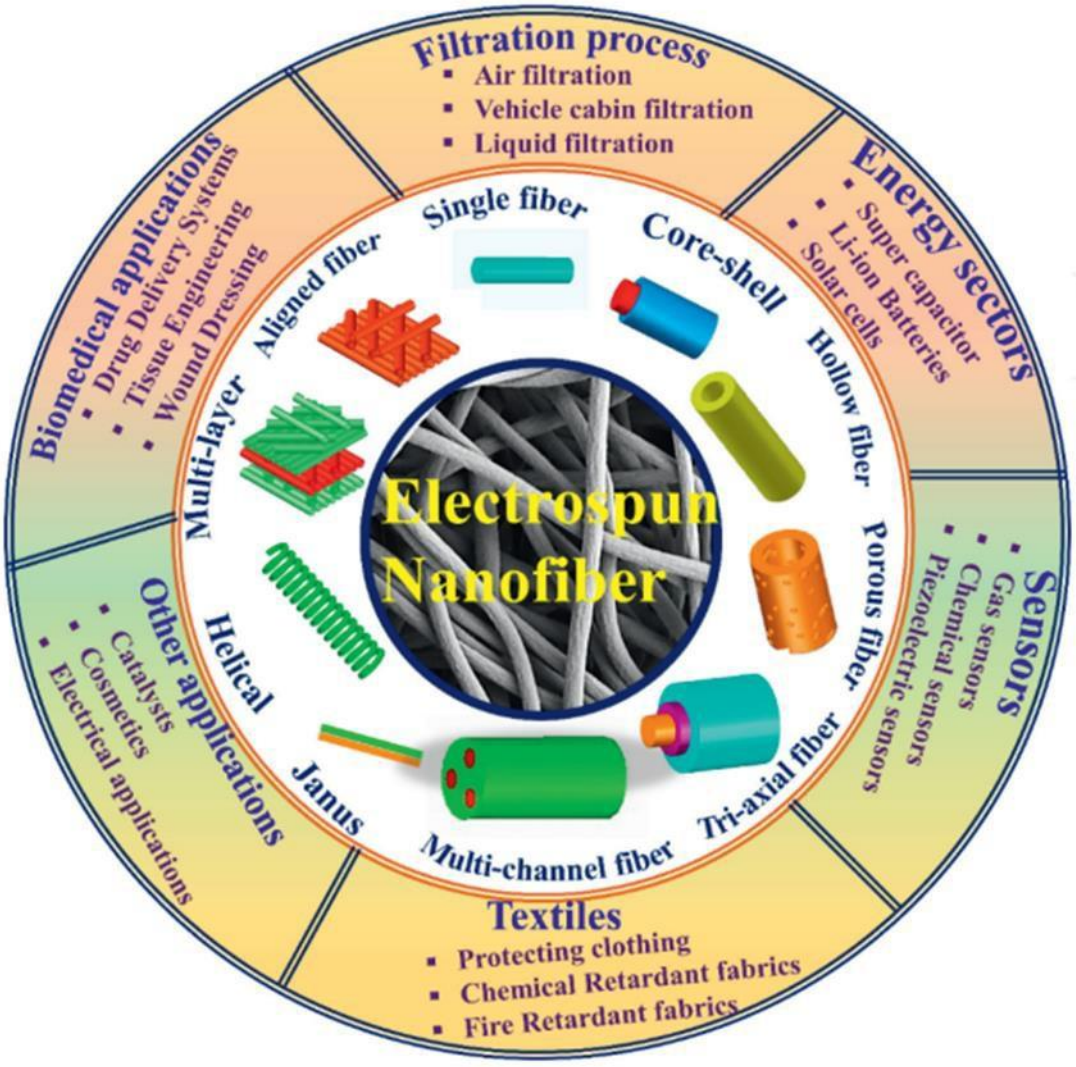


Figure 2.16: Different electrospun nanofibers with their applications [95]

Chapter Three

Experimental methods and characterization techniques

This chapter describes the experimental details, a brief discussion on the equipment parameters carried out in this work and the chemicals that were used.

3.1. Experimental

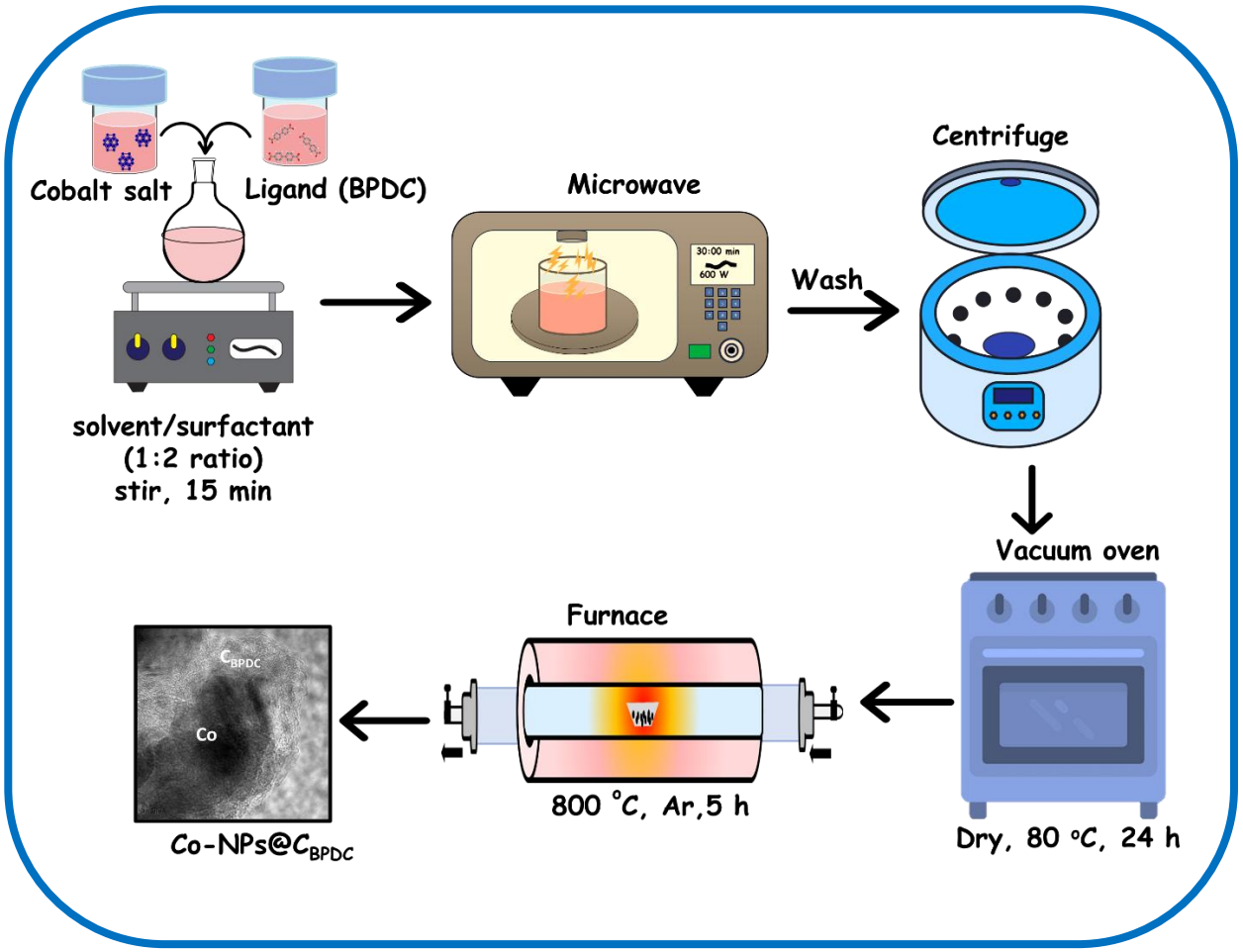
3.1.1. Materials

N,N dimethyl formamide (DMF) was purchased from Merck®. Ethanol, Nafion, and Ethylene glycol were purchased from Sigma Aldrich®. Biphenyl dicarboxylic acid (BPDC), trimesic acid (TMA), cobalt nitrate ($Co(NO_3).5H_2O$), methyl nicotinate, mono-potassium and di-potassium phosphate, ferro(IV)cyanide, ferri(III)cyanide, ascorbic acid (AA), uric acid (UA), and human serum were purchased from Sigma Aldrich®. Potassium chloride was purchased from Merck®. Glassy carbon electrode was purchased from Basi®. Platinum rod, Silver/silver chloride and screen-printed carbon electrodes were purchased from Metrohm®. PBS was prepared using 0.1 mM of potassium phosphate salts, to adjust to pH 6, HCl was used for MN detection. Mono-potassium phosphate (KH_2PO_4), sodium chloride (NaCl), disodium phosphate (Na_2HPO_4), sodium hydroxide (NaOH), ethyl-3-(3-dimethylaminopropyl) carbodiimide (EDC), N-hydroxysuccinimide (NHS), ferro(IV)cyanide (K_4[Fe(CN)6].3H2O), ferri(III)cyanide (K_3[Fe(CN)6].6H2O), were purchased from Sigma Aldrich®. Potassium chloride was purchased from Merck®. Recombinant HPV-16 L1 protein (HPV-16), anti-HPV16 L1 antibody [Cam Vir 1] (anti-HPV-16), anti-Ovalbumin antibody (anti-Ova), native Ovalbumin protein (Ova) were purchased from Celtic molecular diagnostics (PTY) see Figure 3.2. All chemicals and biomolecules were used as received. Millipore

water was obtained from Milli-Q Water Systems (Millipore Corp. Bedford, MA, USA). The saline buffer used was prepared at pH 7.4 for HPV.

3.1.2. Synthesis of metal-organic framework (Co-MOF) and cobalt nanoparticle derived carbon (Co-NPs@C_{TMA} and Co-NPs@C_{BPDC})

The synthesis of MOF and metal oxide nanoparticles derived from MOFs was done as reported in the literature (see Scheme 3.1) [98]. In brief, two conical flasks each equipped with magnetic stirrers, in a 2:1 ratio of cobalt (III) nitrate hexahydrate (0.250 g) and biphenyl dicarboxylic acid (BPDC) (0.600 g) were separately added to two conical flasks containing 20 mL of DMF and 20 mL of ethylene glycol and were left stirring until a homogeneous solutions were obtained. The two solutions were mixed and further allowed to mix for 15 min, after which they were transferred into a teflon cup and microwaved. The reaction was maintained for 30 minutes at 600W with constant stirring. After 30 minutes the solution was allowed to cool down to room temperature and the light pink product that resulted was washed several times with ethanol and then allowed to dry at 80 ^{o}C in an oven overnight (see Figure 3.1(a)). The as-synthesized product namely Co-MOF BPDC was calcined at 800 ^{o}C in a furnace for 5 h under argon flow and was later named Co-NPs@C_{BPDC}, as depicted in Scheme 3.1. Another MOF was synthesized containing a different ligand namely trimesic acid. The synthesis and calcination were under the conditions stated above. The MOF was named Co-MOF TMA with a purple colour (see Figure 3.1 (b)) and Co-NPs@C_{TMA}, respectively.



Scheme 3.1: Synthesis methodology of Co-MOF BPDC which was converted to Co-NPs@C_{BPDC}

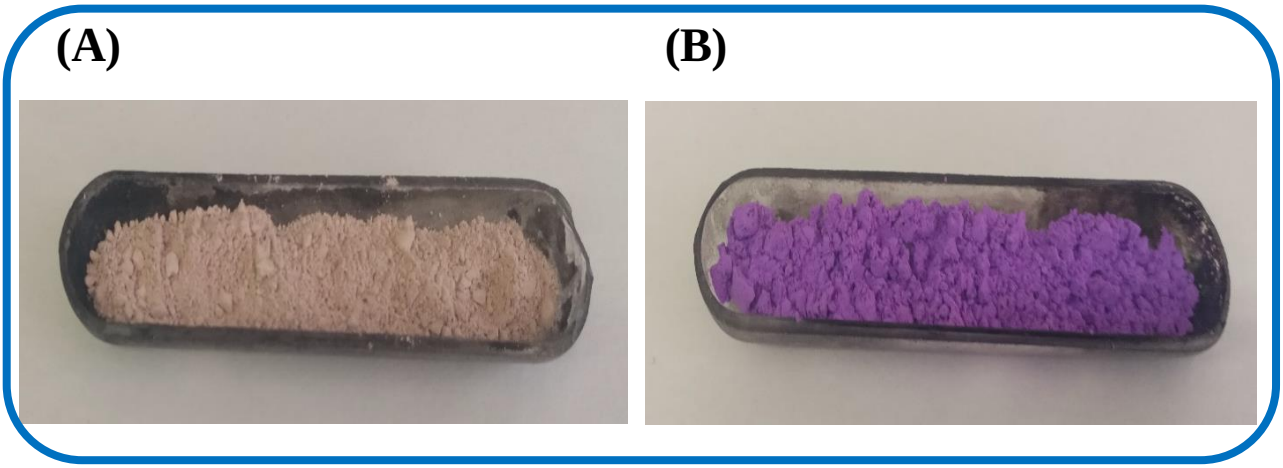


Figure 3.1: Shows (a) Cobalt metal-organic framework (Co-MOF BPDC) and (b) Co-MOF TMA

3.2. Synthesis of Onion like carbon (OLC) and onion like carbon/polyacrylonitrile composite (OLC-PAN)

3.2.1 Synthesis of OLC

OLC were synthesized from nanodiamond. Briefly, the nanodiamonds were placed in a sealed cylindrical graphite crucible and were thermally annealed in a water-cooled high temperature vacuum furnace comprising of a tungsten heaters. The heated and the cooling rate were 15 ^{o}C/min and the chamber pressure ranged between 10 and 100 mPa. To get the final OLC, further annealing at 1300 ^{o}C for 3 h under argon at 1 l/min to afford the final OLC**.**

3.2.2 Synthesis of OLC-PAN

The synthesis of OLC-PAN was according to reported literature. Briefly, in two separate conical flasks 2g of OLC and PAN were dispersed in 15 mL of DMF, the two were mixed and stirred for 2 h in ambient temperature to form a uniform solution. The solution was further sonicated for 20 min to “perfectly” uniform solution. The resulting polymer solution was fed into a syringe for electrospinning purposes. For electrospinning, the feed rate was 0.4 mL/h and the 15 cm distance from the tip to the collector; the potential difference between the collector and the grounded plate was 10 kV. The collected fibres were put in water overnight to remove DMF and were then dried at 60 °C for 2 h in an oven.

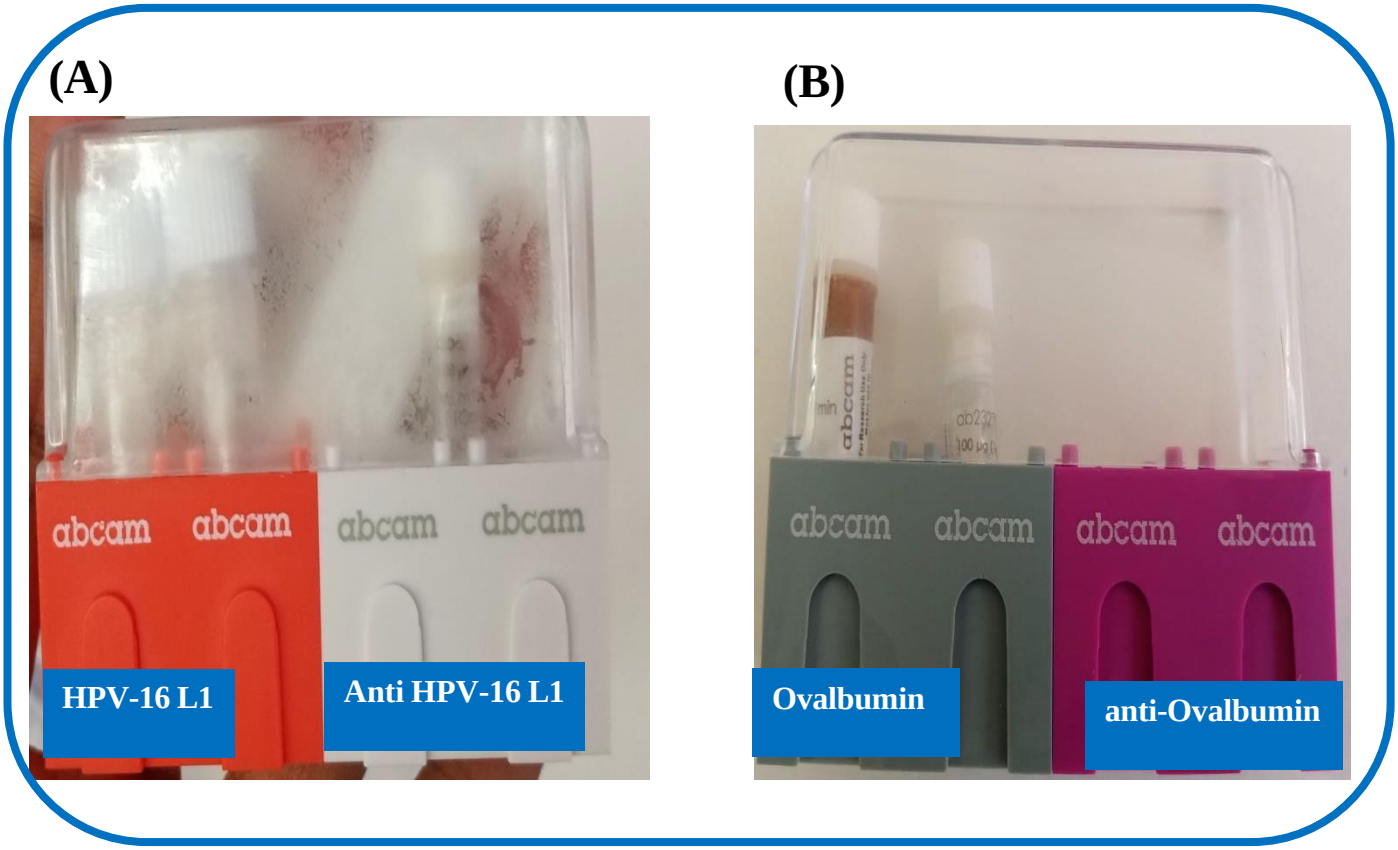


Figure 3.2: Snapshots of the biomolecules as received it their delivered package

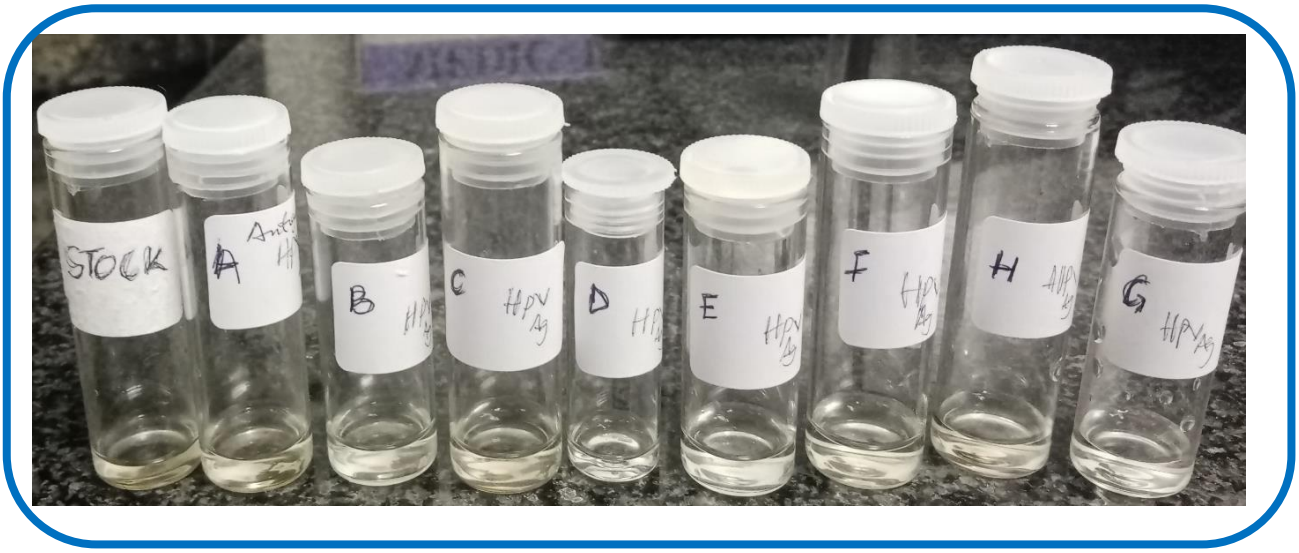


Figure 3.3: Prepared concentrations of HPV-16 L1 antigen (from the highest to lowest concentration)

3.3 Characterization techniques

3.3.1 Powder x-ray diffraction (PXRD)

XRD was used to determine the crystal structure, phase identification, sample purity etc. In many fields, such as pharmaceutical, organometallic chemistry, material chemistry, etc, it is used to characterize drugs, organometallic compounds and nanomaterials. In this work, crystal structures of the synthesized catalysts were investigated by powder X-ray diffractometer (PXRD, D2 Phaser in Bragg-Brentano configuration equipped with a sealed Co $K\alpha$ (Å) radiation tube and a secondary beam of Fe $K\beta$ filter, Bruker Lynxeye PSD detector, with primary and secondary soller slits) in the 2θ range of 5-90°. The Co source was converted to copper (Cu $K\alpha$ radiation (λ = 1.54056 Å) source.

3.3.2 X-ray photoelectron spectroscopy (XPS)

XPS was used in this work to determine the oxidation state of cobalt to determine the oxidation state of the material synthesized, and to determine the presence of N and the types of carbon for OLC-PAN. XPS measurement of all material used in this work were studied under ESCAlab 250Xi XPS with a monochromatic Al kα radiation source (1486.7eV). Survey spectra were taken at a pass energy of 100 eV and a high-resolution pass energy of 20 eV. The instrument used was in NMISA, Building 5, CSIR Campus, Pretoria, South Africa.

3.3.3 Raman spectroscopy

Raman spectroscopy was used to verify vibrational transitions Co-NPs@C_{TMA} or Co-NPs@C_{BPDC} and to determine structural defects. A 514.5 nm line of an argon-ion laser and a Horiba Jobin-Yvon LabRAM HR Raman spectrometer equipped

with an Olympus BX41 microscope attachment was used to obtain the Raman spectra. The LabSpec v5 software was used to capture the data.

3.3.4 Scanning electron microscopy (SEM) and energy dispersive X-ray spectroscopy (EDX)

The microstructures were analysed by scanning electron microscopy (SEM, FEI Nova Nanolab 600) to visualise the morphology of the material. Elemental distribution was determined by Energy-dispersive X-ray spectroscopy (EDX) on a FEI Nova Nanolab 600.

3.3.5 High resolution transmission electron microscopy (HRTEM)

The HRTEM is a microscopic technique that can be used visualize the size and shape assumed by the system under study. High resolution transmission electron micrograms (HRTEM) were acquired from an HRTEM (JEOL 2010F). The method employed for HRTEM imaging: samples were first prepared by dispersion of very little amount of sample in EtOH to obtain a very dilute solution, then coated a drop of the diluted solution on the copper-carbon (Cu/C) grid and allowed to dry at room temperature before the analysis. The dried coated Cu/C grid was then inserted into the instruments and the operating instructions were strictly followed.

3.3.6 Brunauer-Emmett-Teller (BET)

BET technique is a technique used to determine the specific surface area, porosity, and pore volume. The samples are degassed with nitrogen for several hours or days at a specified temperature, in our case the samples were degassed under nitrogen at 150 ^{o}C for 4 h. The adsorption/desorption isotherms are taken at -195 ^{o}C

boiling point of nitrogen. The BET analysis was done using the BET Micromeritics TriStar 3000 with relative pressure ranges of 0.05 to 0.30 from the absorption data for the surface area measurements. The method employed for BET data: before the BET measurement, the sample was first pre-treated at elevated temperature (80 ºC) under an inert highly pure N_2 flow to remove any contaminants.

3.4 Density functional theory (DFT)

To complement the experimental results, Density Functional Theory (DFT) as implemented in BIOVIA® Materials Studio, was used. Two BIOVIA Materials Studio modules were employed, to achieve this goal. These are Adsorption locator tools and, DMol^3 . The adsorption locator tool was used to adsorb methyl nicotinate adsorbate, onto the surfaces of Co{111} and, Co{200}. Surface supercells were modeled as follows: Co a 5×5 in {111} plane; Co, 5×5 and 1×1 in the planes {200}, respectively. The target atoms for the adsorption were the topmost ones for of the modeled surfaces. The choice of these planes was guided by the experimental XRD data obtained. The structures with and without the adsorbate were then optimized using DMol^3 and calculations for various, energies, band structures, partial density of states (PDOS), among other electronic properties. Prior to the adsorption and optimization procedures, atomic positions for Co{111} and, Co{200}, were obtained from Materials Project data base. The surface adsorption distance from the selected atoms was set as 4Å, which was the maximum acceptable (software dependent) distance for the simulation to run. Perdew-Wang generalized-gradient approximation (PW91) functionals employed for DMol^3 calculations. These functionals increases the accuracy of predicted energies and structures and minimizing additional computational time [99].

3.5 Experimental details for Electrochemical Measurements

3.5.1 Electrode modification

The electrochemical measurements were done using SP300 Bio-Logic Potentiostat operatimg on EC-Lab software. A three-electrode configuration was used (Figure 3.4) for half-cell reactions. All electrochemical experiments were performed on a bare or modified glassy carbon electrode (GCE, diameter = 3.0 mm, BASi) as the working electrode, platinum (Pt) rod as a counter electrode and the potentials were measured against Ag/AgCl electrode (saturated with 3 M KCl) used as the reference electrode. The GCE was first cleaned. The GCE was first cleaned by polishing with alumina (Al_2O_3) slurry (0.5 micrometer powder), washed with ultra-pure water, and sonicated in ethanol to remove slurry residues prior use. In the case of Co-NPs@C_{TMA} or Co-NPs@C_{BPDC}, the electrocatalysts inks were prepared by taking 5.0 mg of each electrocatalyst in 1.0 mL of EtOH and 20 µL of Nafion and then sonicated for 30 min to have uniform dispersion. The GCE was cleaned as described above. Then, the as-prepared electrocatalyst ink (5.0 µL) was drop-casted onto the well-polished GCE and allowed to dry in air at room temperature before further use. All electrochemical measurements were investigated in freshly prepared 3 mM $K_4Fe(CN)_6/K_3Fe(CN)_6$ (1:1 mixture) and 0.5 M of KCl in PBS of pH 6 and that of 7. For the detection of MN, the stock solution of 10 mM was prepared in a phosphate buffer solution of pH 6. Ultrapure water 18.2 M Ω cm resistivity) was used for the preparation of the redox probe and MN. For OLC and OLC-PAN inks were prepared by mixing 1 mg of the electrocatalysts in 1 mL of DMF, and 20 µL of Nafion solution (5 wt%) and were ultrasonicated for 1 h to form a dispersed solution. pre-cleaned GCE was then coated with 10 µL of the ink suspension and left to dry in an oven for 15 min at 30^oC. Every solution used in this work was obtained using ultrapure water (18.2 M Ω cm resistivity). Phosphate

buffer solution containing small amount of sodium azide (as a preservative) and EDTA (PBS/AE, pH 7.4) was prepared as previously described [100,101] and used to prepare the solutions of the HPV-16 L1 antigen and antibody. Redox probe solution of 0.1 mM $K_4Fe(CN)_6/K_3Fe(CN)_6$ (1:1 mixture) in PBS/AE (pH 7.4) was used for investigating the electrochemical performance of the fabricated immunosensor electrodes. The measured potentials vs Ag/AgCl in the detection of methyl nicotinate (MN) were converted to the reversible hydrogen electrode (RHE) scale according to the Nernst equation:

$E_{RHE} = E_{Ag/AgCl} + 00059\ pH + E^0_{Ag/AgCl}$ (3.1)

Where E_{RHE} is the converted potential vs RHE, $E^0_{Ag/AgCl} = 0.1976$ V at 25 ° for pH 6.

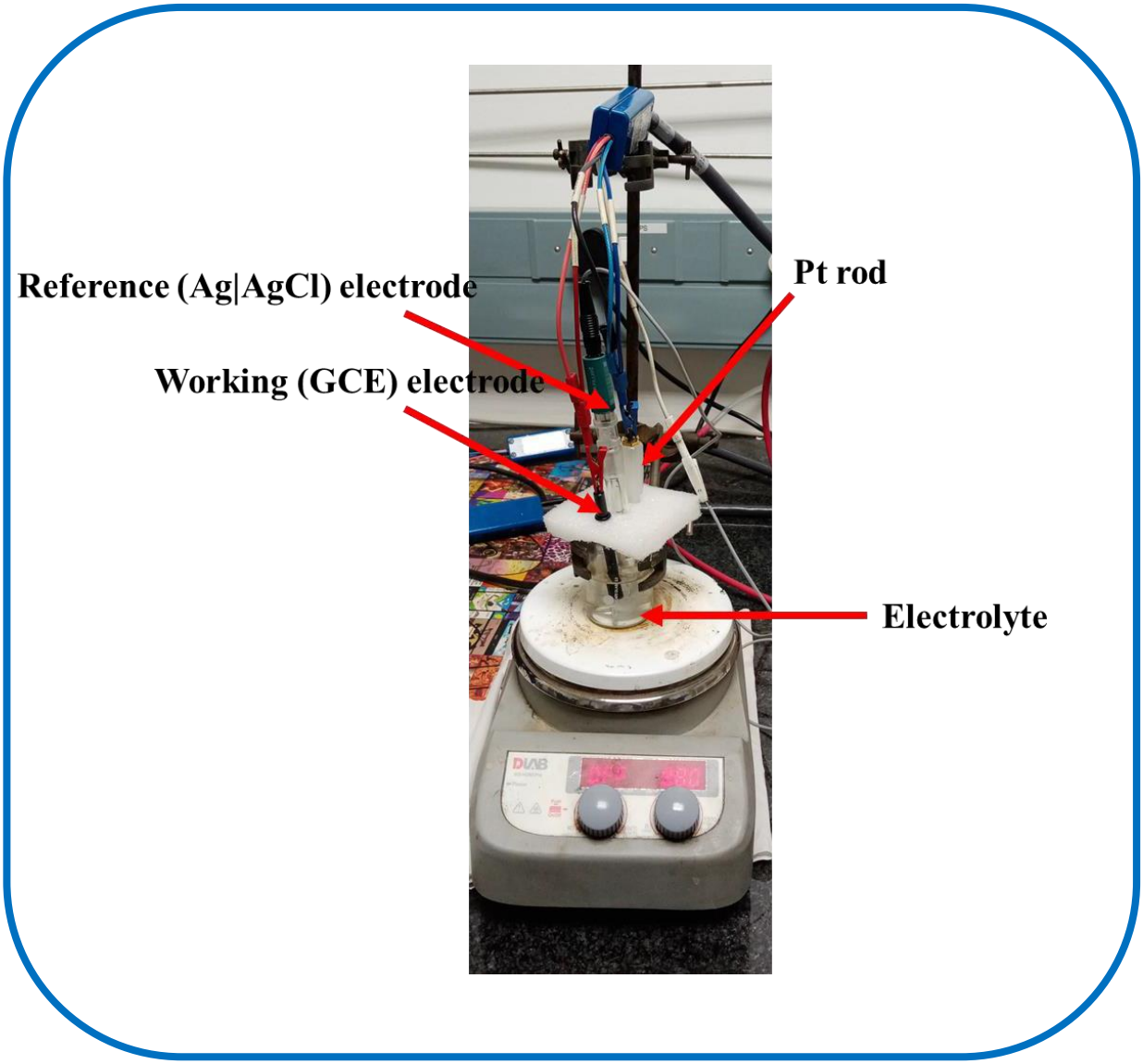


Figure 3.4: Three electrode set-up

3.5.2 Cyclic voltammetry (CV)

CV is a powerful technique used to study the oxidation and reduction of molecular species. In CV, the current is studied as a function of applied potential. The electrode potential is swept linearly across the axis to give a corresponding current response. From the information obtained from CV, one can determine the kinetics of the reaction, mass transport of the reaction, the equilibrium potential, the reversibility and

irreversibility of the reaction etc. In this work, CV was used to determine the kinetics of the electrode and the reversibility and irreversibility of the reactions of interest, amongst others. The voltage window used was between -1 V and 1 V, and the sweep rate varied when necessary.

3.5.3 Square wave voltammetry (SWV)

Square wave voltammetry (SWV) is an attractive alternative to CV where the contribution of non-faradaic current in voltammogram can be minimized. Unlike CV where the potential swept in a linear manner with specified scan rate/s, the potential is applied in a waveform with certain pulse amplitude (E_A) and width (t_p) in a form of a staircase: in the first cycle, a positive E_A pulse is followed by an oppositely directed negative E_A pulse of equal magnitude, followed by a next cycle starting at an increased potential according to a E_{step} value [102]. In this work, SWV was used for concentration studies, which were later used to determine the limits of detection and was also used for proof of concept using screen printed electrode (SPE).

3.5.4 Differential pulsed voltammetry (DPV)

DPV is a pulsed technique with minimal background noise, it measures current as a function of time and potential. Differential pulse voltammetry is a controlled potential analysis method in which a pulsed potential of constant amplitude is applied, and the potential is increased over time so that the potential of each subsequent pulse is slightly higher than the potential of the previous pulse. The return potential after each pulse is slightly negative compared to the potential before the step, and this base potential increases to the same value between pulses. The final measured current signal is the difference between the current just before the pulse is applied and the current before the end of the pulse. The applied potential was between -1 V – 0.5 V, the time of equilibration 40 s, with a pulse high of 50 mV, pulse width of 100 ms, step

height of 5 mV, and step time of 500 ms. All these were kept constant while conducting concentration studies.

Chapter Four

Electrochemical detection of methyl nicotinate

4.1. Brief introduction

Early detection of diseases remains a crucial task for the individuals suffering from the disease and the healthcare system. Early detection relieves the burden to the health care system, while it also curbs the spread and assists in the management of diseases. TB remains burdensome, although there are ways of treating it, early detection remains a challenge. With many diagnostic techniques that have been used to date, there are still a lot of shortcomings associated with them (discussed in detail in the Chapter one).

The focus of this chapter will be mainly on MOFs and MOF-based materials, their characterizations and their application in the electrochemical detection of methyl nicotinate, which is a biomarker associated with TB. The material/ catalysts of interest were synthesized through a microwave-assisted method (Anton Paar), and they were then used as sacrificial templates. The effect of using different ligands of different lengths was also studied, and how it affected the outcome of the metal-organic framework derived material (MOFDM).

4.2 Characterization

The as-synthesised MOFs (Co-MOF TMA and BPDC) were used as a sacrificial template for the synthesis of Co-NPs@C_{TMA} or Co-NPs@C_{BPDC} respectively, through pyrolysis method in a furnace. The electrocatalysts were physico-chemically characterised using X-ray diffraction (XRD), Raman spectroscopy, scanning electron microscopy (SEM), X-ray photoelectron spectroscopy (XPS), high-resolution transmission electron microscope (HRTEM), Brunauer–Emmett–Teller (BET) and electrochemical techniques.

5.7.5 XRD of Co-MOF TMA, Co-MOF BPDC, Co-NPs@C_{TMA} and, Co-NPs@C_{BPDC}

Figure 4.1 shows the XRD of (A) Co-MOF BPDC, and (B) Co-MOF TMA with (C) Co-NPs@C_{BPDC} and (D) Co-NPs@C_{TMA} with their respective crystallographic information file (CIF) of Co and CoO. The main peak for the MOFs was at 2θ value of ~10° and ~17° for both MOFs as reported in literature, these can be ascribed the crystal phases 002 and 100 of Co [52,103,104]. The other X-ray diffraction patterns of the (C) and (D) samples relates to the Co-NPs@CoO phase as shown. The peaks 26.8° corresponds to carbon 002 crystal plane. It is evident that there are intense peaks belonging to metallic Co, whereas the other weak peaks can be attributed to CoO species. The Co.cif assigned the peaks at 2θ degree positions 44.6 and 51.6 which can be ascribed to (111) and (200) crystal planes of Co, and the at 36.8, 40.2, 41.9 and 47.7, respectively, can be ascribed to miller indices (111), ((102), (200), (210) according to CoO.cif indicative of Co with fcc structure ([105,106] . Furthermore, a shift towards lower 2θ degree was observed for Co-NPs@C_{BPDC} relative to Co-NPs@C_{TMA}, this could be because of lattice distortion which may be caused by the different lengths of ligands used. There were no peaks due to Co_3O_4.

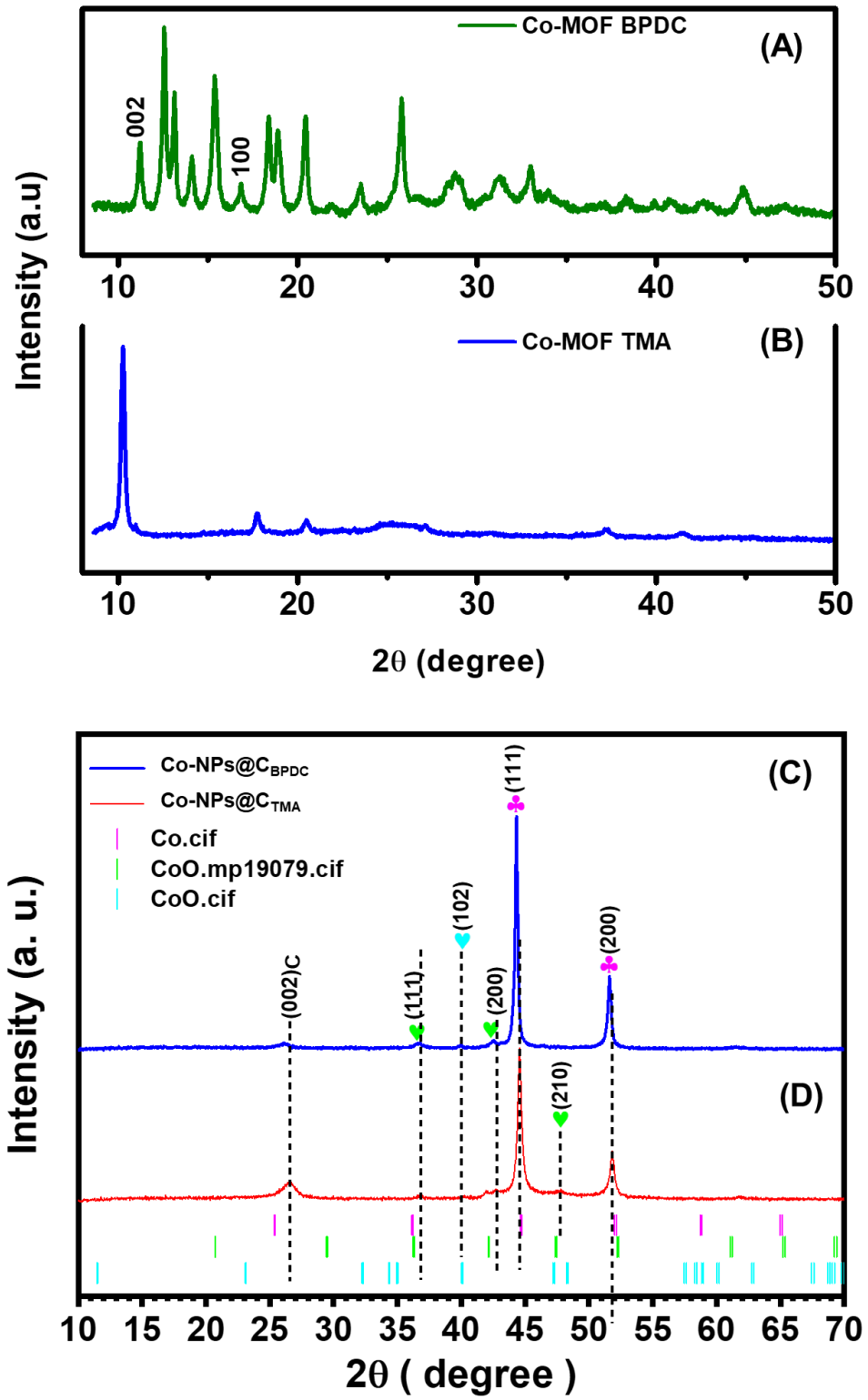


Figure 4.1: X-ray diffraction of parent MOFs (A) Co-MOF TMA and (B) Co-MOF BPDC, (C) Co-NPs@C_{BPDC} and (D) Co-NPs@C_{TMA}

4.2.1.1 Raman of Co-MOF TMA, Co-MOF BPDC, Co-NPs@C_{TMA}, and Co-NPs@C_{BPDC}

The raman spectra of Co-TMA or BPDC MOF are shown in Figure 4.1 (A) and (B), respectively, the resulting spectra showed vibration modes at 130 cm^{-1} and 404 cm^{-1} due to the longitudinal mode (LA) and Co metal node-oxygen (Co-O) respectively. The organic ligand linkages (C–O–C) vibration, (C–O–C)asym, (C– C)v aliphatic, (C–O–C)ring + CH and C–C rings were ascribed the peaks at 631, 850, 1139, 1199, 1266, and 1440 cm^{-1} ,respectively [104,107,108]. These results confirmed the formation of Co-MOFs. Figure 4.2 shows the raman spectra of (C) Co-NPs@C_{TMA} and, (D) Co-NPs@C_{BPDC}. The peaks at 195.09, 620.09 and 696.54 cm^{-1} were assigned to F_{2g} modes, while the peak at 482.57 was assigned to E_g mode, and the peak at 696.54 cm^{-1} assigned to A_{1g} of Co_3O_4, this may be due to the high intensity of the laser beam. The other characteristic peaks observed at 1349 and 1586 cm^{-1}, were assigned to the D and G bands, respectively. The D peak is due to defects, while the G peaks are due to sp^2 bonded carbons, which arise from the doubly degenerate E_{2g} peaks [109]. For quantitative analysis of the material, the D and G peaks were deconvoluted and fitted to three Gaussian function and one Loretzian function as seen in Figure 1 (C) and (D). The choice of using Gaussian functions for the D4, D3, and D2 bands was driven by their better fit with the experimental data [110,111]. The Loretzian function refers to the D1 band assigned to the carbon atoms at the edge sites of the graphene layers and the D4 band arising from the C=C and C–C bands, and the G band as a result of the graphitic lattice, while the D3 band arising from the amorphous carbon [112]. The slight red shift in the D and G raman shift of Co-NPs@C_{BPDC} and the broadening of the peaks were due to high oxygen vacancies on the material [113] or it may be due to structural defects due to the different ligands used [114]. The ID/IG ratio determines the degree of graphitization or defects, and the calculated ID/IG ratio's were 2.03 and

1.90 for Co-NPs@C_{BPDC} and Co-NPs@C_{TMA}, respectively. Co-NPs@C_{BPDC} showed more defects than Co-NPs@C_{TMA}

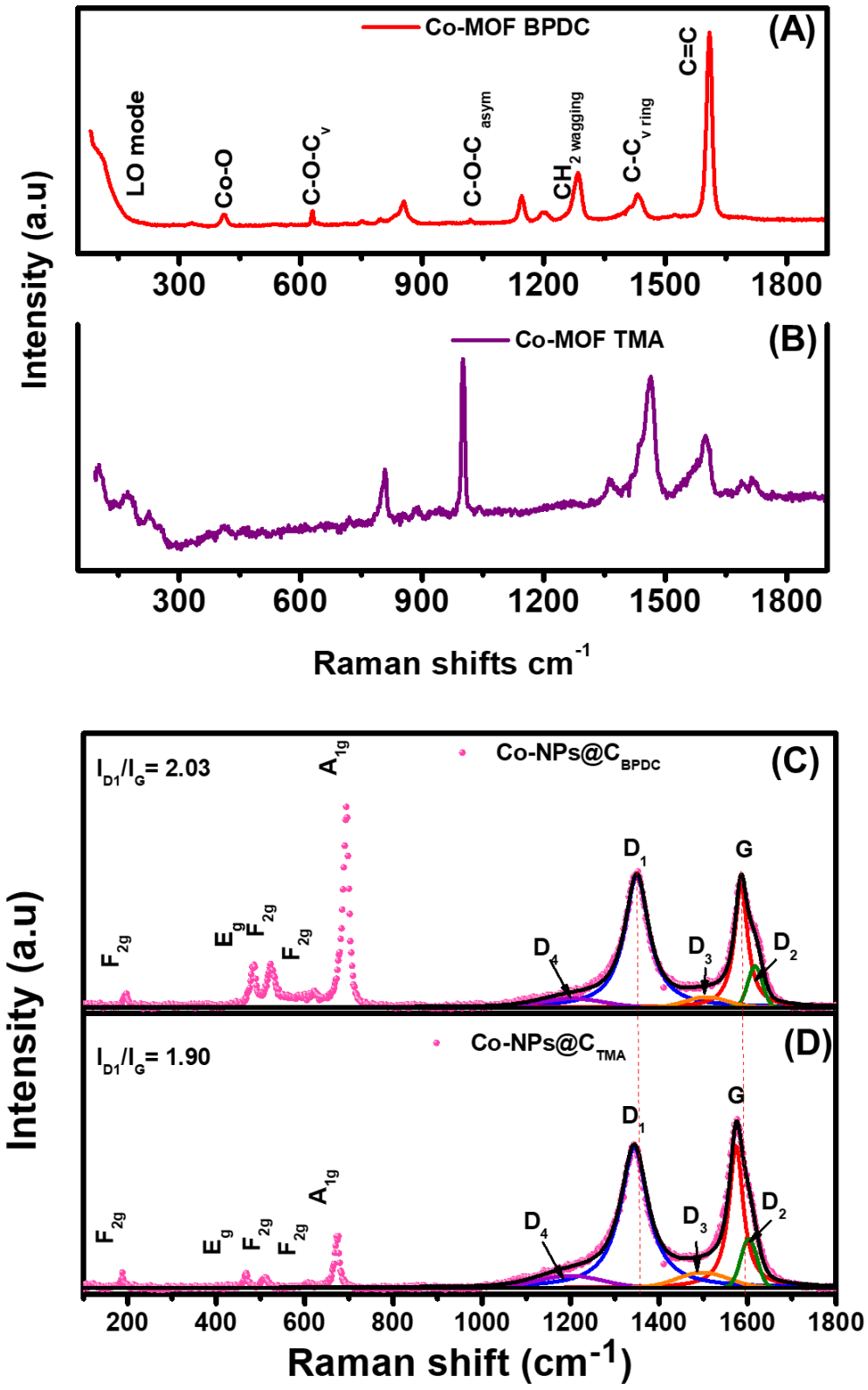


Figure 4.2: Raman spectra of (A) Co-MOF TMA, (B) Co-MOF BPDC, (C) Co-NPs@C_{BPDC} and, (D) Co-NPs@C_{TMA}

4.2.2 X-ray photoelectron spectroscopy (XPS)

X-ray photoelectron spectroscopy (XPS) was used to characterize surface composition and the valance state of Co. The $Co2p_{1/2}$ were deconvoluted to two peak corresponding to Co^{3+} and Co^{2+} at 797.05 eV and 795.23 eV, and the $Co2p_{3/2}$ was also deconvoluted to two peaks at 781.12 eV and 779.78 eV, corresponding to Co^{3+} and Co^{2+}, respectively, along with a Co^{0} peak observed at 778.20 eV for Co-NPs@C_{TMA} [115,116]. For Co-NPs@C_{BPDC} the $Co2p_{1/2}$ peaks were observed at 796.34 eV and 794.61 eV corresponding to Co^{3+} and Co^{2+}, while the peaks for $Co2p_{3/2}$ the peaks were observed at 780.87 eV and 779.62 eV for Co^{3+} and Co^{2+}. The Co2p reveals that, for Co-NPs@C_{BPDC} were slightly shifted towards lower binding energy (i.e. upshifted the d-band center), showing that electrons (generated by BPDC) were migrated to Co^{3+} causing it to be reduced to Co^{2+}, see Figure 4.3(A) and (B). The O1s spectra shown in Figure 4.3(C) and (D), shows three peaks at 532.52 eV, 531.19 eV and 529.71 eV and were assigned to adsorbed oxygen, oxygen vacancies and lattice oxygen, respectively for Co-NPs@C_{TMA}. For Co-NPs@$C_{BPDC,}$ the peaks were observed at 532.89 eV for adsorbed oxygen, at 530.84 eV for oxygen vacancies and 529.57 eV for lattice oxygen [117], with more oxygen vacancies than Co-NPs@C_{TMA}. The C1s were deconvoluted to give peaks at 285.6, 285.7, 284.6, and 284.2 eV corresponding to C=O, C-O, C-C sp_3, and C-C sp^2, respectively for both synthesised materials, see Figure 4.3(E) and (F).

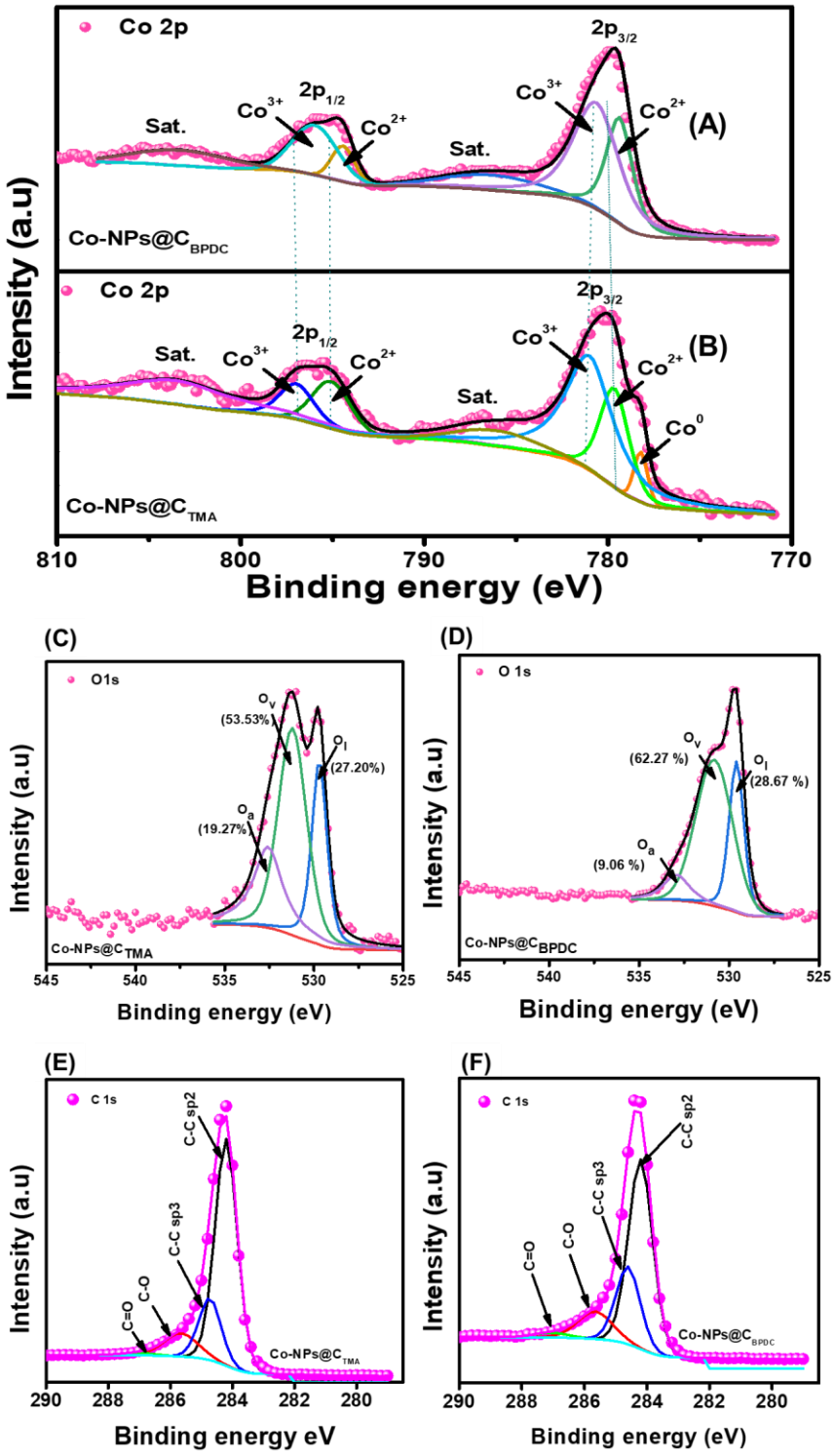


Figure 4.3: Deconvoluted spectras of (A) and (B) Co2p of Co-NPs@C_{TMA} and Co-NPs@C_{BPDC}, (C) and (D) O1s of Co-NPS@C_{TMA} and Co-NPs@$C_{BPDC,}$ respectively and (E) and (F) C1s of Co-NPs@C_{TMA} and Co-NPs@C_{BPDC}, respectively

4.2.3 SEM

Figure 4.4 shows the SEM of the parent MOFs, (A) TMA, (B) BPDC. As can be seen from Figure 4.5(A) TMA MOF shows stacked rod-like morphology, while (4.5(B)) BPDC MOF showed a fluffy looking material. Upon calcining at 800 ºC for 5 hrs, a change in both parent MOFs morphology was observed. CoNPs were observed for both (see Figure 4.5 (D and E), confirming a change on morphology after subjection to heat as can be seen for both in raman and XRD.

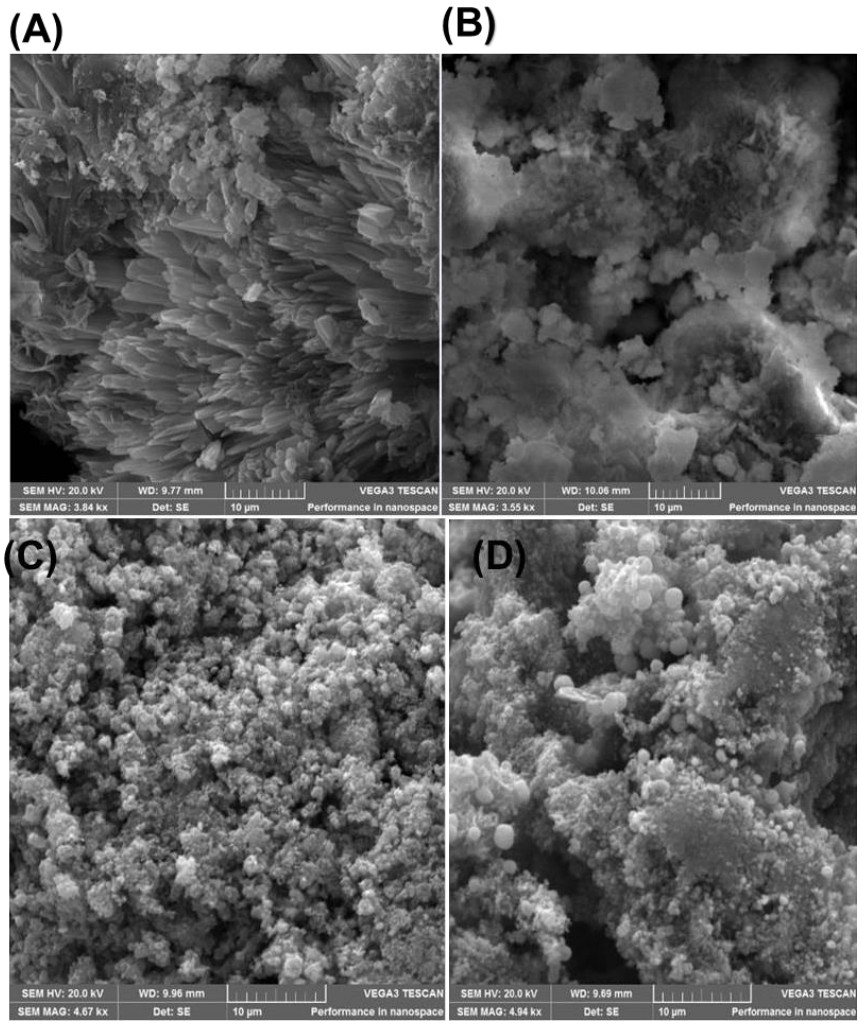


Figure 4.4: Scanning electron microscope images of (A) Co-MOF TMA (B) Co-MOF BPDC, (C) Co-NPs@C_{TMA}, (D) Co-NPs@C_{BPDC}, respectively

4.2.4 EDX

The EDX shows Co, O, C the expected elements in their places respectively. The Pd, Au was from the coating used. Figure 4.5 shows the elemental composition (A) Co-MOF TMA, and Co-NPs@$C_{TMA.}$ Before pyrosis of MOF, higher cobalt content was observed and lower carbon content after pyrosis, an increase in carbon content and a decrease in cobalt content were observed. These observations are due to the structural transformation from MOF to Co-NPs@C. Similar observations were noted for Co-MOF BPDC and Co-NPs@$C_{BPDC.}$

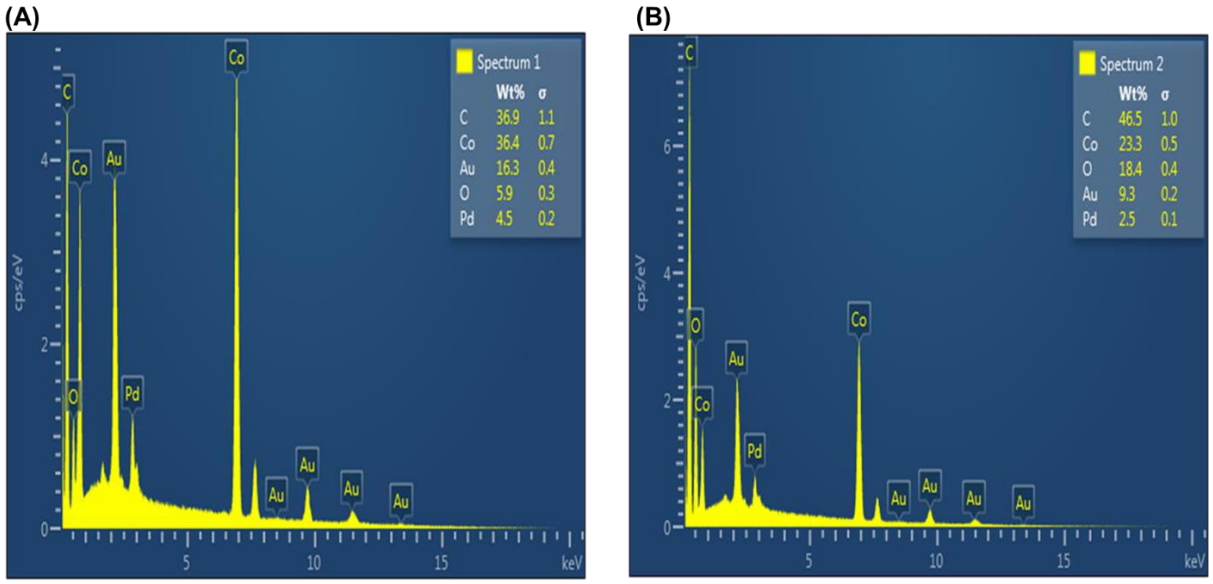


Figure 4.5: Energy dispersive x-ray spectra of (A) Co-MOF TMA, and (B) Co-NPs@C_{TMA}

4.2.5 HRTEM,

HRTEM images of (A) Co-NPs@C_{TMA}, (C) Co-NPs@C_{BPDC} at 50 nm and (B) and (D) at 5 nm are shown in Figure 4.6, respectively. The images shows that both materials (A and C) were highly agglomerated with no definite shape. At higher magnification lattice fridges were observed. On a closer look at the HRTEM, it is quite evident that

the material formed a core shell, with carbon making the shell while cobalt nanoparticles made up the core. The d-spacing of the lattice fridges were calculated for Co-NPs@C_{TMA} were at different spots I and II with are values of 0.255 nm and 0.256 nm corresponding to the CoNPs {111} phase. For Co-NPs@C_{BPDC}, the latter was done and from two spots III and II the d-pacing were 0.228 and 0.274 nm which corresponded to CoNPs {111} phase.

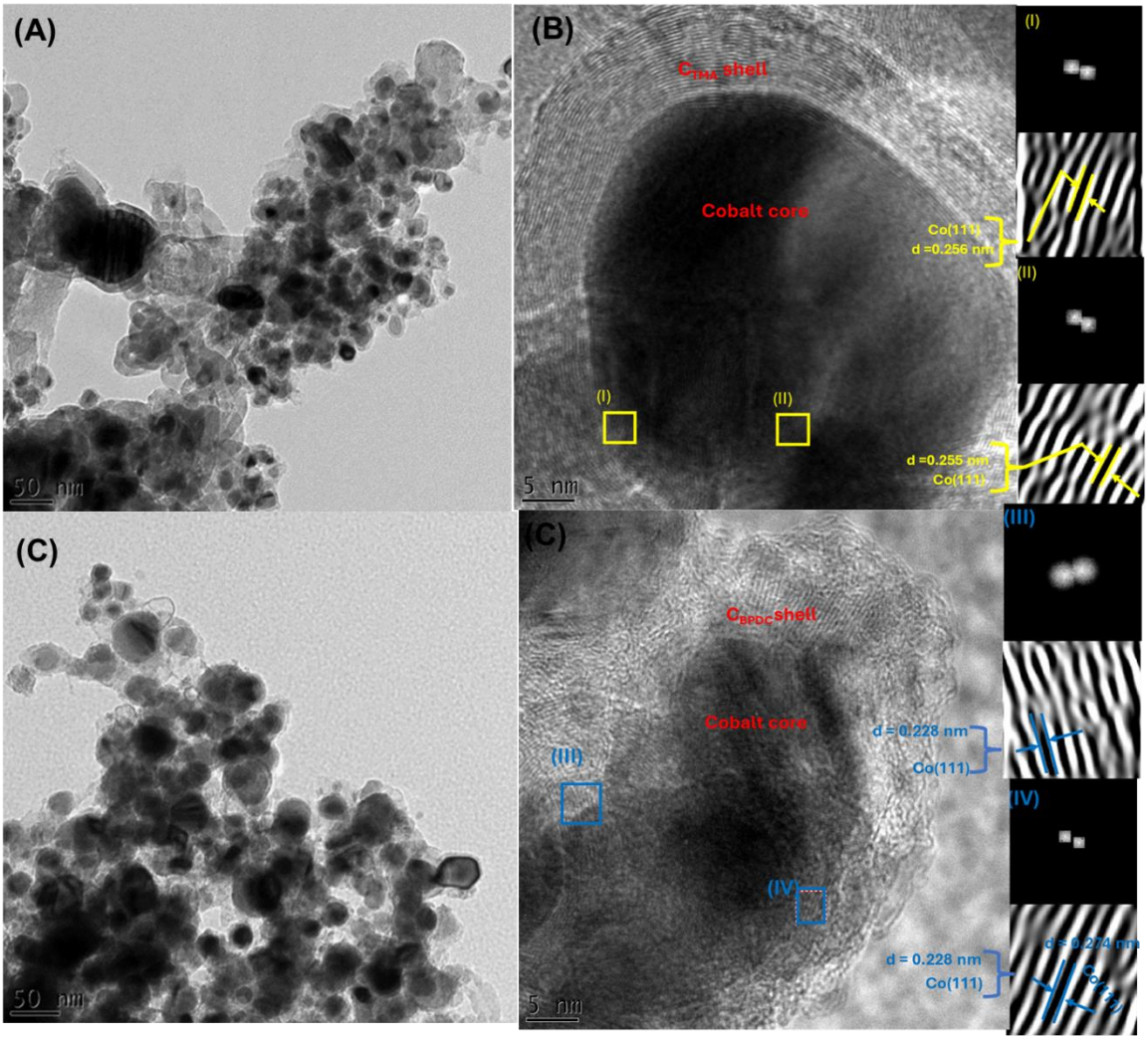


Figure 4.6: High resolution transmission microscopic images of (A) Co-NPs@$C_{TMA,}$ (C) Co-NPs@C_{BPDC} at 50 nm and, (B) Co-NPs@C_{TMA} with (I) and (II) fft and its corresponding inverse fft and (D) Co-NPs@C_{BPDC} with (III) and (IV) fft and its corresponding inverse fft at 5 nm, respectively

4.2.6 Surface area and Pore volume

N_2 adsorption-desorption was evaluated for the characterisation of inner structural properties (pore size, pore volume) and specific surface area of Co-NPs@C_{TMA} or Co-NPs@C_{BPDC} at 77 K. As shown in Table 4.1, Co-NPs@C_{BPDC} was found to have a higher specific surface area and low pore volume compared to Co-NPs@C_{TMA}. Both showed mesoporous pore sizes. The high surface area and porous nature of the material will aid in the diffusion of analytes during electrochemical measurements.

Table 4.1: The results BET surface area of Co-NPs@C_{TMA} and Co-NPs@C_{BPDC}

Electrocatalyst	Specific surface area (m^2/g)	Pore volume (cm^3/g)	Pore size (nm)
Co-NPs@C_{TMA}	**62.139 ± 0.1878**	**0.1959**	**12.610**
Co-NPs@C_{BPDC}	**129.448 ± 1.080**	**0.3357**	**10.375**

4.3 DFT calculations

4.3.1 Predicting of electrochemical interaction of Co{111} and Co{200} towards MN

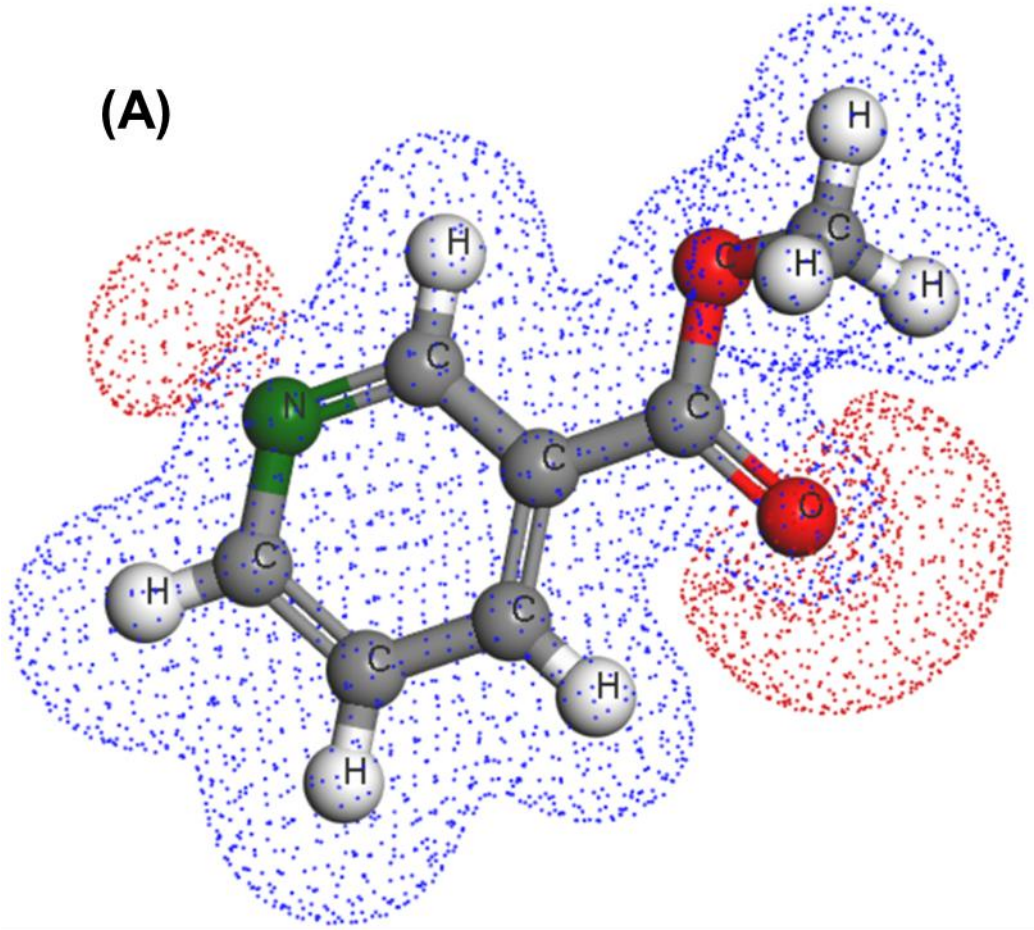


Figure 4.7: Isosurface Potentials@+/- 0.039564 isovalue(a.u.), {blue (+) and red (-) shades for Methyl nicotinate Oxygen has higher –ve potential compares to Nitrogen

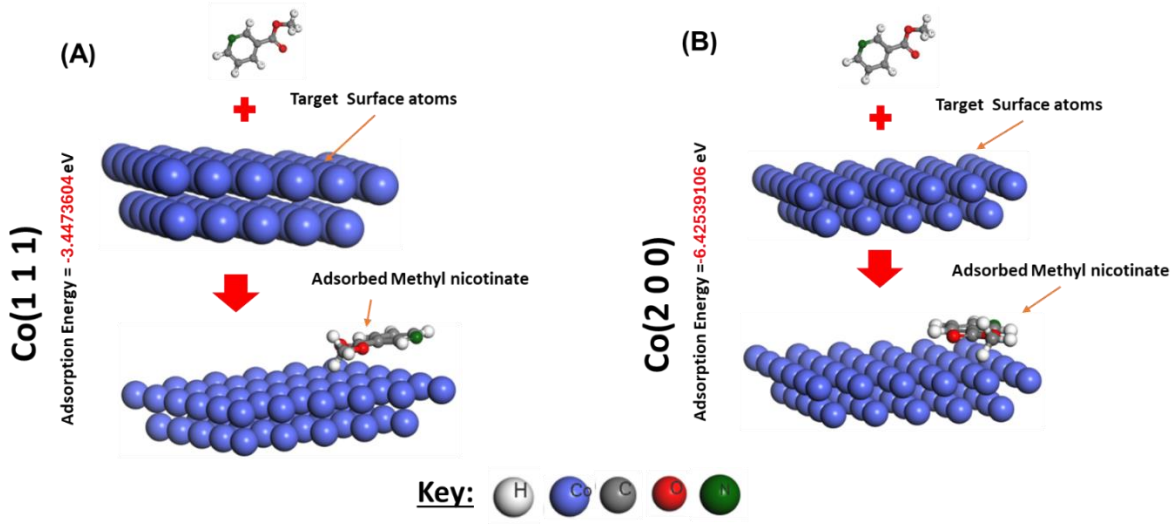


Figure 4.8: Adsorption sites of methyl nicotinate at the surfaces of Co{111} and Co{200}.

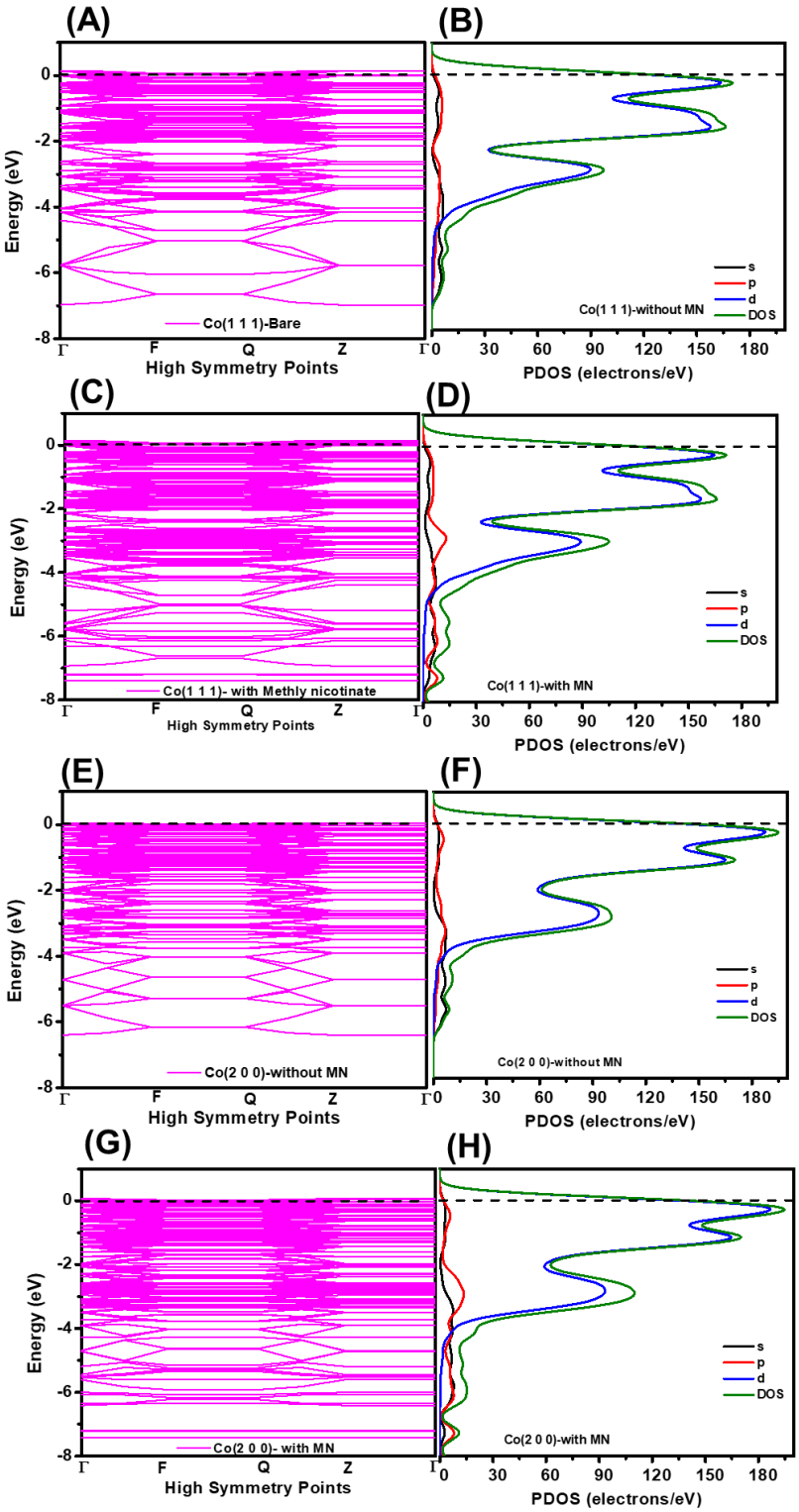


Figure 4.9: Partial density of states of Co{111}; (A) and, (B) before adsorption of MN and, (C) and (D) after adsorption of MN and, of Co{200}; (E) and, (F) before adsorption of MN and (G) and (H) after adsorption of MN, respectively.

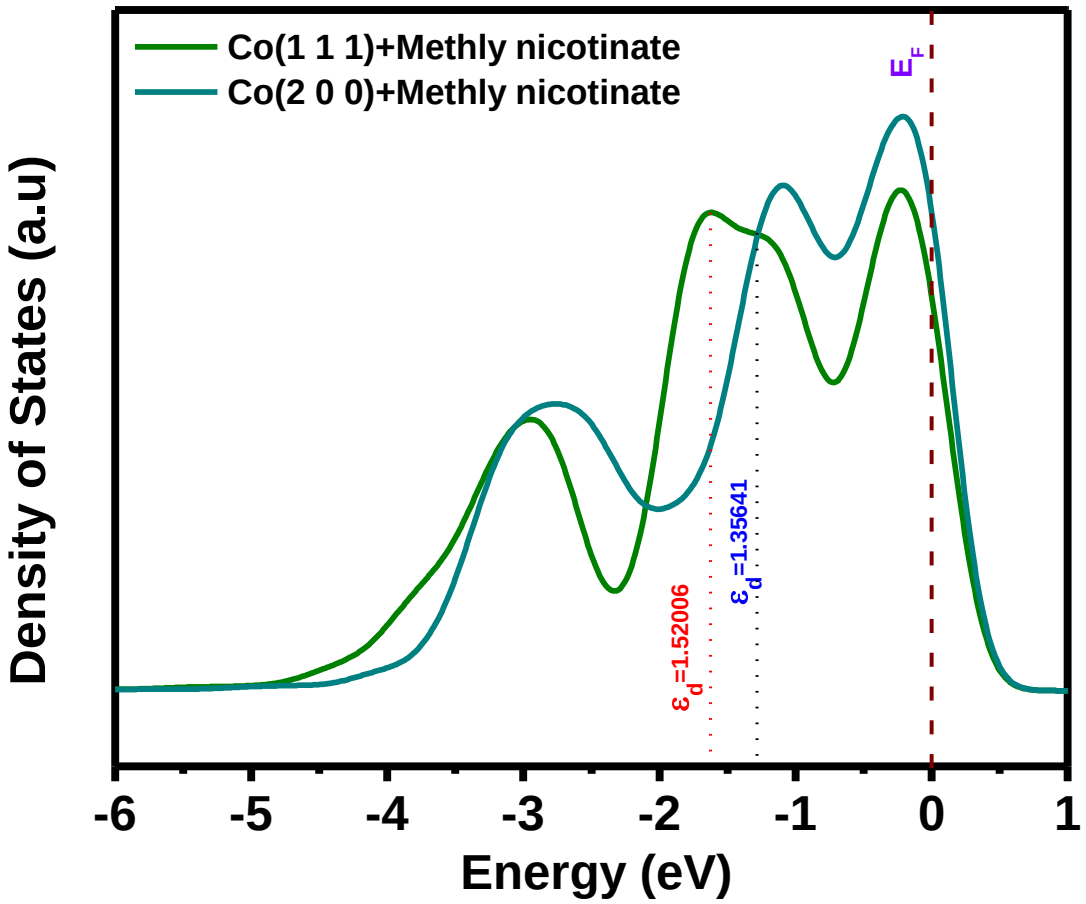


Figure 4.10: D-band centres of Co{111} and Co{200}

From the isosurface potential, oxygen has higher negative potential (red shades) compared to nitrogen (green shades) see Figure 4.7A, meaning that MN was more likely interacting through oxygen first. It is essential to know the interaction of MN to the catalyst, since no study has covered this scope of work. MN between Co{111} and {200}. Figure 4.8A and B shows the interaction between MN with Co {111} and Co{200} lattices planes. Co {111} and {200} lattices were chosen as the model catalyst surface due to their prominence reflection on the XRD. Co{200} showed more delocalized binding site (indicated by the green small dots) than Co{111}. In the DFT calculation, E_{ads},eV is defined in eq. 4.1 [42,118]

E_{ad}=($E_{surface}$+adsorbate) − ($E_{surface}$+$E_{adsorbate}$) …..(4.1)

where $E_{surface}$ + adsorbate is the total energy of the interacting catalyst surface and the adsorbate and $E_{surface}$ + $E_{adsorbate}$ is the energies of the bare catalyst surface (Co{111} or Co{200}) and the free adsorbate (MN) in the gas phase. This equation shows that the more negative the E_{ad} value, the stronger the adsorption. The most preferred lattice for binding should possess the weakest adsorption power (E_{ad}, eV) with the MN molecule. The DFT results show that E_{ad} give the least negative values for Co{200}–MN (A.E = -165.0209142) followed Co{111)-MN (A.E = -165 .4234832 eV). Weak adsorption of adsorbate is most preferred in electrocatalysis, thus the weaker adsorption of MN onto Co {200} compared to Co{111} catalytic lattice predicts better electrocatalysis on Co{200} than on Co{111}. To understand the electronic properties of MN on Co{111} and, Co{200}, before and after the adsorption, DFT calculations on the electronic band structures and the projected density of states (PDOS) were carried out (Figure 4.10). Prior to the adsorption of the MN molecule the onto Co {111} and, Co{200} all the band structures and PDOS show a lower number of energy states than when MN was adsorbed onto the surface of the catalysts. This shows that more electrons were available on Co{111}-MN, Co{200}-MN lattices than when there is no MN. To further understand, the D-band centres of the two active catalytic lattice planes were compared (see Figure 4.10). A shift towards lower energies was observed for Co{200}, further collaborating the observations seen in Figure 4.8 , also showing that Co{200} was the most catalytically active lattice plane for MN.

4.4Electrochemical studies

4.4.1 Voltammetric responses in ferri/ferrocyanide solution

A selection of cyclic voltammograms for 3 mM $[Fe(CN)_6]^{3/4-}$ in 0.1 M KCl as supporting electrolyte, using different electrode modifications is shown in Figure 4.11. Both the parent MOFs and the Co based materials were used to modify GCE. Bare electrode and parent MOFs showed a peak of the Fe^{3+}/Fe^{2+} redox pair assigned as Ox_1/R_1, with extra two peaks for the parent MOFs due to the $Co^{3+/}Co^{2+}$ pair assigned as Ox_2/R_2. The bare electrode showed a better anodic current compared to the parent MOFs. The low anodic current may be due to the insulating nature of MOFs and this was also reported by Gaolathle et.al. [119]. Some of the important parameters to consider on a CV profile are anodic and cathodic potential (E_{pa} and E_{pc}), anodic and cathodic current response (i_{pa} and i_{pc}), the ratio i_{pa}/i_{pc} shows whether a reaction is reversible, quasi-reversible or irreversible, while ΔE_p is indicative of the heterogeneous electron transfer (HET) of the redox system. The heterogeneous electron transfer (HET) of the electrodes were determined using the peak-to-peak separation (ΔE_p) and was of the order, Co-TMA MOF (345 mV) > Co-BPDC MOF (287 mV) > bare GCE (182 mV) > Co-NPs@C_{BPDC} (139 mV) > Co-NPs@C_{TMA} (137 mV). The four different modifications resulted in varying peak potential separations, indicative of different electron transfer properties. A lower ΔE_p implies good electron transfer ability. The Co-NPs@C_{TMA} showed better HET followed by Co-NPs@C_{BPDC}. The Co-NPs@C_{BPDC} electrode was expected to show better HET since it possessed twice the surface area of Co-NPs@C_{TMA}, but it was not the case, and this could be due to mass transport limitations. The ratio i_{pa}/i_{pc} of bare was 1.025, indicative of a reversible reaction, the parent MOFs had a ratio of 0.6740 and 0.8911 Co-MOF TMA and Co-MOF BPDC, respectively. Co-

NPs@C_{TMA} and Co-NPs@C_{BPDC} had higher ratios of 1.4500 and 1.5980, respectively, indicative of non-reversible system/reaction.

Figure 4.11 also shows that Co-NPs@C_{BPDC} had higher current response of 169 µA at 0.6 V compared to Co-NPs@C_{TMA} at 157 µA at the same voltage window for the Fe^{3+}/Fe^{2+} pair. The Ox1 and Ox2 for Co based electrodes have been masked by the presence of Fe hence the broad the peak at 0.6 V, while Red1 and Red2 are prominent. All electrochemical parameters are summarised in Table 4.2

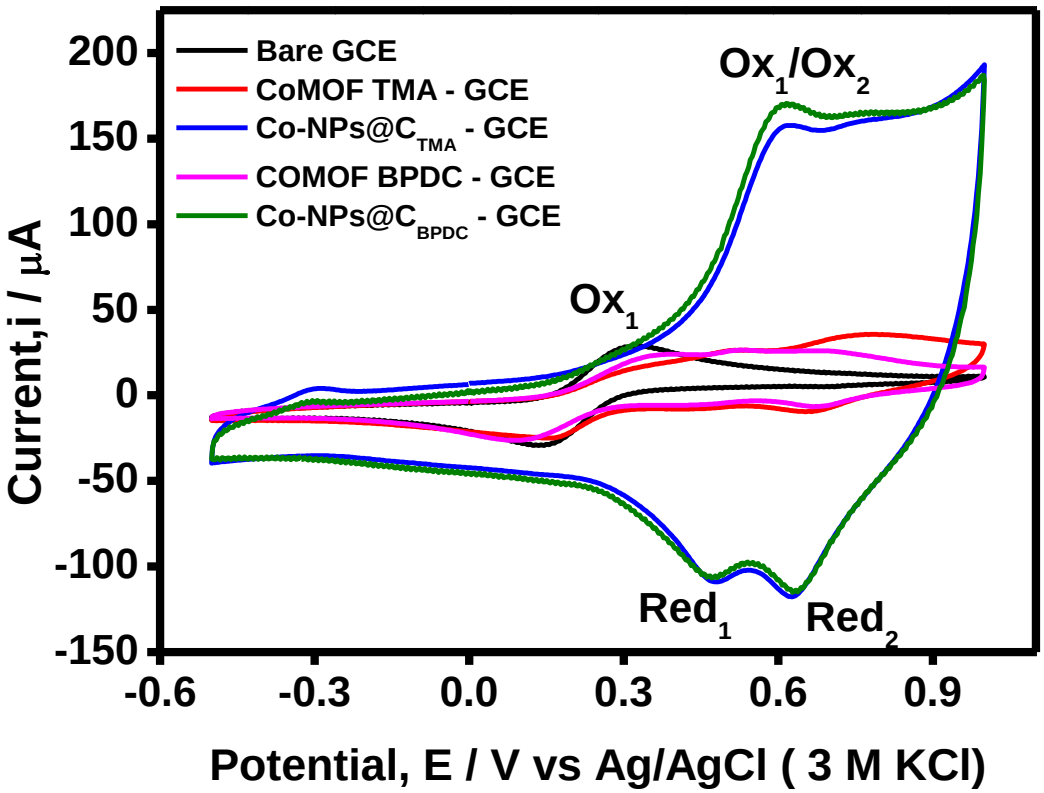


Figure 4.11: Cyclic voltammograms of the modified electrodes in 3 mM $[Fe(CN)_6]^{3/4}$ in 0.1 M KCl, pH 6 at sweeping rate of 20 mV/s

Table 4.2: Summary of electrochemical parameters of electrodes in 3mM $[Fe(CN)_6]^{3/4}$ in 0.1 M KCl

Electrode	E_{pa} (mV)	E_{pc} (mV)	ΔE (mV)	I_{pa} (µA)	I_{pc} (µA)	i_{pa}/i_{pc}
Bare GCE	0.2984	0.1446	154	29.4909	28.7668	1.025
Co-MOF TMA	0.3384	0.1784	160	16.6544	24.7074	0.6740
Co-MOF BPDC	0.3289	0.1398	189	21.9207	24.5977	0.8911
Co-NPs@C_{TMA}	0.6153	0.4803	135	157.5263	108.6381	1.4500
Co-NPs@C_{BPDC}	0.6123	0.4708	142	169.9239	106.3341	1.5980

The scan rate studies were also done to understand the mass transport mechanism of the electrode platforms, see Figure 4.12A (bare GCE), B (GCE-COMOF TMA), and C (GCE-CoMOF BPDC), and Figure 4.13A (GCE-Co-NPs@C_{TMA}), and B (GCE-Co-NPs@C_{BPDC}). A linear relationship between the peak current i_p and scan rate is described by equation 4.2, where i_p is the peak current, n is the number of electrons involved in the electrochemical process, F is a Faradays constant (96.584 C/mol), R is the rate constant (8.314 J/mol.K),T is the absolute temperature (298 K), A is the real surface area of the electrode (cm^2). The other symbols have their usual meaning. The plot of log $|i_p|$ vs log|υ| gave a straight line with slope values of 0.4336 for bare indicative of a diffusion-controlled process, while values of 0.6-1 indicate a mixed system with diffusion and adsorption as seen for Co-NPs@C_{TMA} and Co-NPs@C_{BPDC} with values of 0.6676 and 0.6990, respectively, see Figure 4.13E and F. The plots of i_p and were used to calculate the surface coverage of the electrodes. The surface coverage was calculated to be 0.05148 mol/cm^2 for CoNPs@C_{TMA} and 0.05663

mol/cm^2 for Co@C$_{BPDC}$, see Figure 4.13C and D.

$$i_p = \frac{n^2F^2}{4RT}\nu A\Gamma \quad \ldots 4.2$$

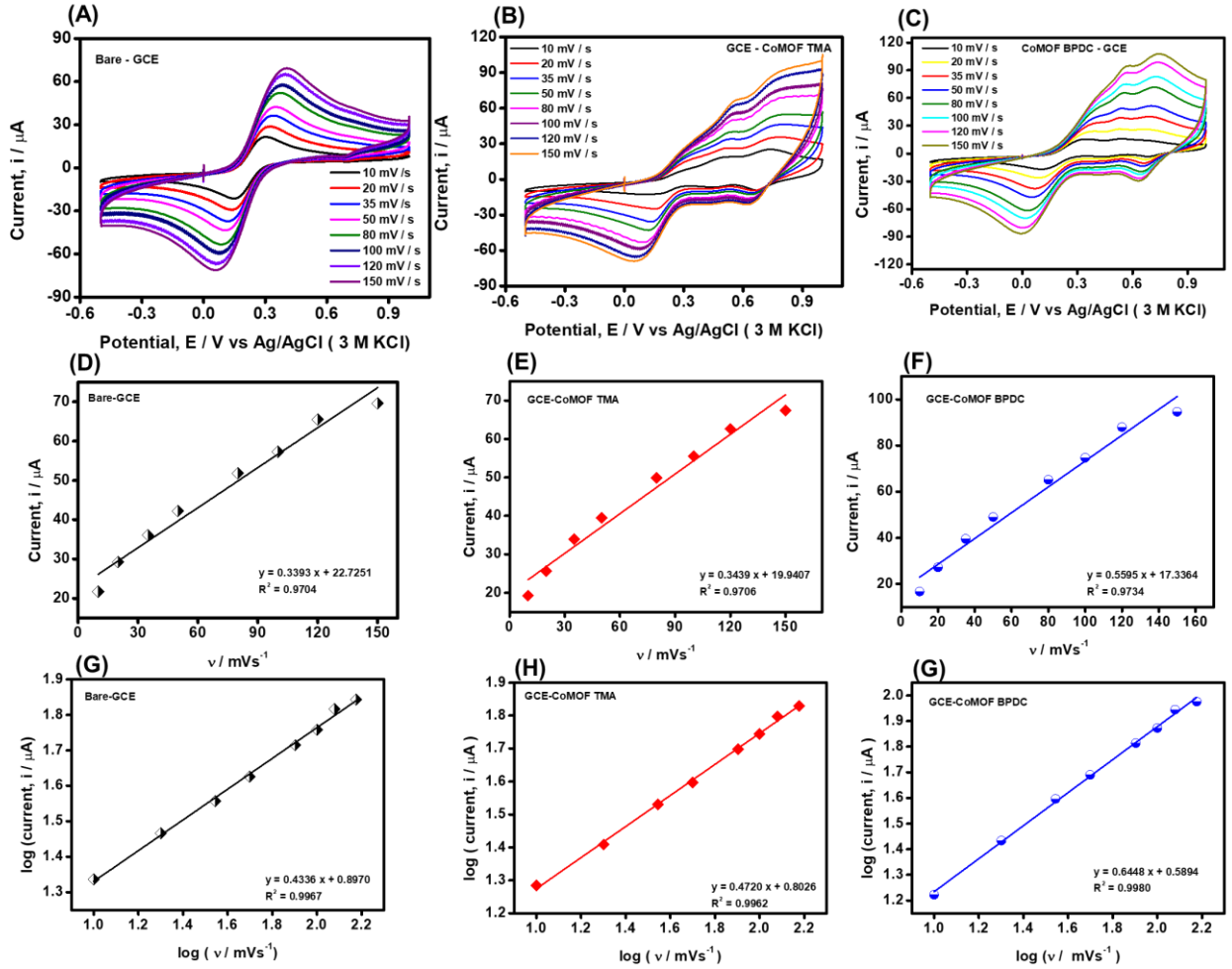


Figure 4.12: Scan rate studies of (A) bare GCE electrode, (B) GCE-CoMOF TMA, (C) GCE-CoMOF BPDC, and υ vs current plots of (D) bare-GCE, (E) GCE CoMOF TMA, (F) GCE-CoMOF BPDC and, log υ vs log current plots (G) bare-GCE, (H) GCE-CoMOF TMA, (I) GCE- CoMOF BPDC, respectively, in 3mM $[Fe(CN)_6]^{3/4}$ in 0.1 M KCl.

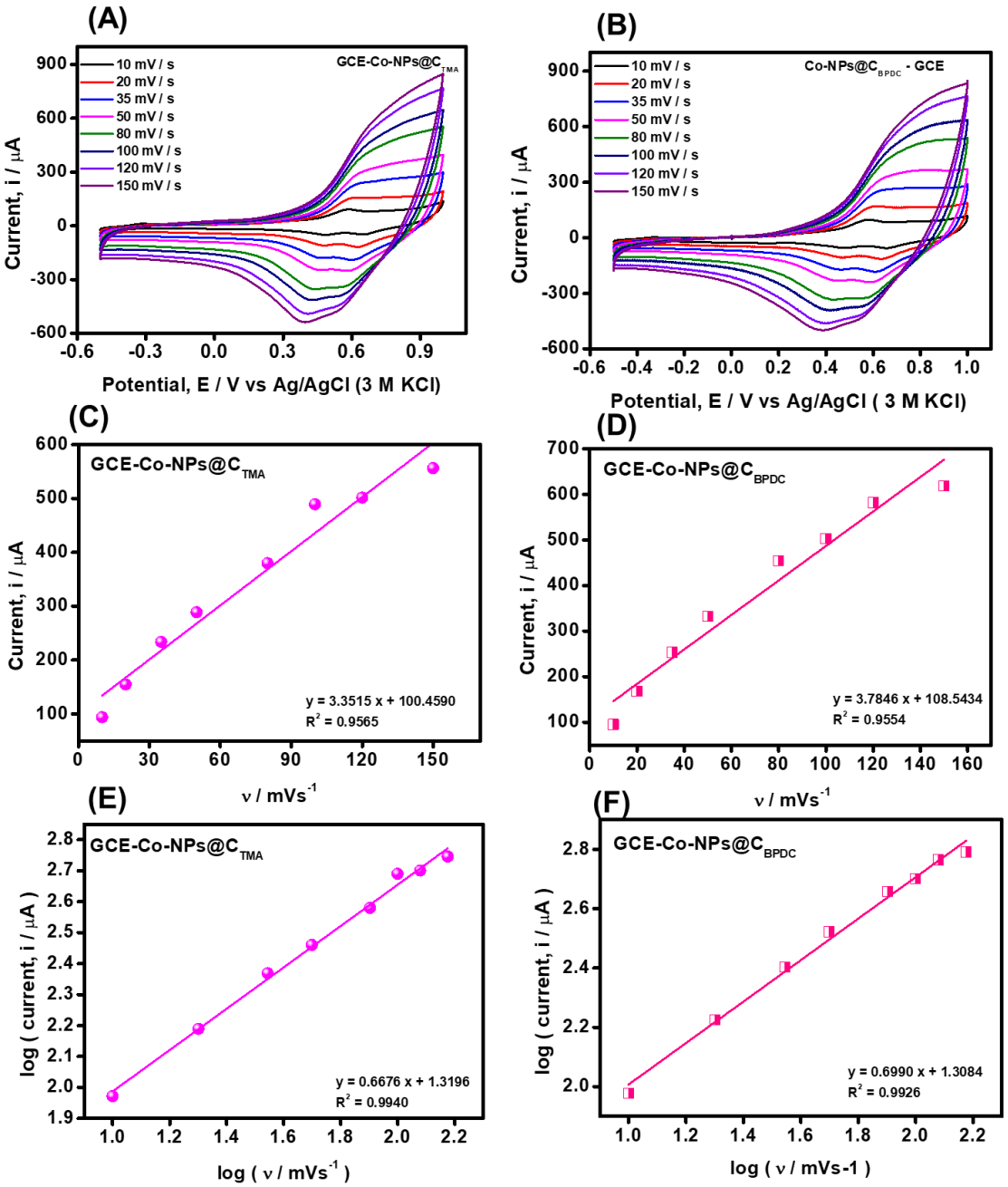


Figure 4.13: Scan rate studies of (A) GCE-Co-NPs@C_{TMA}, (B) GCE-Co-NPs@C_{BPDC}, and υ vs current plots of (C) GCE-Co-NPs@C_{TMA}, (D) GCE- Co-NPs@C_{BPDC} and, log(υ) vs log(current) plots (E) GCE- Co-NPs@C_{TMA} and, (F) Co-NPs@C_{BPDC}, respectively, in 3mM $[Fe(CN)6]^{3/4}$ in 0.1 M KCl

Figure 4.13A and B shows the capacitive nature for Co-NPs@C_{TMA} and Co-NPs@C_{BPDC} based electrodes, this is due to the trapping of the electrolyte inside the pores of the material which also causes an increase in the current response, as the scan rate are increased a highly capacitive nature of the electrodes was observed for both material, this is observed upon increasing the scan rates.

4.5 Methyl nicotinate detection

4.5.1 Cyclic voltammetry

Methyl nicotinate is one of the biomarkers associated with TB, a few studies have been conducted in this area [11,13–16]. In this work, we report on the indirect detection of MN using Co-NPs@C materials derived from MOF. Figure 4.14 shows comparative cyclic voltammograms of: (A) Co-NPs@C_{BPDC} in the absence and presence of MN and, Co-NPs@C_{TMA} in the absence of MN and presence of MN and, (B) insert of bare GCE-MN. The voltammograms show reversible scan for CVs with a cathodic and anodic peak labelled as (I) and (II), showing the Co^{2+}/Co^{0} redox pair (see eq. 4.3) [120][121–123]. In the absence of MN, the anodic peak showed high current responses, however, in the presence of MN, a decrease in the anodic/cathodic current responses was observed, showing that, in the presence of MN, the Co^{2+} interacts with MN and the unreacted/unbound Co^{2+} gets reduced to Co, making the sensor capacitive in the presence of MN, therefore, limiting the electron transport system (see Figure 6 A) [124]. Figure 4.14 (B) insert, shows there were no apparent peaks due to oxidation/reduction of MN, the reduction peak observed was due to the electrolysis of PBS causing hydrogen gas to evolve. So, the peaks observed in the cyclic voltammograms in Figure 4.14(A) were due to cobalt as indicated above. Therefore, this was used as an indirect quantitative detection of MN. Figure 4.14 (C) also compares the CVs of Co-NPs@C_{BPDC} and Co-NPs@C_{TMA} in the presence of MN at

50 mV/s. Although Co-NPs@C_{TMA} showed better electron transfer abilities in ferri-ferro, it showed anodic current response of 77 µA, while Co-NPs@C_{BPDC} electrode showed higher anodic current response of 257 µA at 50 mV/s. The ΔE were 0.229 V vs RHE and 0.2131 V vs RHE, for Co-NPs@C_{TMA} and Co-NPs@C_{BPDC}, respectively. The ΔE values show HET, with Co-NPs@C_{BPDC} showing better electron transport system than Co-NPs@C_{TMA}. The ipa/ipc ratio were 0.830 and 0.547 for Co-NPs@C_{TMA} and Co-NPs@C_{BPDC}, respectively indicative of a quasi-reversible system.

$$Co^{2+} + 2e^{-} \underset{(II)}{\overset{(I)}{\rightleftharpoons}} Co\ldots 4.3$$

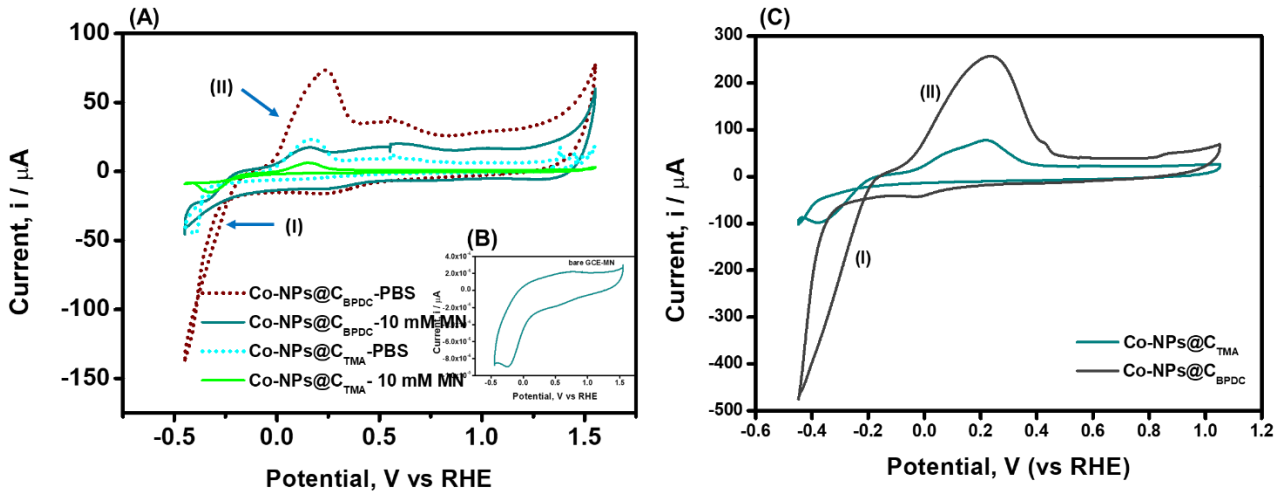


Figure 4.14: Comparative cyclic voltammograms of (A) Co-NPs@C_{BPDC} in PBS and, in MN and, (B) Co-NPs@C_{TMA} in PBS and MN, at 20 mV/s and, (C) Co-NPs@C_{BPDC} and Co-NPs@C_{TMA} in MN solution of pH 6 at 50 mV/s

To further understand the behaviour of the modified electrodes, scan rate studies were conducted. An increase in the anodic current response was observed with increasing scan rates see Figure 4.14 A and B. The plot of anodic current with the square root of scan rate showed a linear relationship for both Co electrodes with slopes and

regression of y = 472.62 x – 46.97, R^2 = 0.9863, and y = 1810.42 x – 97.70, R^2 = 0.9800 Co-NPs@C_{TMA} and Co-NPs@C_{BPDC}, respectively, meaning the reactions at the electrode were diffusion-controlled see Figure 4.16 C. The relationship between peak potential and log scan rate (Figure 4.15 D) for an a quasi-reversible or irreversible diffusion-controlled process is given by Eq. 4.4 (a) and 4.4(b), where a linear relationship for plot E_p vs log υ confirms chemical quasi-reversibility or irreversibility.

$$E_p = \frac{b}{2} log v \ldots 4.4(a)$$

$$b = \frac{2.303RT}{\alpha n_\alpha F} \ldots 4.4(b)$$

where α is the electron transfer coefficient, n_α is the number of electrons involved in the determining rate-determining step, υ is the scan rate, K is a constant, R is the universal gas constant, F is the Faraday constant, T is the temperature (298 K). The plot of E_p vs log υ gave Tafel slopes of 673.4 and 278.8 mV/dec for Co-NPs@C_{TMA} and Co-NPs@C_{BPDC}, respectively. The high Tafel slopes have no significant meaning; slopes above 120 mV/dec are indicative of electrode passivation [125], as is the case with our electrodes.

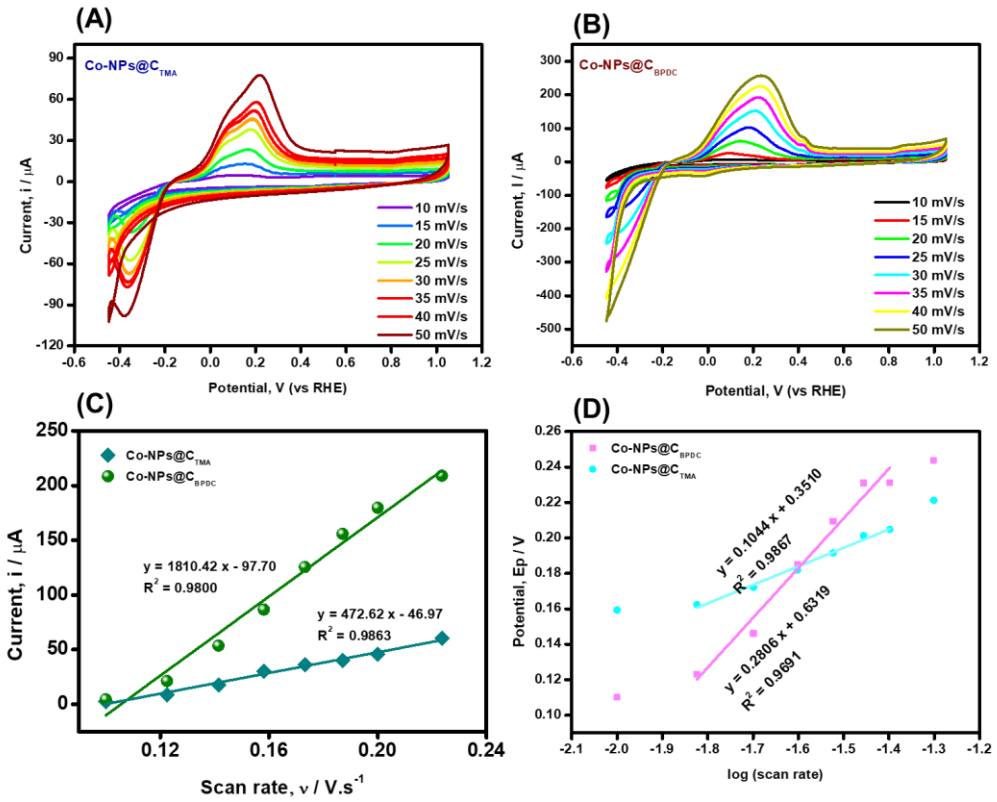


Figure 4.15: Scan rate studies of MN (A) Co-NPs@C_{TMA} (B) Co-NPs@C_{BPDC} (C) scan rate vs current plot of Co-NPs@C_{TMA} or Co-NPs@C_{BPDC} (D) log(scan rate) vs potential plots of Co-NPs@C_{TMA} or Co-NPs@C_{BPDC}, respectively.

4.6 Limit of detection and sensitivity studies

To verify the possibility to develop MN sensor, differential pulsed voltammetry (DPV) was done of the modified electrodes. Using Co-NPs@C_{BPDC} and Co-NPs@C_{TMA} electrodes, via a serial dilution method using concentrations of 0.06 – 0.20 mg/mL was done using DPV. Prior to the addition of MN, PBS alone was measured which showed an oxidation peak at ~0.35 V vs RHE, which was attributed to the oxidation of cobalt, upon additions of MN, a decrease with each addition was observed. The decrease in current with the additions of different concentrations of MN, show that the sensor becomes more capacitive or adsorptive, see Figure 4.16 A and B. The reason for the observed decrease in current responses was due to the complex formation between

MN and Co(II) , therefore blocking the electron transfer and also decrease the active surface area [124]. A second unknown peak was observed on both catalysts, as concentrations increased. The current response vs concentration plot was obtained by using the difference of blank to each concentration (Δi / μA). The linear regression equations are summarised as follows: y = 49.4049x (±1.2551 mg.mL^{-1}) + 1.9110 (±0.1730) with R^2 = 0.9955 and y = 77.4726x (±1.4615 mg.mL^{-1})– 4.3949 (±0.1849) (R^2 = 0.9982), Co-NPs@C_{TMA}, and Co-NPs@C_{BPDC} respectively. Both catalysts showed a wide concentration range from 0.06-0.20 mg.mL^{-1}. From the regression equations, the limit of detection was determined using LoD = 3s/ m, where m is the slope of the linear plots and s is the relative standard deviation of the intercept on the y–axis. The limit of detection was found to be 470.50 nM for Co-NPs@C_{TMA} and 147.64 nM for Co-NPs@C_{BPDC}, respectively. The LODs are quite low compared to what was reported in a similar work (see Table 4.3). Co-NPs@C_{BPDC} showed lower LOD; this can be attributed to many factors such as high surface area, defect richness etc. compared to Co-NPs@C_{TMA}. The LOQ was determined using LOQ = 10s/m, where s and, m variables are defined above. The LOQ were 1.5863 μM for Co-NPs@C_{TMA} and 0.4961 μM for Co-NPs@C_{BPDC}, respectively. Concentration studies were also done in serum to mimic a human-like system. Figure 4.16 also showed that in MN was still detectable for both Co-NPs@/C_{TMA}, and Co-NPs@C_{BPDC}, at 0.14 mg / mL MN was detectible in serum at approximately the same current response as in PBS, showing the possibility of using this sensor for the detection of MN in blood. So, the possible mechanism involved between Co-NPs and MN was, the cobalt in PBS existed as Co^{2+}, due to the strong interactions between oxygen and nitrogen containing molecules to Co^{2+}, MN easily interacted with Co^{2+} forming MN-Co complex. Co has been reported to be the front runner in this reaction as previously reported by Bairagi et.al. and others [11,12,14].

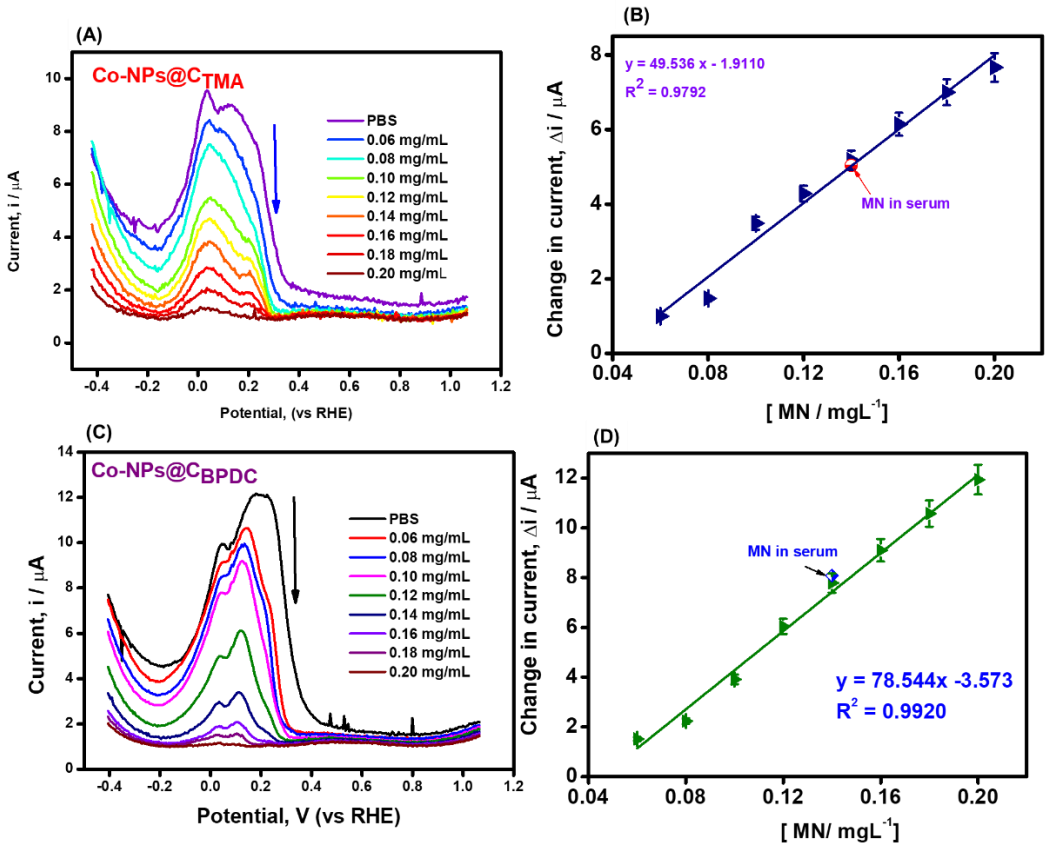


Figure 4.16: Concentration studies of MN using differential pulsed voltammogram for (A) Co-NPs@C_{TMA} and its concentration vs change in current plot (B), and (C) Co-NPs@C_{BPDC} and its concentration vs change in current plot (D), respectively.

4.6.1 Selectivity studies

Selectivity studies were used to determine the selectivity of the electrodes in the presence of commonly found chemical species in blood, such as ascorbic acid (AA) and uric acid (UA). The interfering species were three times the concentration of MN (60 mg in 100 mL:20 mg / 100 mL). For Co-NPs@C_{TMA}, the oxidation peak of AA and UA without MN are shown at 0.55 V and 0.98 V, respectively. In the presence of MN, the AA oxidation peak was not showing, and the AU oxidation peak strangely increased. For Co-NPs@C_{BPDC}, the oxidation peak of AA and UA without MN are shown at 0.55 V and 0.98 V, respectively. In the presence of MN, the AA oxidation peak was shifted to higher potentials with no enhancement in the current response, and the AU oxidation peak strangely decreased, meaning MN was strongly binding to Co, making less of Co available to catalyse the oxidation of AA and AU. Its worth noting that, in the presence of the interferants, it can be seen in Figure 4.17 that MN was detectible, although there was a slight decrease in the original anodic current for Co-NPs@C_{TMA}, while there was a slight enhancement for Co-NPs@C_{BPDC}. These results show that MN can still be detectable in the presence of other interfering species.

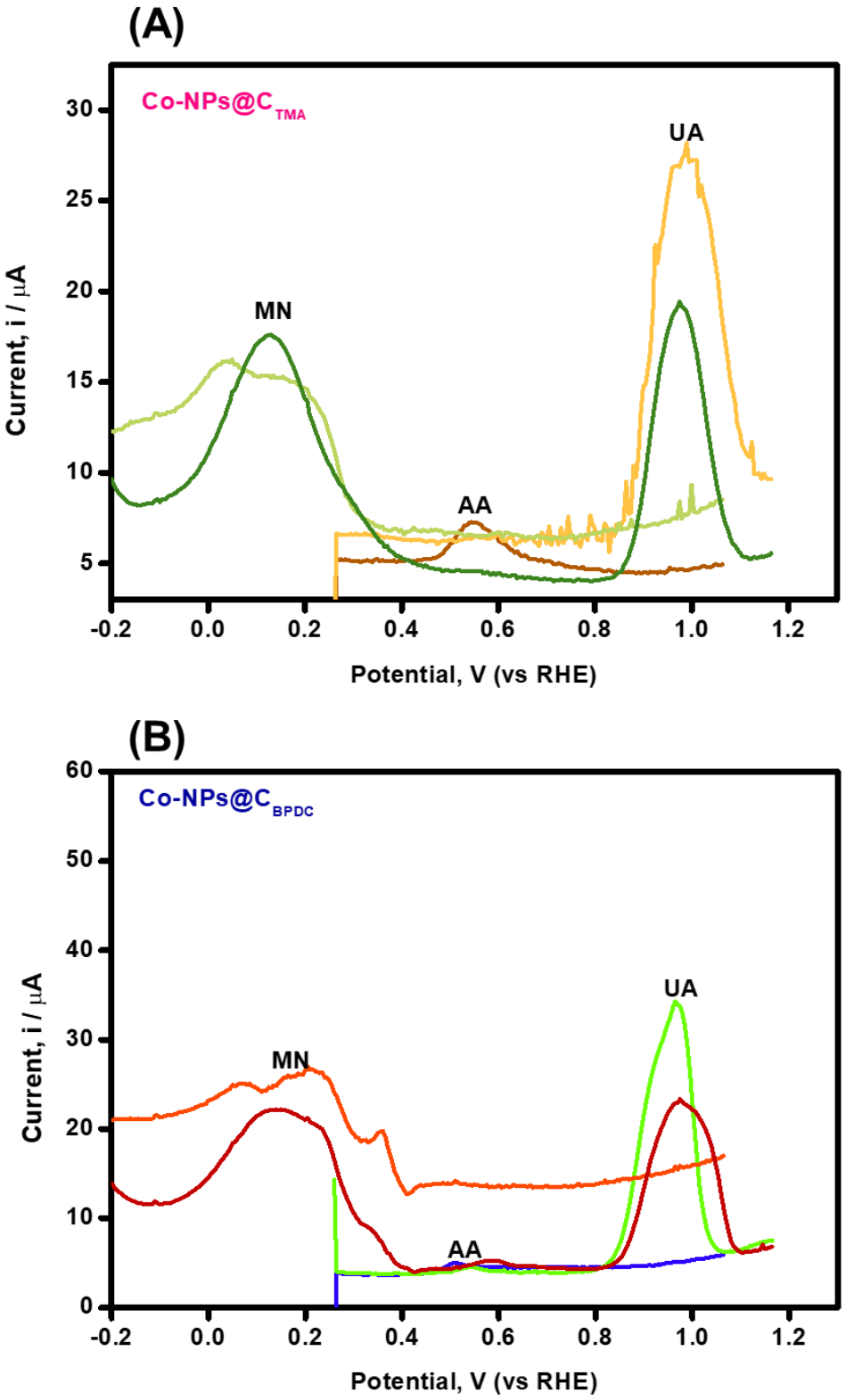


Figure 4.17: Differential pulsed voltammogram of MN, AA and UA (A) Co-NPs@C_{TMA}, and (B) Co-NPs@C_{BPDC}

Table 4.3: Comparative studies MN-based studies with different material

Electrodes	pH	Technique	Conc. range	LOD	LOQ	Ref.
Co-RGO/P*(C)/GCE	6	DPV	0.15-14 mg/L	1.2 µM	N/A	[14]
La_2O_3@SnO_2/rGO/GCE	7	DPV	0.035–522.9 µM	19.7 nM	N/A	[15]
Co-NPs@C_{TMA}	6	DPV	0.04-0.12 mg/L	0.47 µM	1.59 µM	This work
Co-NPs@C_{BPDC}	6	DPV	0.04-0.18 mg/L	0.15 µM	0.50 µM	This work

4.7 Preliminary gas sensing

The ability of the sensor to test MN in gaseous form was done using a CSPE, and the experimental setup is shown in Figure 4.18**.** Before the experiment, the CSPE was dipped in PBS, and in a conical flask, MN (100 mg) was dissolved in 50 mL of ethanol. Using nitrogen as a carrier gas, it was bubbled in the homogeneous solution, and the generated gas was transported through the outlet to the surface of the CSPE. Figure 4.19A shows the evolution of CVs (Co-NPs@$C_{BPDC,}$ this was chosen as it showed better results in PBS), the CSPE with MN showed a capacitive behaviour with poor current response and no oxidation peak. Upon modification with Co-NPs@C_{BPDC} (which was chosen because it showed better catalytic activity), an oxidation peak was observed, and an increase in current response was also observed. The scan rate studies were carried out; as the scan rate was increased, the CVs became more and more capacitive for CSPE-Co-NPs@C_{BPDC} and there was a shift in the oxidation peaks, showing that the reaction was quasi-reversible. The concentration studies were conducted using LSV, upon increasing the concentration of MN, an increase in the oxidation current (i_c) was observed, see Figure 4.20. Although this is not conclusive, much work still needs to be done on gas detection, but it is worth mentioning that this study is quite promising.

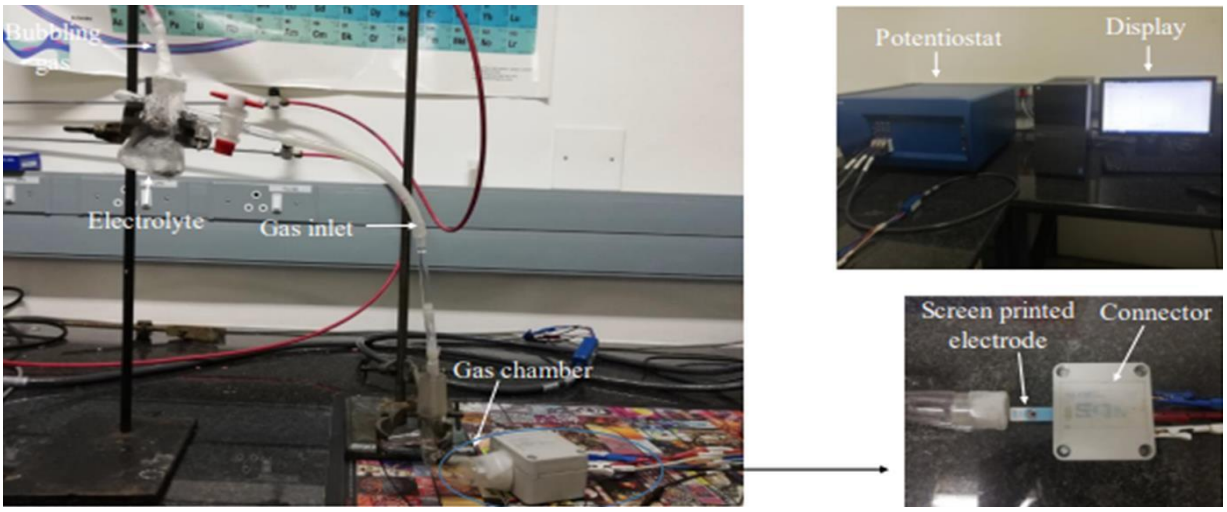


Figure 4.18: Gas sensing set up for detection of MN (picture adapted from [126])

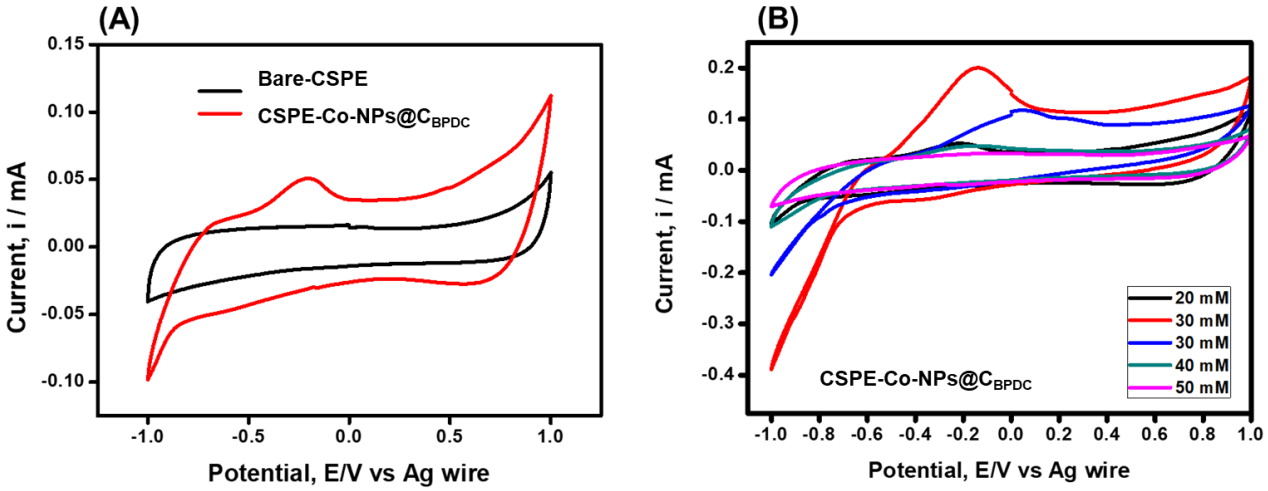


Figure 4.19: Scan rate studies of (A) CSPE (black, with MN), and CSPE- (red, with MN) (B) Scan rate studies of CSPE-Co-NPs@C$_{BPDC}$ with MN

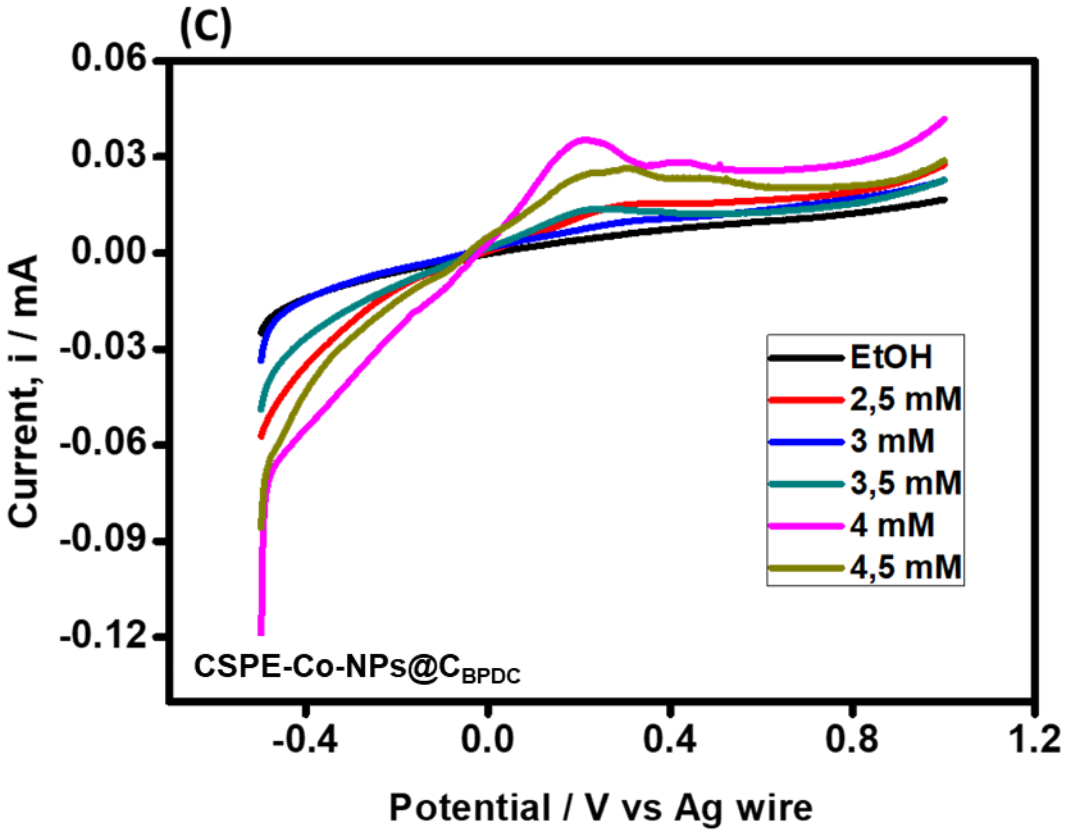


Figure 4.20: Linear scanning voltammogram showing the concentration studies of Co-NPs@C$_{BPDC}$

4.8 Conclusion

Cobalt based MOFs were successfully synthesized and were later used as sacrificial templates for Co-NPs@C using pyrolysis, these MOFs contained ligands of different lengths (trimesic acid (TMA)– shorter length and biphenyl dicarboxyluc acid (BPDC) – longer length). Various techniques were used to characterize the material. XRD confirmed that the structures that were formed were Co nanoparticles with traces of CoO. The Co-NPs@C$_{BPDC}$ was shifted towards lower 2θ degree angles compared to Co-NPs@C$_{TMA}$. The XPS also showed that Co-NPs@C$_{BPDC}$ showed more oxygen vacancies than Co-NPs@C$_{TMA}$. HRTEM confirmed that the synthesised material was a core shell, with carbon being the shell and Co-NPs forming the core. Using DFT, it was shown that Co{200} was the most catalytic plane towards MN and with the least activation energy, and binding energy which is most preferred. Two electrode platforms were made with Co-NPs@C$_{TMA}$ and Co-NPs@C$_{BPDC}$ with GCE. The two sensors

were used for the detection of MN. The LOD for Co-NPs@C_{BPDC} was 0.15 μM performing better than Co-NPs@C_{TMA} with 0.45 μM. It is clear that the two MOF derived Co-NPs@C resulted in materials with different structural defects which made Co-NPs@C_{BPDC} superior than Co-NPs@C_{TMA} in performance. The ability of the sensor to detect MN in the presence of other commonly found biochemicals such as AA and AU was done. It was found that the sensor still had the ability to detect MN, in fact an enhancement in the current response was observed. The sensors ability to be detect MN in serum was also done, and at concentration 0.14 mg/mL MN was detected, this at same concentration as the PBS. This is not only promising but also calls for more work to be done in this area.

Chapter Five

Electrochemical detection of HPV-16 L1 antigen and antibody

This chapter gives a detailed discussion on the physicochemical techniques done for OLC and OLC-PAN materials. The material was used to detect both antigen and antibody of human papilloma virus (HPV).

5.1 Brief introduction

HPV is associated with many cancers, with over 200 HPV genotypes; in this work, we will be looking at a high-risk HPV-16 L1. The reason for our choice of genotype was informed by what has been reported in the literature that it has been found in many cervical cancer cases. For a detailed discussion on HPV, please refer to Chapter One.

5.2 .1 Physicochemical characterisation

This section discusses physicochemical characterization methods such as TEM, SEM, XRD, Raman, and surface analysis.

5.1.2 TEM and SEM Characterisation

HRTEM images are shown in Figure 5.1A for OLC and Figure 5.1B for OLC-PAN. The HRTEM image of OLC is interconnected graphitic layers, which resemble onion-like rings with the outside layers connected to form an oval-like shape, while the OLC- PAN does not show any distinct shape. The SEM images of OLC and OLC-PAN are shown in Figure 5.1C and D**,** respectively. The morphology of OLC is agglomerates of nanoparticles, while the OLC-PAN shows rough and smoothened surfaces, the PAN surface's roughness confirms the OLC's successful incorporation onto the PAN

matrix.

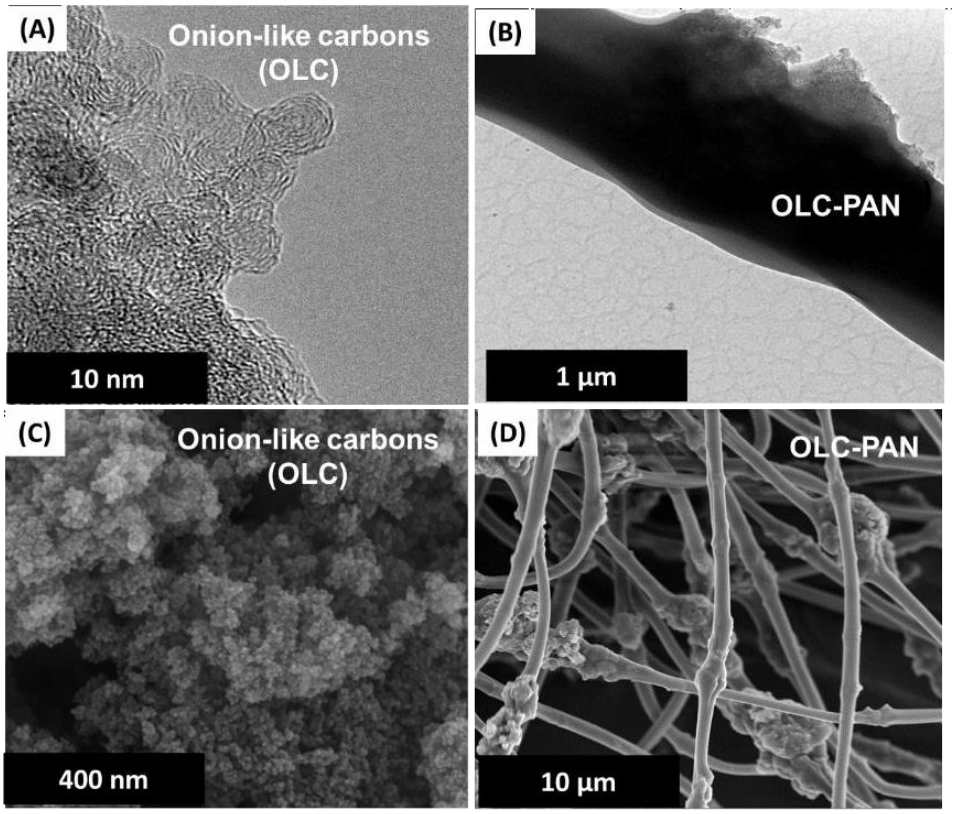


Figure 5.1: TEM images of (A) OLC and (B) OLC-PAN, SEM images of (C) OLC and (D) OLC-PAN

5.1.3 X-ray diffraction and raman spectroscopy

Figure 5.2A compares the powder XRD patterns of the OLC and OLC-PAN. The OLC shows two distinct peaks at 2θ of ~ 26.4 and 44.0° corresponding to the amorphous (i.e., (002) plane) and crystalline graphite (i.e., (101) plane), respectively. The OLC-PAN, on the other hand, shows the same peaks as the OLC, but with an extra peak at 2θ = 17.1° that corresponds to the (100) plane of the polymer. The XRD of the OLC-PAN confirms the presence of the OLC. Figure 5.2B compares the Raman spectra of the OLC and OLC-PAN. Both OLC and OLC-PAN show the two characteristic distinct D (defect) band due to the out-of-plane vibrations of sp^2-bonded carbons, and G(graphitic) band arising from the in-plane vibrations of the sp^3-bonded carbons. The D and G bands were observed at 337.4 and 1593 cm^{-1} for the OLC, respectively, while

those of the OLC-PAN appear at 1347.9 and 1598.2 cm^{-1}, respectively. The degree of graphitization was determined using the conventional I_D/I_G ratio. The I_D/I_G ratio of OLC-PAN was 1.97 compared to the OLC of 1.95, indicating that the OLC-PAN is slightly more defective than the OLC alone.

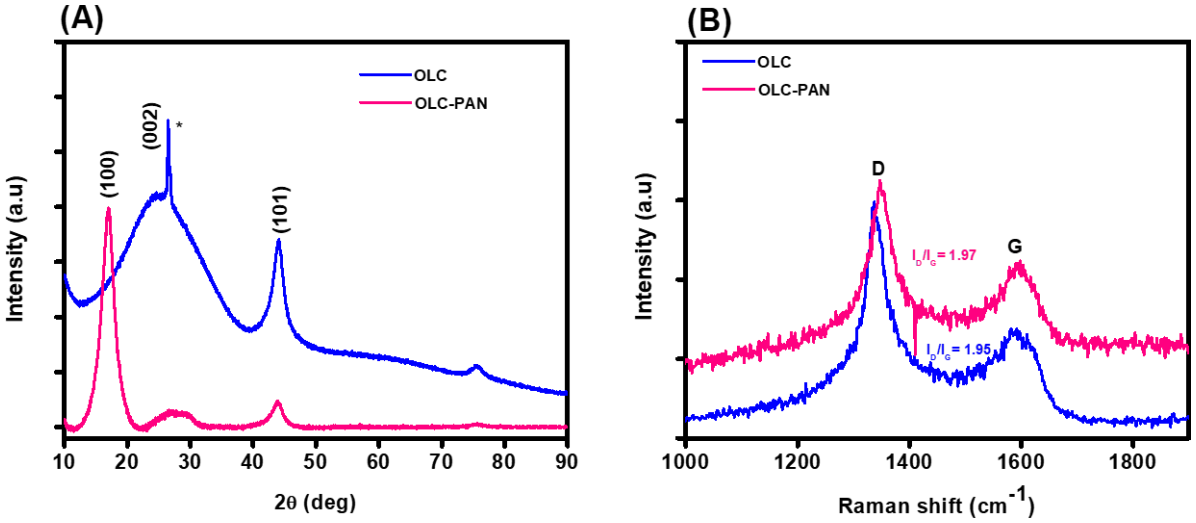


Figure 5.2: XRD of (A) OLC, OLC-PAN, and (B) raman spectra of OLC, OLC-PAN

5.1.4 Surface analysis

The BET surface area, pore volume and pore size were calculated as 279.05 m^2g^{-1}, 1.20 cm^3g^{-1}, and 17.11 nm, respectively for OLC, and as 117.69 m^2g^{-1}, 0.54 cm^3g^{-1}, and 22.89 nm respectively for OLC-PAN. The decrease in the surface area of OLC-PAN compared to the OLC should be expected considering the bulky nature of the OLC-PAN as evident from the SEM and TEM images.

5.2.5 XPS

Figure 5.3 shows the XPS wide scan spectrum of the OLC-PAN (Figure 5.3A) with the expected peaks for C1s, O1s, and N1s at binding energies of 286, 397, and 536

eV, respectively. The deconvoluted spectra are shown for C 1s (Figure 5.3B), O 1s (Figure 5.3C), and N 1s (Figure 5.3D). The C1s peak was deconvoluted to two binding energies at 283 eV (sp^3 (C−C), defects) and 284.6 eV (C−C). It is to be noted that the sp^3 (C−C) and sp2 (C−C) defect peaks are characteristics of the nanodiamonds [127,128] and the correct peak assignment has been a subject of controversy; most researchers believe that the peak position of sp^2 C is lower than that of the sp^3 C, few workers believe the opposite [129]. Interestingly, however, it has recently been demonstrated (via calculations) that the peak position of sp^2 C is greater than that of sp^3 C, which agrees with the experimental results of those few workers [129]. According to these workers [129], the ambiguous assignments could be related to charging effects and defects (such as pentagons, heptagons, and functional groups) present in diamonds. The values of the sp^3 (C−C) range between 283.15 and 283.21 eV, and even at 282.8 eV [101], which are in close agreement with our value of 283 eV. Importantly, considering that the OLC used in this study was obtained from detonation nanodiamonds (DNDs), we believe that the observed peak at 283 eV (sp^3 (C−C)) could have arisen from the unconverted DNDs present in the OLC. Similarly, the O1s peak was deconvoluted with two binding energies at 531.2 eV (C=O) and 529.8 eV (C−O) (Figure 5.3C). These peak assignments agree with previous reports [100,130]. In addition, the N 1s were deconvoluted to one peak at 398 eV, corresponding to a cyanide (C=N) bond arising from the PAN component of the composite structure. Note that the two binding energies of the O 1s peak, as well as that of the N 1s, are slightly shifted to lower values, but this can be attributed to electron transfer from the PAN to the oxygenated functional groups of the OLC

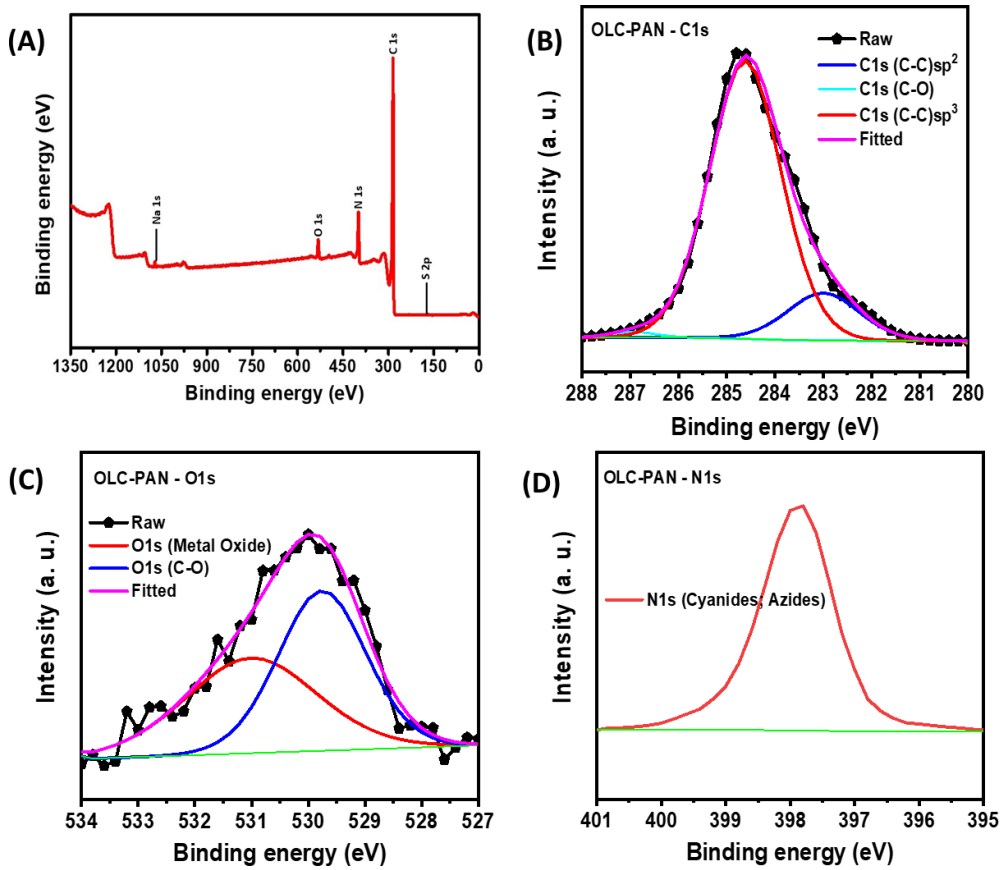


Figure 5.3: (A) wide scan spectra of OLC-PAN, and deconvoluted spectra of (B) C1s, (C) O1s and (D) N1s of OLC-PAN.

5.2 Cyclic voltammetry

5.3.1 mass transport and electrode kinetics

Figure 5.4 shows comparative cyclic voltammogram of bare-GCE (pink), GCE-OLC (red) and GCE-OLC-PAN (blue) at 50 mV/s in 0.1 mM of $Fe(CN)_6]^{4-}/[Fe(CN)_6]^{3-}$) and 3mM KCl. Some of the important parameters in CV are I_{pa} and I_{pc}, the ratio of I_{pa}/I_{pc},the value of ΔE_p (difference between E_{pa} and E_{pc}). The plot of log I_{pa} vs log Ʊ gives insight on the type of mass transport involved on the electrode-solution interface (see Figure 5.5 C, F, and I), a linear plot with a slope of 0.5 shows a diffusion-controlled mass transport whereas slope values above 0.5 shows an adsorption-controlled mass transport [131], all values were ~0.5 indicative of a diffusion controlled system. The ΔE_p were of the order GCE (357 mV) >GCE-OLC (125 mV)>GCE-OLC-PAN (121 mV),

GCE-OLC-PAN showed better electron transport than the former and the latter. This may be due to the presence of nitrogen from PAN, which increased the conductivity of the electrode. Thirdly, the ratio of i_{pa} and i_{pc} when is ~ 1 indicates a reversible reaction, as it were for all electrodes. Also, the scan rates indicate the stability of the electrode. The electrodes were highly stable, as no observable shifts were observed. All the CV parameters of the electrodes are summarized in Table 5.1.

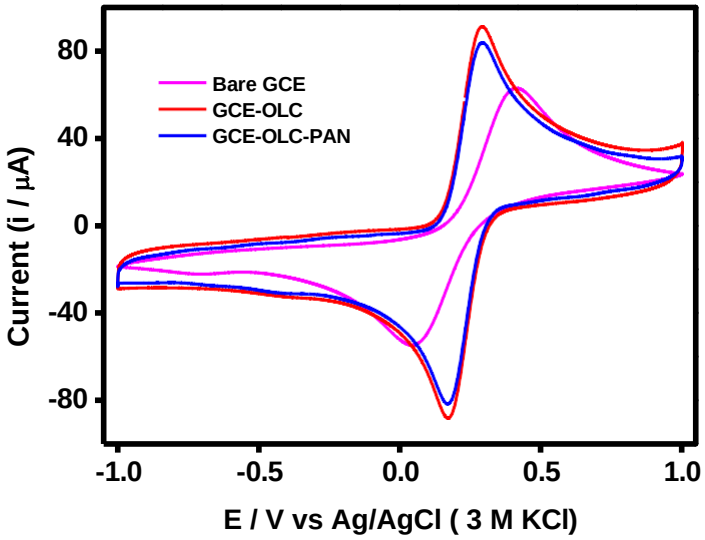


Figure 5.4: Comparative cyclic voltammogram of bare-GCE (pink), GCE-OLC (red) and GCE-OLC-PAN (blue) at 50 mV/s in 0.1 mM of $Fe(CN)_6]^{4-}/[Fe(CN)_6]^{3-}$) and 3mM KCl

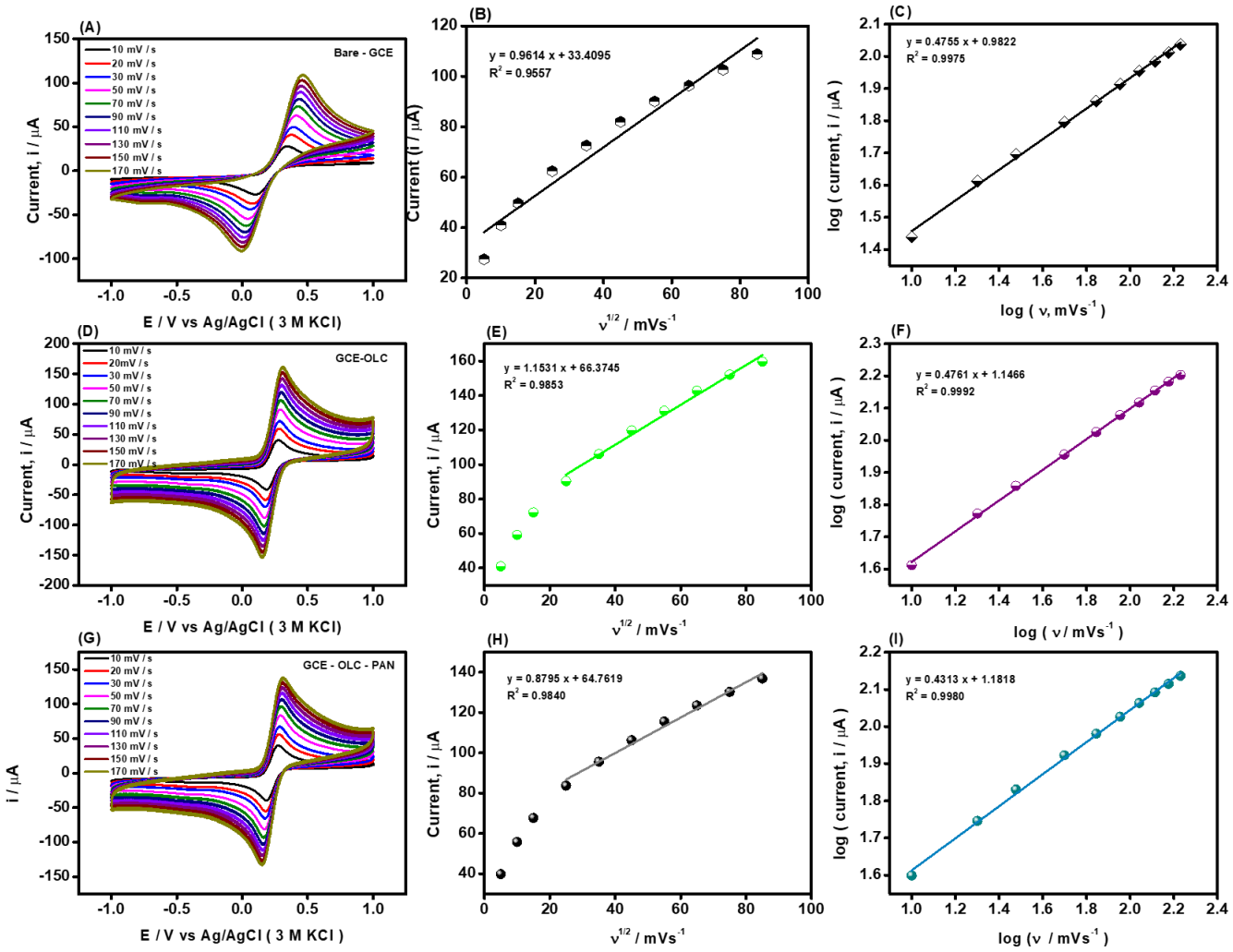


Figure 5.5: Scan rate studies of bare-GCE (A) and GCE-OLC (E) and GCE-OLC-PAN (G) with plots anodic current vs scan rates (B), (E), (H) and log anodic current vs log scan rate (C), (F) and (I), respectively

Table 5.1: Summary of CV parameters of bare-GCE, GCE-OLC and GCE-OLC-PAN

Electrode	E_{pa} (V)	E_{pc} (V)	ΔE (mV)	i_{pa} (µA)	i_{pc} (µA)	i_{pa}/i_{pc}
Bare GCE	0.410	0.0524	357	62.317	-53.710	1,13
OLC	0.300	0.170	125	90.696	-87.946	1.03
OLC-PAN	0.292	0,170	121	82.855	-80.632	1.02

5.4 Electroanalytical Performance of the Immunosensors Towards HPV-16 L1

The fabrication of the HPV-16 L1 immunosensors and antigen-antibody interaction mechanisms are described in the Experimental Section 2 but summarized as shown in Figure 5.6. The HPV antigen or antibody is immobilised onto the OLC- or OLC-PAN electrode via the conventional covalent bonding process by forming the strong amide bond using the sulfo-NHS ester [132–135]. In practice, route A describes the screening of HPV-16 infection (asymptomatic individuals), while route B is for testing the HPV-16 infection (in individual presents some symptoms). Cyclic voltammetric evolutions of the bare GCE, the electrochemical immunosensors (EI (1) and EI (2), Figure 5.6) and their corresponding antigen-antibody interaction stages (AA(I) and AAI (2), Figure 5.6) were conducted in the redox probe solution (i.e., PBS/AE, pH 7.4, containing 0.1 mM $[Fe(CN)_6]^{4-}/[Fe(CN)_6]^{3-}$) (see Figure 5.7). It was observed that the OLC-PAN-immunosensor exhibited the strongest current suppression (capacitive behaviour) upon interaction with the analytical HPV-16 antigen compared to the OLC-based counterpart. The difference between the two immunosensor electrodes may be related to the conductivity of the electrode platforms, where OLC shows higher electronic conductivity than the OLC-PAN counterpart. The CV parameters are summarized in Table 5.2. To note, for a reversible system, the I_{pa}/I_{pc}

ratio should be 1, and both electrode platforms showed a reversible nature. Also, the value of ΔE_p should be smaller for a fast electron transfer reaction; in both cases, the values were over upon modification with the biomolecules, and an increase in the ΔE_p values was observed, which was expected due to the nature of the immunosensor. For this sensor the higher the value of ΔE the better, it shows maximum complexation between Ab-Ag or vice versa, OLC-PAN showed higher values. Also, upon modification with the biomolecule, a decrease in current response was observed for both, OLC-PAN having the lowest, as mentioned earlier.

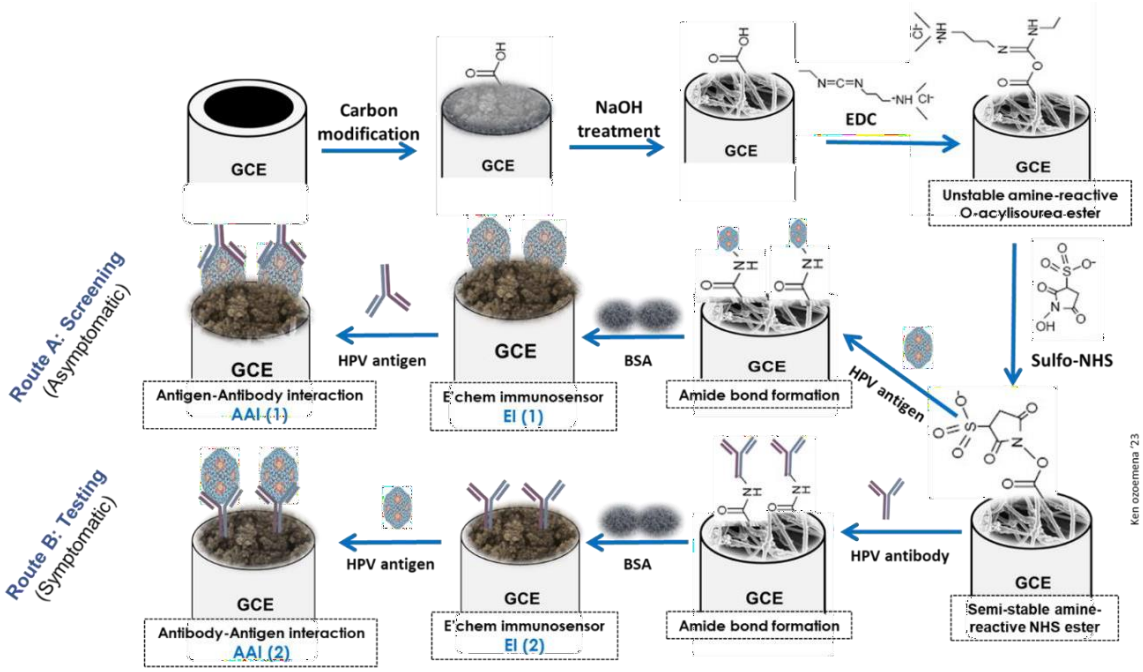


Figure 5.6: A typical fabrication pathway for HPV-16 L1 immunosensors. The reagents in each path are identified in the experimental section.

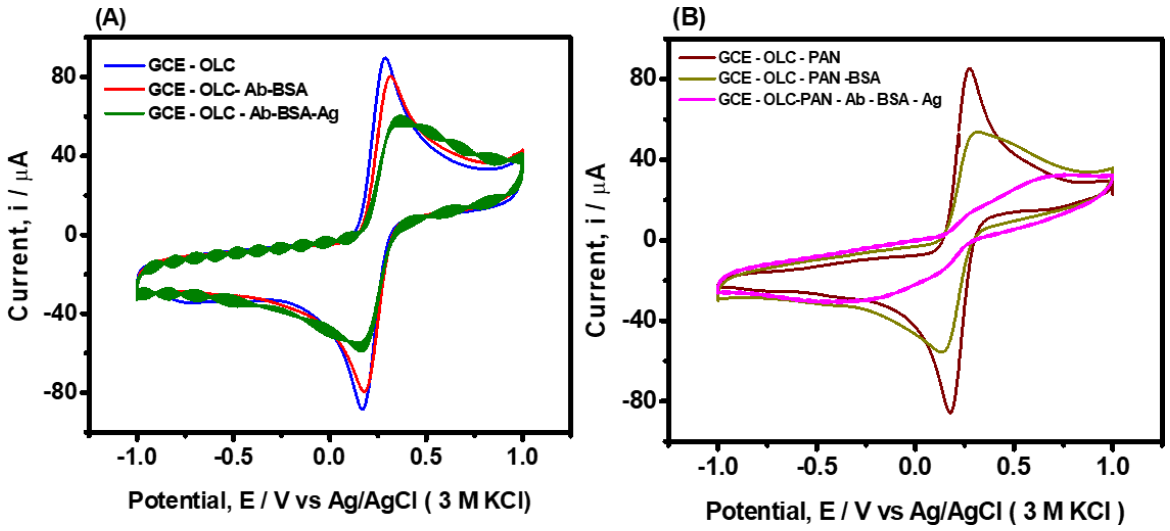


Figure 5.7: Comparative cyclic voltammograms of (A) GCE-OLC, GCE-OLC-Ab-BSA, and GCE-OLC-Ab-BSA-Ag, and (B) GCE-OLC-PAN, GCE-OLC-PAN-Ab-BSA, GCE-OLC-Ab-BSA-Ag at 50 nm

Table 5.2: Summary of CV parameters of GCE-OLC and GCE-OLC-PAN sensor platforms.

Electrode name	ΔE (mV)	I_{pa} (µA)	I_{pc}(µA)	I_{pa}/I_{pc} (µA)
GCE-OLC	177,89	89,99	-88,47	1,01
GCE-OLC-Ab-BSA	185,73	80,39	-79,63	1,00
GCE-OLC-Ab-BSA-Ag	195,21	60,68	-59,09	1,03
GCE-OLC-PAN	93,33	84,84	-85,13	1,00
GCE-OLC-PAN-Ab-BSA	174,6	53,52	-55,65	0,96

GCE-OLC-PAN-Ab-BSA-Ag	436,5	40,01	-37,27	1,07

The developed electrochemical immunosensors were employed to detect HPV-16 L1 antigen at different concentrations (Figure 5.8). The concentration studies were conducted by exposing/immersing the immunosensor in different concentrations of the HPV-16 L1 antigen (from 1.95×10^{-12} to 5.0×10^{-2} mg/mL) for 5 min to allow for the complexation to occur, after which square wave voltammetry (SWV) was used to monitor the reaction in the presence of the redox probe. The continuous suppression of the redox peaks of the redox probe upon increasing concentration of the HPV-16 L1 antigen is indicative of the excellent complexation between Ab and Ag. The OLC-based immunosensor (Figure 5.8A) showed a broader peak response than its OLC-PAN counterpart (Figure 5.8C). Aside from this disadvantage of the OLC- based electrode platform, the OLC-PAN-based immunosensor also showed better linearity than the OLC-based immunosensor (i.e., $R^2 = 0.9971$ cf 0.9823). Thus, the OLC-PAN electrode was used to immobilise the HPV-16 L1 antibody for the detection of the HPV-16 L1 antigen. The current response for each concentration was determined by taking the difference from the blank, i.e., (Δi/μA). For both immunosensors, two linear concentration ranges (Figure 5.8 B, C, for OLC and OLC- PAN-based immunosensors, respectively) were observed at low (i.e., $1.95 \times 10^{-12} - 6.25 \times 10^{-6}$ mg/mL) and high ($6.25 \times 10^{-6} - 5.0 \times 10^{-2}$ mg/mL) concentration ranges. Considering that the OLC-PAN-based electrode platform gives a sharper current response, the results are summarized as follows:

OLC-based immunosensors for HPV-16 antigen detection:

$\Delta i/\mu A = 5.406 \pm 0.2479 \log([\text{HPV-16 L1, fg/mL}]) + 1.175 \pm 1.0366$ ($R^2 = 0.9917$)

(5.1)

OLC-PAN-based immunosensors for HPV-16 antigen detection:

$\Delta i/\mu A = 5.232 \pm 0.1740 \log([\text{HPV-16 L1, fg/mL}]) + 16.3757 \pm 0.7278$ ($R^2 = 0.9956$)

(5.2)

OLC-PAN-based immunosensors for HPV-16 antibody detection:

$\Delta i/\mu A = 1.2518 \pm 0.0.0533 \log([\text{HPV-16 L1, fg/mL}]) + 6.3744 \pm 0.3519$ ($R^2 = 0.9910$)

(5.3)

As summarized in Table 5.3, the immunosensors exhibited wide linear concentration ranges (1.95 fg/mL to 6.0 ng/mL, i.e., 34.82 aM to 0.11 nM), excellent sensitivity at the low concentration range for the detection of antigen (i.e., 5.406 ± 0.2479 µA/log([HPV-16 L1, fg/mL]) for the OLC-based immunosensor, and 5.232 ± 0.1740 µA/log([HPV-16 L1, fg/ mL]) for the OLC-PAN-based immunosensor). For the detection of the antibody at OLC-PAN-based immunosensor, the sensitivity is lower than observed for the antigen (i.e., 1.2518 ± 0.0533 µA/log([HPV-16 L1, fg/mL]). The immunosensors showed ultra-low detection limits (i.e., LoD = 3 s/*m*, and LoQ = 10 s/*m*, where s is the standard deviation of the intercept, while *m* is the slope/sensitivity of the calibration plot. The values were calculated as the average of six electrodes and are summarized in Table 5.3, with LoD as ca. 0.61 fg/mL (10.89 aM) and 1.83 fg/mL (32.7 aM) for OLC-PAN and OLC-based immunosensors, respectively. Using the OLC-PAN-based immunosensor, the HPV-16 L1 antibody was detected at 2.54 fg/mL (45.36 aM). The extraordinary low detection limits shown in this work represent the first of its kind for the detection of HPV-16 L1 using either immunosensor or nucleic acid-based sensors (Table 5.3). For possible clinical application, we can compare with the conventional

liquid-based pap test (LBPT) (which is still the most easily accessible technique in rural areas of resource limited countries, or LMICs) and the more advanced PCR based techniques. In LBPT, the specimen sample is rinsed into a sample container, and the liquid is placed onto a microscope slide. Then, the sample is examined under a microscope to check whether the cells are normal. The detection limit of LBPT is about 2000 copies/mL (i.e., 4.04 fg/mL) [136]. There is a commercial APTIMA HPV assay that detects the mRNA of high-risk HPV, including HPV 16 L1, was reported to be able to detect 106 mRNA copies/reaction (i.e., ca. 0.21 fg). The real-time PCR (RT-PCR) is the most essential critical molecular technique for testing high-risk HPV types in clinical laboratories, mainly in high-income settings and advanced countries. In addition, recombinase polymerase amplification (RPA) represents an isothermal alternative to the PCR. Previously, Hesselink et al. [137] showed that the HPV-risk assay y (i.e., a type of real-time PCR assay) used for testing clinical samples gave LoD of 460 copies/reaction (ca. 0.93 fg) for the HPV-16 L1 genotype). In addition, in 2023, Wongsamart et al. [138] reported an advanced form of RPA known as the multiplex recombinase polymerase amplification (mRPA), which gave an LoD of 1000 copies/ reaction (i.e., 2.01 fg) for the HPV-16 L1 genotype. The LoD values of our proposed electrochemical immunosensor are lower than the conventional LBPT, and comparable or even lower than the advanced PCR and mRPA techniques. It should be noted, however, that we could not subject our immunosensors to testing real clinical samples at this time due to the inherent difficulty of obtaining ethical clearance for human samples, but efforts are being made to overcome this in the future.

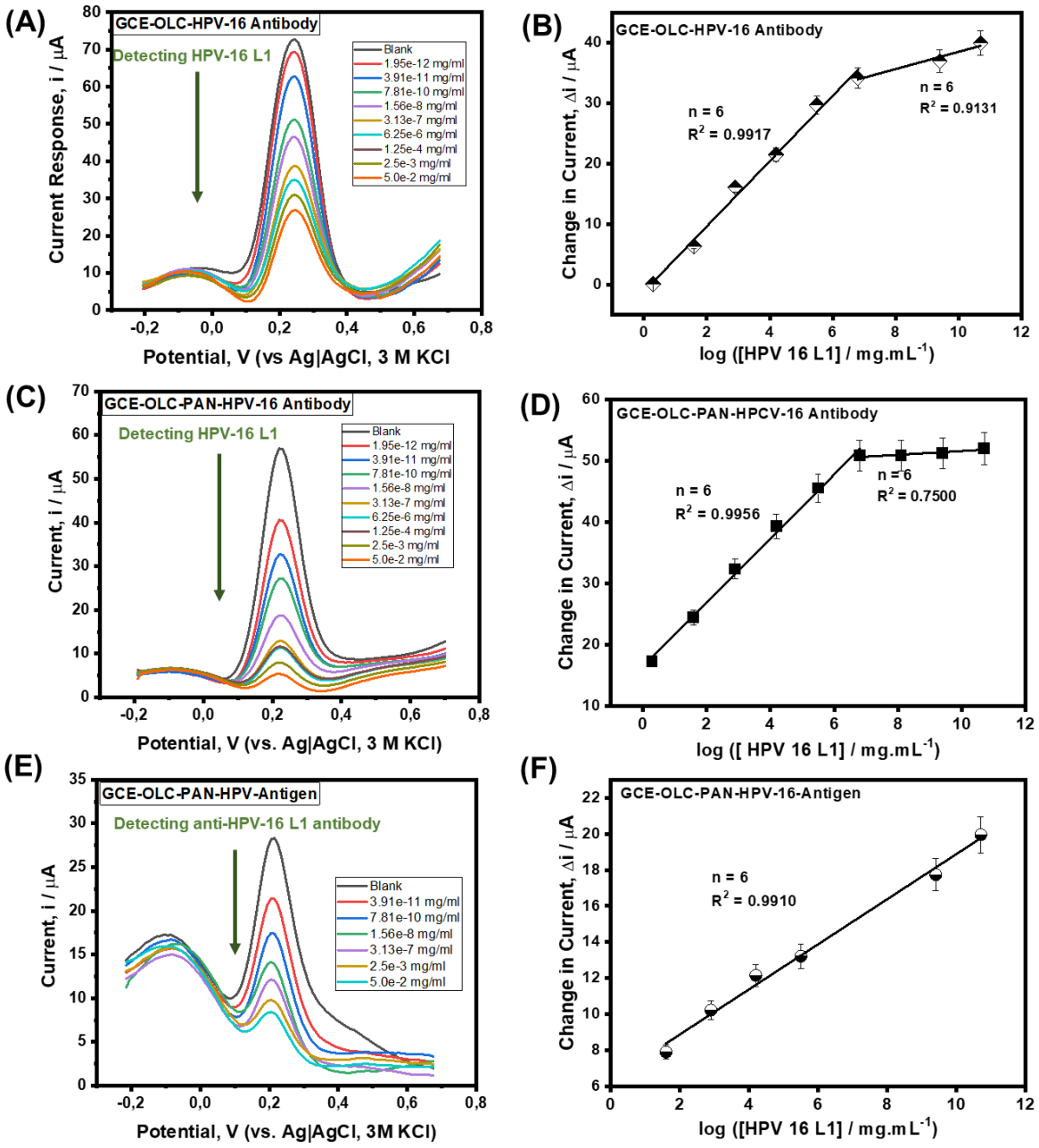


Figure 5.8: (**A**) Concentration studies of HPV-16 L1 (Ag) and (**B**) linear plot of change in current vs log [HPV-16 L1] **Figure 5.7**: (**A**) shows concentration studies of Anti-HPV 16 L1, (**B**) shows linear plot of change in current vs log [Anti-HPV 16 L1].

Table 5.3: Reports on the values obtained in this work in comparison to literature

Platform	Target	Technique	LCR	LOD	LOQ	Ref
GCE-OLC	HPV-16 L1 (antigen)	SWV	1.95 fg/mL-6.25 ng/mL (34.2 aM-0.112 nM)	1.83 fg/mL (32 aM)	6.11 fg/mL (0.11 fM)	This work
GCE-OLC-PAN	HPV-16 L1 (antigen)	SWV	1.95 fg/mL-6.25 ng/mL (34.2 aM-0.112 nM)	0.61 fg/mL (10.89 aM)	2.03 fg/mL (36.3 aM)	This work
GCE-OLC-PAN	HPV-16 L1 (antibody)	SWV	39.1 fg/mL-60µg/mL (0.70 fM-1.07 µM)	2.54 fg/mL (45.36 aM)	8.46 fg/mL (0.15 fM)	This work
prGO-MoS2	HPV-16 L1 (antigen)	DPV	1.75 pM			[28]
GC-polymer	HPV-16 L1 (antigen)	SWV	50 nM			[30]
Ag@AuNPS-GO/SPA	HPV-16 L1 (antigen)	DPV	2.0 pg/mL			[139]
Pt/PaN/MWCNTs	HPV-16 L1 (antigen)	CV/SWV	490 pM			[140]
Melanine-AuNPS	HPV-16 L1 (antigen)	LDI MS	58.8 pg/mL			[141]
AuNPs-Aptamer	HPV-16 L1 (antigen)	Uv-vis/corori metry	9.6 ng/mL			[142]

[a] KEY: Molar mass of HPV-16 L1 (56 kDa) was used to convert the gravimetric concentrations to their corresponding molar concentrations. LCR (linear concentration range); LoD (limit of detection); LoQ (limit of quantification); PaN (polyaniline); AuNPs (gold nanoparticles); SPA (staphylococcal protein A); LDI MS (laser desorption ionization mass spectrometry); SWV (square wave voltammetry); and DPV (differential pulse voltammetry).

5.5 Specificity studies and sensor re-usability

To test for specificity, we adopted the use of an anti-ovalbumin antibody (anti-OVA) and native ovalbumin protein (OVA) as reported elsewhere [30]. The anti-OVA (Ab)

was immobilized as prescribed during the experimental session and the anti-OVA immunosensor. The constructed immunosensor (GCE-OLC-PAN-OVAAb-BSA) was used to compare the extent to which the OVA-antibody can interact with the corresponding OVA-antigen and HPV-16 L1 antigen of similar concentration (7.8×10^{-15} fg/mL). As shown in Figure 5.9A, the OVA-antibody exhibited very strong interaction with the OVA-antigen but with weak or no interaction with the HPV-16 L1 antigen. The rejection of the OVA-ab by the HPV-16 L1 antigen confirms the specificity of the HPV-16 L1 antigen with its corresponding antibody. To test for reusability/reproducibility of the proposed immunosensor, we adopted the well-established procedure of glycine chemistry [143]. In a nutshell, the ability to reuse OLC-PAN-based immunosensor after chemically stripping off its active HPV-16 L1 antibody was interrogated using a constant concentration of the HPV-16 L1 antigen (7.8×10^{-15} fg/mL). On the first day, the immunosensor was used to detect the antigen, thereafter the bound antigen was stripped off by dipping the immunosensor into a buffer solution of glycine HCl (pH 2.8) for 5 min and then reused to detect the HPV-16 L1 antigen. The detection−stripping cycle was carried out six different times with each step used to detect the antigen five times. After the repetitive regeneration-detection steps, the immunosensor electrode was stored in the refrigerator at 4 °C, and the process was repeated on the 7th day. As shown in Figure 5.9B, the immunosensor was found to be reusable even on the 7th day, albeit with minor loss in the current response compared to the 6th regeneration-detection step on the first day

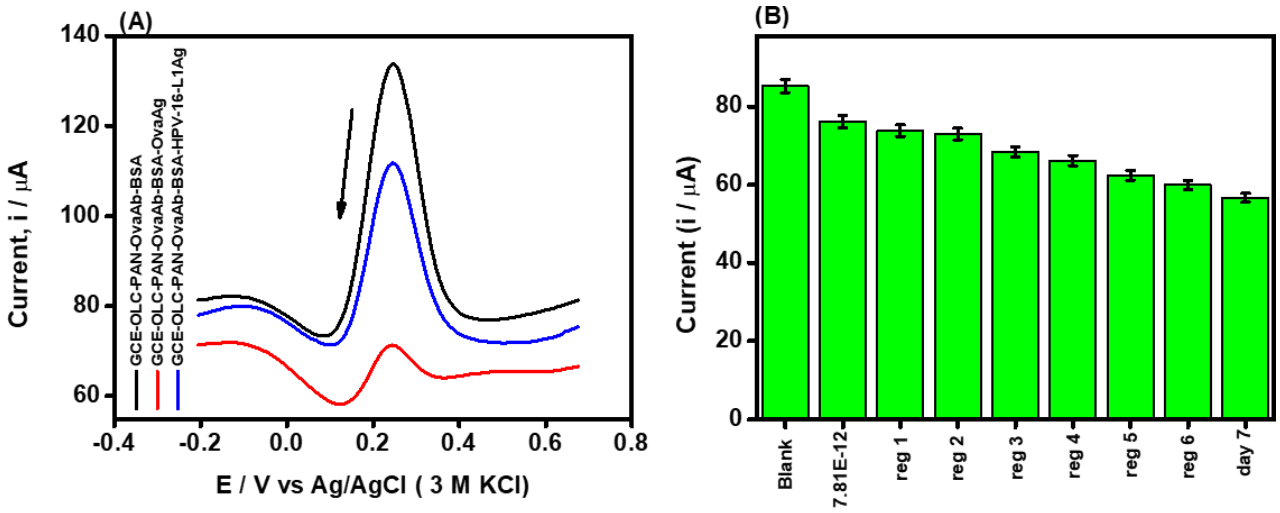


Figure 5.9: (A) Square wave voltametric responses of GCE-OLC-PAN-OvaAb-BSA towards Ova-antigen ($7.8x10^{-15}$ fg/ml) and HPV-16 L1 antigen ($7.8x10^{-15}$ fg/ml), **(B)** Bar chart describing the responses of HPV-16-L1 antibody towards HPV-16 L1 ($7.8x10^{-15}$ fg/ml) after detection-stripping cycles.*reg means the regeneration of the surface.

5.6 Proof of concept

The possible practical application of the HPV immunosensor was tested using a screen-printed carbon electrode (SPCE) modified with the HPV-16 L1 antibody (Figure 5.0A, B). Although this was preliminary work, it is evident from Figure 6C that the immunosensor can detect very low ($6.98x10^{-13}$ mg/ml) and high ($1.15x10^{-2}$ mg/ml) concentrations of the antigenic HPV-16 L1. This result promises, upon thorough optimization, to move from lab-based techniques to point-of-care diagnosis of HPV infections.

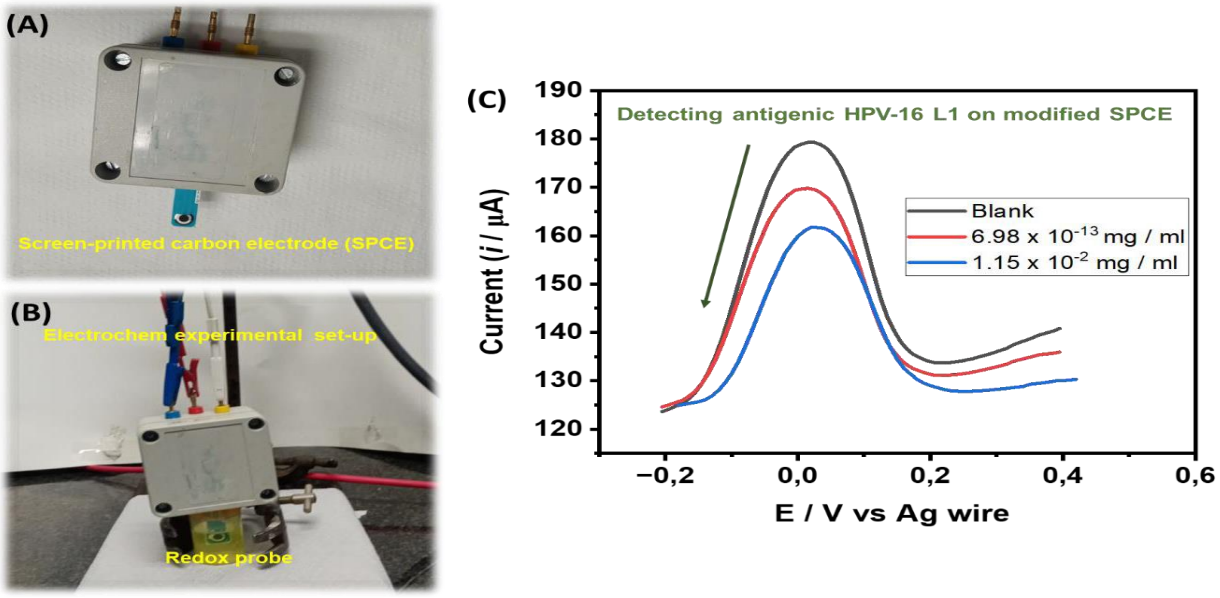


Figure 5.10: (A, B) Set-up of a screen-printed carbon electrode (SPCE) modified with HPV-16 L1 antibody immunosensor, (B) typical square wave voltammetric responses towards antigenic HPV-16 L1.

5.7 Conclusion

OLC and OLC-PAN were successfully utilised as electrode platforms for the detection of HPV-16 L1 antigen and antibody. Both platforms exhibited a wide linear concentration range (1.95 fg/mL to 6.25 ng/mL) and ultra-low detection of 1.83 fg/mL (32.7 aM) and 0.61 fg/mL (10.9 aM) for OLC- PAN and OLC-based immunosensors, respectively. The high specificity of detection was proven by experimenting with an anti-ovalbumin antibody (anti-OVA) and native ovalbumin protein (OVA). An immobilised antigenic HPV-16 L1 peptide showed insignificant interaction with anti-OVA in contrast with the excellent interaction with the anti-HPV-16 L1 antibody. The sensor's reusability was also tested, and a couple of runs were done, which showed that even after using the sensor several times, the sensor was still active although there was a slight decrease in the current response. The immunosensor still showed some activity after the 7th day of storage upon surface regeneration. The application

of the immunosensor as a potential PoC diagnostic device was investigated with the SPEC, which showed the ability to detect ultra-low (ca. 0.7 fg/mL ≈ 12.5 aM) and high (ca. 12 µg/mL ≈ 0.21 µM) concentrations. This work represents the lowest detection limit ever reported for HPV-16 L1 using electrochemical and non-electrochemical methods The results open the door of opportunity for studying other electrode platforms and realizing PoC diagnostic devices for screening and testing of HPV biomarkers for cervical cancer.

Chapter Six

Conclusion and recommendations

6.1 Conclusion

Co-MOF using different ligands with different synthesized lengths were successfully synthesized, as confirmed by the XRD, SEM and Raman. These Co-MOFs were successfully used as sacrificial templates for synthesising Co-NPs@C_{TMA} and Co-NPs@C_{BPDC}. These were characterised using XRD, raman, BET, XPS etc. It was found that the Co-NPs@C_{BPDC} contained a higher surface area than the Co-NPs@C_{TMA} also using XPS, we were able to show that the former had more oxygen vacancies than the latter. The presence of high oxygen vacancies for Co-NPs@C_{BPDC}. The high oxygen vacancies assisted in the detection of MN as the Co-NPs@C_{BPDC} showed better electrocatalytic abilities. The cyclic voltammograms of both electocatalysts showed a reversible CV due to Cobalt oxidation and reduction, which was used as an indirect method of dectection for MN. Compared to what has been reported in literature, the sensors showed better responses with lower LOD. MN was also detectable in the presence of interfering species, meaning the presence of other chemical species will not deter the detection of MN. Also, in serum, a concentration corresponding to that of MN in PBS was detectable for both Co-NPs@C_{TMA} and Co-NPs@C_{BPDC}.

Two materials, i.e. OLC and OLC-PAN were successfully synthesized and were later used for the fabrication of an HPV-16 L1 immunosensor. Various physicochemical techniques were used for the characterization of the material such as XRD, SEM, and XPS. A immunosensor was fabricated using the two materials and were both used for

The detection of the HPV-16 L1 antigen and antibody. The OLC-PAN was found to be the best-performing sensor as it showed maximum suppression than the OLC. Both sensors exhibited ultralow detection limits, with OLC-PAN showing lower LOD = 0.61 fg/mL and LOQ = 2.03 fg/mL than the OLC = 1.83 fg/mL and LOQ = 6.11 fg/mL. For the latter reason, an immunosensor was fabricated using OLC- PAN to detect the HPV-16 L1 antibody, and the sensor still depicted a lower LOD = 2.54 fg/mL. The selectivity studies were done using Ova and anti-Ova, and it was still demonstrated that the immunosensor had the ability to detect HPV 16 only and no other interfering biomolecules, making the sensor more selective towards the analyte of interest. The sensor's ability to be used more than once was also tested, and after several times of surface regeneration was done, the sensor was still able to detect the analyte, though a small fraction of the activity was lost. Also, after long-term storage of the sensor, it was still able to detect the analyte. Using SPE, it was demonstrated that it is a highly promising PoC method that can be used.

6.2 Recommendations

The method that was used was microwave-assisted synthesis in this work, the author recommends that:

- The synthesis of the material be done using both MAS and conventional heating method to see what effect of using different heating methods would induce on the properties of the material
- Vary the ligand-to-metal salt ratio and vice versa
- Vary the heating temperatures during synthesis
- Use different polymers to see what effect they will have. In this work ethylene glycol was used because of its good microwave properties
- Varying calcining temperatures

- Explore other applications, as this material holds great potential.

A lot can be done for the gas sensing, such as

- More studies are needed for stability

6.3 The work that formed part of this work is the HPV-16 L1 detection and some recommendations for the work. A lot was done, but serum work was not done, so the writer recommends:

- The detection be done in serum using both GCE and SPE
- Use different carbon-based materials and determine the effect of surface area for this particular work, as surface area plays an important role
- Dope the carbon material with different heteroatoms, to increase the conductivity of the material.
- Obtain clinical samples from hospitals that were confirmed to be HPV infected for real-life application, as it would be highly good if this immunosensor would be used to deal with real-life issues, moving from a “laboratory setting to a real-life situation”. It would make it easy to for people test for HPV frequently, as this would be less of an invasive technique than Pap smear and also to would assist on the early detection of cervical cancer.

References

[1] H.J. Zar, Global paediatric pulmonology: Out of Africa, Paediatr. Respir. Rev. 7 (2006) 226–228. doi:10.1016/j.prrv.2006.04.195.

[2] H. Thakur, N. Kaur, D. Sareen, N. Prabhakar, Electrochemical determination of M. tuberculosis antigen based on Poly(3,4-ethylenedioxythiophene) and functionalized carbon nanotubes hybrid platform, Talanta. 171 (2017) 115–123. doi:10.1016/j.talanta.2017.04.063.

[3] World Health Organization, Use of high burden country lists for TB by WHO in the post-2015 era : Summary, Who. 5 (2020) 2015. https://www.who.int/tb/publications/global_report/high_tb_burdencountrylists2016-2020summary.pdf.

[4] M.H. Mat Zaid, J. Abdullah, N.A. Yusof, Y. Sulaiman, H. Wasoh, M.F. Md Noh, R. Issa, PNA biosensor based on reduced graphene oxide/water soluble quantum dots for the detection of Mycobacterium tuberculosis, Sensors Actuators, B Chem. 241 (2017) 1024–1034. doi:10.1016/j.snb.2016.10.045.

[5] S.A. Alshoabi, K.M. Almas, S.A. Aldofri, A.M. Hamid, F.H. Alhazmi, W.M. Alsharif, O.M. Abdulaal, A.A. Qurashi, K.M. Aloufi, K.D. Alsultan, A.M. Omer, T.S. Daqqaq, The Diagnostic Deceiver: Radiological Pictorial Review of Tuberculosis, Diagnostics. 12 (2022) 1–28. doi:10.3390/diagnostics12020306.

[6] W. Gong, X. Wu, Differential Diagnosis of Latent Tuberculosis Infection and Active Tuberculosis: A Key to a Successful Tuberculosis Control Strategy, Front. Microbiol. 12 (2021) 1–23. doi:10.3389/fmicb.2021.745592.

[7] M. Syhre, S.T. Chambers, The scent of Mycobacterium tuberculosis, Tuberculosis. 88 (2008) 317–323. doi:10.1016/j.tube.2008.01.002.

[8] M. Syhre, L. Manning, S. Phuanukoonnon, P. Harino, S.T. Chambers, The scent of Mycobacterium tuberculosis - Part II breath, Tuberculosis. 89 (2009) 263–266. doi:10.1016/j.tube.2009.04.003.

[9] K.I. Ozoemena, S. Carrara, Biomedical electrochemical sensors for resource-limited countries, Curr. Opin. Electrochem. 3 (2017) 51–56. doi:10.1016/j.coelec.2017.06.002.

[10] D. Bhattacharyya, Y.R. Smith, M. Misra, S.K. Mohanty, Electrochemical detection of methyl nicotinate biomarker using functionalized anodized titania nanotube arrays, Mater. Res. Express. 2 (2015). doi:10.1088/2053-1591/2/2/025002.

[11] Y.R. Smith, D. Bhattacharyya, S.K. Mohanty, M. Misra, Anodic Functionalization of Titania Nanotube Arrays for the Electrochemical Detection of Tuberculosis Biomarker Vapors, J. Electrochem. Soc. 163 (2016) B83–B89. doi:10.1149/2.0741603jes.

[12] D. Bhattacharyya, Y.R. Smith, S.K. Mohanty, M. Misra, Titania

Nanotube Array Sensor for Electrochemical Detection of Four Predominate Tuberculosis Volatile Biomarkers, J. Electrochem. Soc. 163 (2016) B206–B214. doi:10.1149/2.0221606jes.

[13] J.P. Metters, D.K. Kampouris, C.E. Banks, Fingerprinting breath: Electrochemical monitoring of markers indicative of bacteria Mycobacterium tuberculosis infection, J. Braz. Chem. Soc. 25 (2014) 1667–1672. doi:10.5935/0103-5053.20140159.

[14] P. KumarBairagi, A. Goyal, NishithVerma, Cobalt-Dispersed Reduced Graphene Oxide Nanocomposite for the Selective lectrochemical Detection of Methyl Nicotinate, (2019) 18. doi:10.3390/proceedings2019015018.

[15] T.W. Chen, R. Arumugam, S.M. Chen, M. Altaf, S. Manohardas, M. Saeed Ali Abuhasil, M. Ajmal Ali, Ultrasonic preparation and nanosheets supported binary metal oxide nanocomposite for the effective application towards the electrochemical sensor, Ultrason. Sonochem. 64 (2020) 105007. doi:10.1016/j.ultsonch.2020.105007.

[16] C.N. Willis, S.R. Larson, A. Andama, D. Jaganath, M. Misra, A. Cattamanchi, S.K. Mohanty, Engineered Electroactive Solutions for Electrochemical Detection of Tuberculosis-Associated Volatile Organic Biomarkers, IEEE Sens. J. 22 (2022) 2984–2992. doi:10.1109/JSEN.2021.3126732.

[17] T. Ramesh, K.L. Foo, R. Haarindraprasad, A.J. Sam, M.

Solayappan, Gold-Hybridized Zinc Oxide Nanorods as Real-Time Low-Cost NanoBiosensors for Detection of virulent DNA signature of HPV-16 in Cervical Carcinoma, Sci. Rep. 9 (2019) 1–17. doi:10.1038/s41598-019-53476-9.

[18] D.S. Campos-Ferreira, E.V.M. Souza, G.A. Nascimento, D.M.L. Zanforlin, M.S. Arruda, M.F.S. Beltrão, A.L. Melo, D. Bruneska, J.L. Lima-Filho, Electrochemical DNA biosensor for the detection of human papillomavirus E6 gene inserted in recombinant plasmid, Arab. J. Chem. 9 (2016) 443–450. doi:10.1016/j.arabjc.2014.05.023.

[19] K.Y.P.S. Avelino, L.S. Oliveira, N. Lucena-Silva, C.P. de Melo, C.A.S. Andrade, M.D.L. Oliveira, Metal-polymer hybrid nanomaterial for impedimetric detection of human papillomavirus in cervical specimens, J. Pharm. Biomed. Anal. 185 (2020). doi:10.1016/j.jpba.2020.113249.

[20] H. Sung, J. Ferlay, R.L. Siegel, M. Laversanne, I. Soerjomataram, A. Jemal, F. Bray, Global Cancer Statistics 2020: GLOBOCAN Estimates of Incidence and Mortality Worldwide for 36 Cancers in 185 Countries, CA. Cancer J. Clin. 71 (2021) 209–249. doi:10.3322/caac.21660.

[21] D. Singh, J. Vignat, V. Lorenzoni, M. Eslahi, O. Ginsburg, B. Lauby-Secretan, M. Arbyn, P. Basu, F. Bray, S. Vaccarella, Global estimates of incidence and mortality of cervical cancer in 2020: a baseline analysis of the WHO Global Cervical Cancer Elimination

Initiative, Lancet Glob. Heal. 11 (2023) e197–e206. doi:10.1016/S2214-109X(22)00501-0.

[22] M. Arbyn, E. Weiderpass, L. Bruni, S. de Sanjosé, M. Saraiya, J. Ferlay, F. Bray, Estimates of incidence and mortality of cervical cancer in 2018: a worldwide analysis, Lancet Glob. Heal. 8 (2020) e191–e203. doi:10.1016/S2214-109X(19)30482-6.

[23] A.L.P. Abreu, R.P. Souza, F. Gimenes, M.E.L. Consolaro, A review of methods for detect human Papillomavirus infection, Virol. J. 9 (2012) 1–9. doi:10.1186/1743-422X-9-262.

[24] A.G. Waxman, M.M. Zsemlye, Preventing Cervical Cancer: The Pap Test and the HPV Vaccine, Med. Clin. North Am. 92 (2008) 1059–1082. doi:10.1016/j.mcna.2008.04.012.

[25] M.L. Wilson, K.A. Fleming, M.A. Kuti, L.M. Looi, N. Lago, K. Ru, Access to pathology and laboratory medicine services: a crucial gap, Lancet. 391 (2018) 1927–1938. doi:10.1016/S0140-6736(18)30458-6.

[26] S. Pareek, U. Jain, M. Bharadwaj, N. Chauhan, A label free nanosensing platform for the detection of cervical cancer through analysis of ultratrace DNA hybridization, Sens. Bio-Sensing Res. 33 (2021) 100444. doi:10.1016/j.sbsr.2021.100444.

[27] J.R. Espinosa, M. Galván, A.S. Quiñones, J.L. Ayala, V. Ávila, S.M. Durón, Electrochemical resistive dna biosensor for the detection of hpv type 16, Molecules. 26 (2021). doi:10.3390/molecules26113436.

[28] F. Chekin, K. Bagga, P. Subramanian, R. Jijie, S.K. Singh, S. Kurungot, R. Boukherroub, S. Szunerits, Nucleic aptamer modified porous reduced graphene oxide/MoS2 based electrodes for viral detection: Application to human papillomavirus (HPV), Sensors Actuators, B Chem. 262 (2018) 991–1000. doi:10.1016/j.snb.2018.02.065.

[29] P. Teengam, W. Siangproh, A. Tuantranont, C.S. Henry, T. Vilaivan, O. Chailapakul, Electrochemical paper-based peptide nucleic acid biosensor for detecting human papillomavirus, Anal. Chim. Acta. 952 (2017) 32–40. doi:10.1016/j.aca.2016.11.071.

[30] B. Piro, A. Kapella, V.H. Le, G. Anquetin, Q.D. Zhang, S. Reisberg, V. Noel, L.D. Tran, H.T. Duc, M.C. Pham, Towards the detection of human papillomavirus infection by a reagentless electrochemical peptide biosensor, Electrochim. Acta. 56 (2011) 10688–10693. doi:10.1016/j.electacta.2011.04.094.

[31] D.P. Valencia, L.M.F. Dantas, A. Lara, J. García, Z. Rivera, J. Rosas, M. Bertotti, Development of a bio-electrochemical immunosensor based on the immobilization of SPINNTKPHEAR peptide derived from HPV-L1 protein on a gold electrode surface, J. Electroanal. Chem. 770 (2016) 50–55. doi:10.1016/j.jelechem.2016.03.040.

[32] A.N. Kozitsina, T.S. Svalova, N.N. Malysheva, A. V. Okhokhonin, M.B. Vidrevich, K.Z. Brainina, Sensors based on bio and biomimetic

receptors in medical diagnostic, environment, and food analysis, Biosensors. 8 (2018) 1–34. doi:10.3390/bios8020035.

[33] A. Hulanicki, S. Glab, F. Ingman, Chemical sensors definitions and classification, Pure Appl. Chem. 63 (1991) 1247–1250. doi:10.1351/pac199163091247.

[34] S.C. Kishore, K. Samikannu, R. Atchudan, S. Perumal, T.N.J. Immanuel Edison, M. Alagan, A.K. Sundramoorthy, Y.R. Lee, Smartphone-Operated Wireless Chemical Sensors: A Review, Chemosensors. 10 (2022) 1–22. doi:10.3390/chemosensors10020055.

[35] J. Baranwal, B. Barse, G. Gatto, G. Broncova, A. Kumar, Electrochemical Sensors and Their Applications: A Review, Chemosensors. 10 (2022). doi:10.3390/chemosensors10090363.

[36] N.R. Stradiotto, H. Yamanaka, M.V.B. Zanoni, Electrochemical sensors: A powerful tool in analytical chemistry, J. Braz. Chem. Soc. 14 (2003) 159–173. doi:10.1590/S0103-50532003000200003.

[37] J.N. Tiwari, V. Vij, K.C. Kemp, K.S. Kim, Engineered carbon-nanomaterial-based electrochemical sensors for biomolecules, ACS Nano. 10 (2016) 46–80. doi:10.1021/acsnano.5b05690.

[38] D. Grieshaber, R. MacKenzie, J. Vörös, E. Reimhult, Electrochemical biosensors - Sensor principles and architectures, Sensors. 8 (2008) 1400–1458. doi:10.3390/s8031400.

[39] C. Bucolo, G.M. Leggio, F. Drago, S. Salomone, Dopamine

outside the brain: The eye, cardiovascular system and endocrine pancreas, Pharmacol. Ther. 203 (2019) 107392. doi:10.1016/j.pharmthera.2019.07.003.

[40] V. Pérez-Fernández, D.G. Harman, J.W. Morley, M.A. Cameron, Optimized Method to Quantify Dopamine Turnover in the Mammalian Retina, Anal. Chem. 89 (2017) 12276–12283. doi:10.1021/acs.analchem.7b03216.

[41] H. Teymourian, M. Parrilla, J.R. Sempionatto, N.F. Montiel, A. Barfidokht, R. Van Echelpoel, K. De Wael, J. Wang, Wearable Electrochemical Sensors for the Monitoring and Screening of Drugs, ACS Sensors. 5 (2020) 2679–2700. doi:10.1021/acssensors.0c01318.

[42] T.J. Ehirim, O.C. Ozoemena, P. V. Mwonga, A.B. Haruna, T.P. Mofokeng, K. De Wael, K.I. Ozoemena, Onion-like Carbons Provide a Favorable Electrocatalytic Platform for the Sensitive Detection of Tramadol Drug, ACS Omega. 7 (2022) 47892–47905. doi:10.1021/acsomega.2c05722.

[43] N. Bhalla, P. Jolly, N. Formisano, P. Estrela, Introduction to biosensors, Essays Biochem. 60 (2016) 1–8. doi:10.1042/EBC20150001.

[44] T.M. Swager, K.A. Mirica, Introduction: Chemical Sensors, Chem. Rev. 119 (2019) 1–2. doi:10.1021/acs.chemrev.8b00764.

[45] D.R. Thvenot, K. Toth, R.A. Durst, G.S. Wilson, Electrochemical

biosensors: Recommended definitions and classification (Technical Report), Pure Appl. Chem. 71 (1999) 2333–2348. doi:10.1351/pac199971122333.

[46] E.O. Polat, M.M. Cetin, A.F. Tabak, E.B. Güven, B.Ö. Uysal, T. Arsan, A. Kabbani, H. Hamed, S.B. Gül, Transducer Technologies for Biosensors and Their Wearable Applications, Biosensors. 12 (2022). doi:10.3390/bios12060385.

[47] K.K. Gangu, S. Maddila, S.B. Mukkamala, S.B. Jonnalagadda, A review on contemporary Metal-Organic Framework materials, Inorganica Chim. Acta. 446 (2016) 61–74. doi:10.1016/j.ica.2016.02.062.

[48] S. Bala, I. Mondal, A. Goswami, U. Pal, R. Mondal, Co-MOF as a sacrificial template: Manifesting a new Co3O4/TiO2 system with a p-n heterojunction for photocatalytic hydrogen evolution, J. Mater. Chem. A. 3 (2015) 20288–20296. doi:10.1039/c5ta05210f.

[49] R. Liu, T. Yu, Z. Shi, Z. Wang, The preparation of metal-organic frameworks and their biomedical application, Int. J. Nanomedicine. 11 (2016) 1187–1200. doi:10.2147/IJN.S100877.

[50] R. V. Jagadeesh, K. Murugesan, A.S. Alshammari, H. Neumann, M.M. Pohl, J. Radnik, M. Beller, MOF-derived cobalt nanoparticles catalyze a general synthesis of amines, Science (80-.). 358 (2017) 326–332. doi:10.1126/science.aan6245.

[51] M. Sanchez-Sala, O. Vallcorba, C. Domingo, J.A. Ayllón, Acetic acid as a solvent for the synthesis of metal–organic frameworks based on trimesic acid, Polyhedron. 170 (2019) 458–462. doi:10.1016/j.poly.2019.06.017.

[52] F.H. Wei, D. Chen, Z. Liang, S.Q. Zhao, Y. Luo, Synthesis and characterization of metal-organic frameworks fabricated by microwave-assisted ball milling for adsorptive removal of Congo red from aqueous solutions, RSC Adv. 7 (2017) 46520–46528. doi:10.1039/c7ra09243a.

[53] X.X. Wang, B. Yu, K. Van Hecke, G.H. Cui, Four cobalt(II) coordination polymers with diverse topologies derived from flexible bis(benzimidazole) and aromatic dicarboxylic acids: Syntheses, crystal structures and catalytic properties, RSC Adv. 4 (2014) 61281–61289. doi:10.1039/c4ra08138b.

[54] M.D. Allendorf, A. Schwartzberg, V. Stavila, A.A. Talin, A roadmap to implementing metal-organic frameworks in electronic devices: Challenges and critical directions, Chem. - A Eur. J. 17 (2011) 11372–11388. doi:10.1002/chem.201101595.

[55] V. Stavila, A.A. Talin, M.D. Allendorf, MOF-based electronic and opto-electronic devices, Chem. Soc. Rev. 43 (2014) 5994–6010. doi:10.1039/c4cs00096j.

[56] J. Guo, Y. Li, Y. Cheng, L. Dai, Z. Xiang, Highly Efficient Oxygen Reduction Reaction Electrocatalysts Synthesized under Nanospace

Confinement of Metal-Organic Framework, ACS Nano. 11 (2017) 8379–8386. doi:10.1021/acsnano.7b03807.

[57] M. Saraf, R. Rajak, S.M. Mobin, MOF Derived High Surface Area Enabled Porous Co3O4 Nanoparticles for Supercapacitors, ChemistrySelect. 4 (2019) 8142–8149. doi:10.1002/slct.201901652.

[58] J. Liu, B. Lukose, O. Shekhah, H.K. Arslan, P. Weidler, H. Gliemann, S. Bräse, S. Grosjean, A. Godt, X. Feng, K. Müllen, I.B. Magdau, T. Heine, C. Wöll, A novel series of isoreticular metal organic frameworks: Realizing metastable structures by liquid phase epitaxy, Sci. Rep. 2 (2012) 1–5. doi:10.1038/srep00921.

[59] J.F. Kurisingal, R. Babu, S.H. Kim, Y.X. Li, J.S. Chang, S.J. Cho, D.W. Park, Microwave-induced synthesis of a bimetallic charge-transfer metal organic framework: A promising host for the chemical fixation of CO2, Catal. Sci. Technol. 8 (2018) 591–600. doi:10.1039/c7cy02063e.

[60] W. Guo, W. Sun, L.P. Lv, S. Kong, Y. Wang, Microwave-Assisted Morphology Evolution of Fe-Based Metal-Organic Frameworks and Their Derived Fe2O3 Nanostructures for Li-Ion Storage, ACS Nano. 11 (2017) 4198–4205. doi:10.1021/acsnano.7b01152.

[61] C.P. Raptopoulou, Metal-organic frameworks: Synthetic methods and potential applications, Materials (Basel). 14 (2021) 1–32. doi:10.3390/ma14020310.

[62] M. Henary, C. Kananda, L. Rotolo, B. Savino, E.A. Owens, G.

Cravotto, Benefits and applications of microwave-assisted synthesis of nitrogen containing heterocycles in medicinal chemistry, RSC Adv. 10 (2020) 14170–14197. doi:10.1039/d0ra01378a.

[63] E.F. and R.M. Sofia Henriques Ferreira, Ana Rovisco, Andreia dos Santos, Hugo Águas, Rui Igreja, Pedro Barquinha, Porous ZnO Nanostructures Synthesized by Microwave Hydrothermal Method for Energy Harvesting Applications, IntechOpen. (2021). https://www.intechopen.com/books/advanced-biometric-technologies/liveness-detection-in-biometrics.

[64] Y. Zhu, P. Su, J. Wang, X. Wang, Research Progress on Metal–Organic Framework-Based Electrode Materials for Supercapacitors, Crystals. 13 (2023). doi:10.3390/cryst13111593.

[65] Y.Z. Chen, R. Zhang, L. Jiao, H.L. Jiang, Metal–organic framework-derived porous materials for catalysis, Coord. Chem. Rev. 362 (2018) 1–23. doi:10.1016/j.ccr.2018.02.008.

[66] S. Goma, C.K. Mahadevan, Purity and properties of spherical shaped Co3O4 nanocrystals prepared by a polyol route using a domestic microwave oven, Next Mater. 1 (2023) 100020. doi:10.1016/j.nxmate.2023.100020.

[67] M.G. Kim, Y.H. Choi, Electrocatalytic Properties of Co3O4 Prepared on Carbon Fibers by Thermal Metal–Organic Deposition for the Oxygen Evolution Reaction in Alkaline Water Electrolysis,

Nanomaterials. 13 (2023). doi:10.3390/nano13061021.

[68] A.A. Vodyashkin, P. Kezimana, F.Y. Prokonov, I.A. Vasilenko, Y.M. Stanishevskiy, Current Methods for Synthesis and Potential Applications of Cobalt Nanoparticles: A Review, Crystals. 12 (2022). doi:10.3390/cryst12020272.

[69] S.G. Peera, R. Koutavarapu, C. Liu, G. Rajeshkhanna, A. Asokan, C.V. Reddy, Cobalt nanoparticle-embedded nitrogen-doped carbon catalyst derived from a solid-state metal-organic framework complex for oer and her electrocatalysis, Energies. 14 (2021). doi:10.3390/en14051320.

[70] A. Ejsmont, T. Darvishzad, G. Słowik, P. Stelmachowski, J. Goscianska, Cobalt-based MOF-derived carbon electrocatalysts with tunable architecture for enhanced oxygen evolution reaction, J. Colloid Interface Sci. 653 (2024) 1326–1338. doi:10.1016/j.jcis.2023.09.172.

[71] M.A. Riaz, Z. Yuan, A. Mahmood, F. Liu, X. Sui, J. Chen, Q. Huang, X. Liao, L. Wei, Y. Chen, Hierarchically porous carbon nanofibers embedded with cobalt nanoparticles for efficient H2O2 detection on multiple sensor platforms, Sensors Actuators, B Chem. 319 (2020) 128243. doi:10.1016/j.snb.2020.128243.

[72] J.L.C. Rowsell, O.M. Yaghi, Effects of functionalization, catenation, and variation of the metal oxide and organic linking units on the low-pressure hydrogen adsorption properties of metal-organic

frameworks, J. Am. Chem. Soc. 128 (2006) 1304–1315. doi:10.1021/ja056639q.

[73] M. Ding, W. Shi, L. Guo, Z.Y. Leong, A. Baji, H.Y. Yang, Bimetallic metal-organic framework derived porous carbon nanostructures for high performance membrane capacitive desalination, J. Mater. Chem. A. 5 (2017) 6113–6121. doi:10.1039/c7ta00339k.

[74] K. Sathiyan, A. Dutta, V. Marks, O. Fleker, T. Zidki, R.D. Webster, A. Borenstein, Nano-encapsulation: overcoming conductivity limitations by growing MOF nanoparticles in meso-porous carbon enables high electrocatalytic performance, NPG Asia Mater. 15 (2023). doi:10.1038/s41427-022-00459-4.

[75] M. Trukawka, K. Cendrowski, M. Peruzynska, A. Augustyniak, P. Nawrotek, M. Drozdzik, E. Mijowska, Carbonized metal–organic frameworks with trapped cobalt nanoparticles as biocompatible and efficient azo-dye adsorbent, Environ. Sci. Eur. 31 (2019). doi:10.1186/s12302-019-0242-9.

[76] M. Hao, M. Qiu, H. Yang, B. Hu, X. Wang, Recent advances on preparation and environmental applications of MOF-derived carbons in catalysis, Sci. Total Environ. 760 (2021) 143333. doi:10.1016/j.scitotenv.2020.143333.

[77] M.A. Ahsan, O. Fernandez-Delgado, E. Deemer, H. Wang, A.A. El-Gendy, M.L. Curry, J.C. Noveron, Carbonization of Co-BDC MOF

results in magnetic C@Co nanoparticles that catalyze the reduction of methyl orange and 4-nitrophenol in water, J. Mol. Liq. 290 (2019) 111059. doi:10.1016/j.molliq.2019.111059.

[78] W. Liao, W. Wu, G. Zhong, S. Zhang, J. Song, X. Fu, S.M. Huang, S. Zheng, Y. Xu, H.Y. Su, Cobalt nanoparticles encapsulated in Nitrogen-Doped carbons derived from Co-Metal-Organic frameworks with superb adsorption capacity for tetracycline, Sep. Purif. Technol. 326 (2023). doi:10.1016/j.seppur.2023.124793.

[79] J. Lu, Y. Zeng, X. Ma, H. Wang, L. Gao, H. Zhong, Q. Meng, Cobalt nanoparticles embedded into N-doped carbon from metal organic frameworks as highly active electrocatalyst for oxygen evolution reaction, Polymers (Basel). 11 (2019). doi:10.3390/polym11050828.

[80] E. Dai, J. Xu, J. Qiu, S. Liu, P. Chen, Y. Liu, Co@Carbon and Co 3 O4@Carbon nanocomposites derived from a single MOF for supercapacitors, Sci. Rep. 7 (2017) 1–11. doi:10.1038/s41598-017-12733-5.

[81] O. Mykhailiv, H. Zubyk, K. Brzezinski, M. Gras, G. Lota, M. Gniadek, E. Romero, L. Echegoyen, M.E. Plonska-Brzezinska, Improvement of the Structural and Chemical Properties of Carbon Nano-onions for Electrocatalysis, ChemNanoMat. 3 (2017) 583–590. doi:10.1002/cnma.201700161.

[82] J.K. McDonough, Y. Gogotsi, Carbon onions: Synthesis and

electrochemical applications, Electrochem. Soc. Interface. 22 (2013) 61–66. doi:10.1149/2.F05133if.

[83] S. Kaur, A. Krishnan, S. Chakraborty, Recent advances and challenges of carbon nano onions (CNOs) for application in supercapacitor devices (SCDs), J. Energy Storage. 71 (2023) 107928. doi:10.1016/j.est.2023.107928.

[84] A.V. Ramya, R. Thomas, M. Balachandran, Mesoporous onion-like carbon nanostructures from natural oil for high-performance supercapacitor and electrochemical sensing applications: Insights into the post-synthesis sonochemical treatment on the electrochemical performance, Ultrason. Sonochem. 79 (2021) 105767. doi:10.1016/j.ultsonch.2021.105767.

[85] A.C. Loanda R. Cumba, and R.J.F. , Silvia Giordani, Electrochemical Properties of Screen-Printed Carbon Nano-Onion Electrodes, Molecules. 25 (2020). doi:10.3390/molecules25173884.

[86] M.E. Plonska-Brzezinska, Carbon Nano-Onions: A Review of Recent Progress in Synthesis and Applications, ChemNanoMat. 5 (2019) 568–580. doi:10.1002/cnma.201800583.

[87] D.M. Bobrowska, P. Olejnik, L. Echegoyen, M.E. Plonska-Brzezinska, Onion-Like Carbon Nanostructures: An Overview of Bio-Applications, Curr. Med. Chem. 26 (2018) 6896–6914. doi:10.2174/0929867325666181101105535.

[88] M. Zeiger, N. Jäckel, V.N. Mochalin, V. Presser, Review: Carbon onions for electrochemical energy storage, J. Mater. Chem. A. 4 (2016) 3172–3196. doi:10.1039/c5ta08295a.

[89] J. Bartelmess, S. Giordani, Carbon nano-onions (multi-layer fullerenes): Chemistry and applications, Beilstein J. Nanotechnol. 5 (2014) 1980–1998. doi:10.3762/bjnano.5.207.

[90] A. Camisasca, A. Sacco, R. Brescia, S. Giordani, Boron / Nitrogen-Codoped Carbon Nano-Onion Electrocatalysts for the Oxygen Reduction Reaction, ACS Appl. Nano Mater. 1 (2018) 5763–5773. doi:doi/10.1021/acsanm.8b01430.

[91] L. Feng, N. Xie, J. Zhong, Carbon nanofibers and their composites: A review of synthesizing, properties and applications, Materials (Basel). 7 (2014) 3919–3945. doi:10.3390/ma7053919.

[92] X. Yang, Y. Chen, C. Zhang, G. Duan, S. Jiang, Electrospun carbon nanofibers and their reinforced composites: Preparation, modification, applications, and perspectives, Compos. Part B Eng. 249 (2023). doi:10.1016/j.compositesb.2022.110386.

[93] D. Yadav, F. Amini, A. Ehrmann, Recent advances in carbon nanofibers and their applications – A review, Eur. Polym. J. 138 (2020). doi:10.1016/j.eurpolymj.2020.109963.

[94] D.S. and M.J.L. Juan C. Ruiz-Cornejo, Synthesis and applications of carbon nanofibers: a review, Rev Chem Eng. (2018).

doi:doi.org/10.1515/revce-2018-0021.

[95] K.S.G. and R.J. N, Electrospinning: The Technique and Applications. Recent Developments in Nanofibers Research, IntechOpen. (2023). doi:doi.org/10.5772/intechopen.105804.

[96] T. Wang, Z. Chen, W. Gong, F. Xu, X. Song, X. He, M. Fan, Electrospun Carbon Nanofibers and Their Applications in Several Areas, ACS Omega. 8 (2023) 22316–22330. doi:10.1021/acsomega.3c01114.

[97] J. Xue, T. Wu, Y. Dai, Y. Xia, Electrospinning and electrospun nanofibers: Methods, materials, and applications, Chem. Rev. 119 (2019) 5298–5415. doi:10.1021/acs.chemrev.8b00593.

[98] W. Guo, W. Sun, Y. Wang, Multilayer CuO@NiO Hollow Spheres: Microwave-Assisted Metal-Organic-Framework Derivation and Highly Reversible Structure-Matched Stepwise Lithium Storage, ACS Nano. 9 (2015) 11462–11471. doi:10.1021/acsnano.5b05610.

[99] J.P. Perdew, K. Burke, M. Ernzerhof, Generalized gradient approximation made simple, Phys. Rev. Lett. 77 (1996) 3865–3868. doi:10.1103/PhysRevLett.77.3865.

[100] X. Qi, G. Yang, M. Jing, Q. Fu, F.C. Chiu, Microfibrillated cellulose-reinforced bio-based poly(propylene carbonate) with dual shape memory and self-healing properties, J. Mater. Chem. A. 2 (2014) 20393–20401. doi:10.1039/c4ta04954c.

[101] J. Du, R. Zhao, Z. Zhu, A facile approach for synthesis and in

situ modification of onion-like carbon with molybdenum carbide, Phys. Status Solidi Appl. Mater. Sci. 208 (2011) 878–881. doi:10.1002/pssa.201026646.

[102] F.H. Pilz, P. Kielb, Cyclic voltammetry, square wave voltammetry or electrochemical impedance spectroscopy? Interrogating electrochemical approaches for the determination of electron transfer rates of immobilized redox proteins, BBA Adv. 4 (2023) 100095. doi:10.1016/j.bbadva.2023.100095.

[103] K. Karuppasamy, R. Bose, D. Vikraman, S. Ramesh, H.S. Kim, E. Alhseinat, A. Alfantazi, H.S. Kim, Revealing the effect of various organic ligands on the OER activity of MOF-derived 3D hierarchical cobalt oxide @ carbon nanostructures, J. Alloys Compd. 934 (2023) 167909. doi:10.1016/j.jallcom.2022.167909.

[104] T. Kazda, L. Münster, B. Hanulíková, A. Stýskalík, P. Eloy, Microwave-assisted synthesis of platelet-like cobalt metal-organic framework , its transformation to porous layered cobalt-carbon nanocomposite discs and their utilization as anode materials in sodium-ion batteries Citation Permanent link This document is, (2023).

[105] M. Manjunatha, G.S. Reddy, K.J. Mallikarjunaiah, R. Damle, K.P. Ramesh, Determination of Phase Composition of Cobalt Nanoparticles Using 59Co Internal Field Nuclear Magnetic Resonance, J. Supercond. Nov. Magn. 32 (2019) 3201–3209. doi:10.1007/s10948-019-5083-7.

[106] H. Lv, X. Liang, G. Ji, H. Zhang, Y. Du, Porous three-dimensional flower-like Co/CoO and its excellent electromagnetic absorption properties, ACS Appl. Mater. Interfaces. 7 (2015) 9776–9783. doi:10.1021/acsami.5b01654.

[107] A.K. Ipadeola, R. Barik, S.C. Ray, K.I. Ozoemena, Bimetallic Pd/SnO2 Nanoparticles on Metal Organic Framework (MOF)-Derived Carbon as Electrocatalysts for Ethanol Oxidation, Electrocatalysis. 10 (2019) 366–380. doi:10.1007/s12678-019-00518-5.

[108] R. Kaur, M. Chhibber, P. Mahata, S.K. Mittal, Induction of Catalytic Activity in ZnO Loaded Cobalt Based MOF for the Reduction of Nitroarenes, ChemistrySelect. 3 (2018) 3417–3425. doi:10.1002/slct.201702703.

[109] Z.E. Brubaker, J.J. Langford, R.J. Kapsimalis, J.L. Niedziela, Quantitative analysis of Raman spectral parameters for carbon fibers: practical considerations and connection to mechanical properties, J. Mater. Sci. 56 (2021) 15087–15121. doi:10.1007/s10853-021-06225-1.

[110] Å. Björkman, Thermische Klärschlammbehandlung, Interpret. Raman Spectra Disord. Amorph. Carbon. 31 (1969) 632–645. doi:10.1007/BF02543692.

[111] A. Sadezky, H. Muckenhuber, H. Grothe, R. Niessner, U. Pöschl, Raman microspectroscopy of soot and related carbonaceous materials: Spectral analysis and structural information, Carbon N. Y. 43 (2005)

1731–1742. doi:10.1016/j.carbon.2005.02.018.

[112] Y. Liu, C. Song, G. Lv, X. Wang, N. Li, Virgin and Extracted Soots in Premixed Methane Flames: A Comparison of Surface Functional Groups, Graphitization Degree, and Oxidation Reactivity, Energy and Fuels. 31 (2017) 6413–6421. doi:10.1021/acs.energyfuels.6b03011.

[113] J. Zhu, Z. Ren, S. Du, Y. Xie, J. Wu, H. Meng, Y. Xue, H. Fu, Co-vacancy-rich Co1–xS nanosheets anchored on rGO for high-efficiency oxygen evolution, Nano Res. 10 (2017) 1819–1831. doi:10.1007/s12274-017-1511-9.

[114] N. Alotaibi, H.H. Hammud, N. Al Otaibi, S.G. Hussain, T. Prakasam, Novel cobalt–carbon@silica adsorbent, Sci. Rep. 10 (2020) 1–17. doi:10.1038/s41598-020-75367-0.

[115] X. Fan, Y. Sun, P. Ohlckers, X. Chen, Porous thin-wall hollow co3o4 spheres for supercapacitors with high rate capability, Appl. Sci. 9 (2019). doi:10.3390/app9214672.

[116] C. Alex, S.C. Sarma, S.C. Peter, N.S. John, Competing Effect of Co3+Reducibility and Oxygen-Deficient Defects Toward High Oxygen Evolution Activity in Co3O4Systems in Alkaline Medium, ACS Appl. Energy Mater. 3 (2020) 5439–5447. doi:10.1021/acsaem.0c00297.

[117] X. Han, G. He, Y. He, J. Zhang, X. Zheng, L. Li, C. Zhong, W. Hu, Y. Deng, T.Y. Ma, Engineering Catalytic Active Sites on Cobalt Oxide Surface for Enhanced Oxygen Electrocatalysis, Adv. Energy

Mater. 8 (2018) 1–13. doi:10.1002/aenm.201702222.

[118] J.J. Ogada, A.K. Ipadeola, P. V. Mwonga, A.B. Haruna, F. Nichols, S. Chen, H.A. Miller, M. V. Pagliaro, F. Vizza, J.R. Varcoe, D.M. Meira, D.M. Wamwangi, K.I. Ozoemena, CeO2Modulates the Electronic States of a Palladium Onion-Like Carbon Interface into a Highly Active and Durable Electrocatalyst for Hydrogen Oxidation in Anion-Exchange-Membrane Fuel Cells, ACS Catal. 12 (2022) 7014–7029. doi:10.1021/acscatal.2c01863.

[119] L. Gaolatlhe, R. Barik, S.C. Ray, K.I. Ozoemena, Voltammetric responses of porous Co3O4 spinels supported on MOF-derived carbons: Effects of porous volume on dopamine diffusion processes, J. Electroanal. Chem. 872 (2020) 113863. doi:10.1016/j.jelechem.2020.113863.

[120] A.C. De Sá, L.L. Paim, N.R. Stradiotto, New detector based on composite of carbon nanotubes with nanoparticles of cobalt oxide for carbohydrates analysis by HPLC with reverse pulsed amperometric detection, J. Braz. Chem. Soc. 31 (2020) 456–466. doi:10.21577/0103-5053.20190204.

[121] E. Delnavaz, K. Asadpour-Zeynali, Cobalt oxide nanoparticles electrodeposited on glassy carbon electrode for metronidazole determination, Results Chem. 7 (2024) 101321. doi:10.1016/j.rechem.2024.101321.

[122] A. Noorbakhsh, M. Mirkalaei, M.H. Yousefi, Electrodeposition of Cobalt Oxide Nanostructure on the Glassy Carbon Electrode for Electrocatalytic Determination of para -Nitrophenol, (2014) 2716–2726. doi:10.1002/elan.201400386.

[123] S. Lisnund, V. Blay, P. Muamkhunthod, K. Thunyanon, J. Pansalee, J. Monkrathok, P. Maneechote, K. Chansaenpak, P. Pinyou, Electrodeposition of Cobalt Oxides on Carbon Nanotubes for Sensitive Bromhexine Sensing, (2022) 1–12.

[124] H.H. Hammud, N. Alotaibi, N. Al Otaibi, A. Aljaafari, F. Ahmed, A. Azam, T. Prakasam, Hierarchical porous carbon cobalt nanocomposites-based sensor for fructose, Chemosensors. 9 (2021) 1–19. doi:10.3390/chemosensors9010006.

[125] M. Shumba, T. Nyokong, Characterization and Electrocatalytic Activity of Nanocomposites Consisting of Nanosized Cobalt Tetraaminophenoxy Phthalocyanine, Multi-walled Carbon Nanotubes and Gold Nanoparticles, Electroanalysis. 28 (2016) 1478–1488. doi:10.1002/elan.201501058.

[126] L. Gaolathle, Electrochemistry of cobalt (II , III) oxide on metal organic framework (MOF) -derived porous carbons for the detection of dopamine Lesego Gaolatlhe, University of the witwatersand, 2020.

[127] D.G. Lim, K.H. Kim, E. Kang, S.H. Lim, J. Ricci, S.K. Sung, M.T. Kwon, S.H. Jeong, Comprehensive evaluation of carboxylated

nanodiamond as a topical drug delivery system, Int. J. Nanomedicine. 11 (2016) 2381–2395. doi:10.2147/IJN.S104859.

[128] A.R. Kirmani, W. Peng, R. Mahfouz, A. Amassian, Y. Losovyj, H. Idriss, K. Katsiev, On the relation between chemical composition and optical properties of detonation nanodiamonds, Carbon N. Y. 94 (2015) 79–84. doi:10.1016/j.carbon.2015.06.038.

[129] A. Fujimoto, Y. Yamada, M. Koinuma, S. Sato, Origins of sp3C peaks in C1s X-ray Photoelectron Spectra of Carbon Materials, Anal. Chem. 88 (2016) 6110–6114. doi:10.1021/acs.analchem.6b01327.

[130] S. Xiao, P. Xu, Q. Peng, J. Chen, J. Huang, F. Wang, N. Noor, Layer-by-layer assembly of polyelectrolyte multilayer onto PET fabric for highly tunable dyeing withwater soluble dyestuffs, Polymers (Basel). 9 (2017). doi:10.3390/polym9120735.

[131] C. Batchelor-Mcauley, L.M. Gonalves, L. Xiong, A.A. Barros, R.G. Compton, Controlling voltammetric responses by electrode modification; Using adsorbed acetone to switch graphite surfaces between adsorptive and diffusive modes, Chem. Commun. 46 (2010) 9037–9039. doi:10.1039/c0cc03961f.

[132] O.C. Ozoemena, N.S. Mathebula, T.J. Ehirim, T. Maphumulo, G.M. Valikpe, J.L. Shai, K.I. Ozoemena, Onion-like carbon re-inforced electrospun polyacrylonitrile fibres for ultrasensitive electrochemical immunosensing of Vibrio cholerae toxin, Electrochim. Acta. 356 (2020)

136816. doi:10.1016/j.electacta.2020.136816.

[133] O.C. Ozoemena, T.J. Ehirim, T. Khawula, K. Makgopa, L.J. Shai, K.I. Ozoemena, Bovine Serum Albumin-Dependent Charge-Transfer Kinetics Controls the Electrochemical Immunosensitive Detection: Vibrio cholerae as a Model Bioanalyte, Electrocatalysis. 12 (2021) 595–604. doi:10.1007/s12678-021-00673-8.

[134] B.O. Agboola, K.I. Ozoemena, Self-assembly and heterogeneous electron transfer properties of metallo-octacarboxyphthalocyanine complexes on gold electrode, Phys. Chem. Chem. Phys. 10 (2008) 2399–2408. doi:10.1039/b800611c.

[135] O.C. Ozoemena, T. Maphumulo, J.L. Shai, K.I. Ozoemena, Electrospun Carbon Nanofibers as an Electrochemical Immunosensing Platform for Vibrio cholerae Toxin: Aging Effect of the Redox Probe, ACS Omega. 5 (2020) 5762–5771. doi:10.1021/acsomega.9b03820.

[136] J. Dockter, A. Schroder, B. Eaton, A. Wang, N. Sikhamsay, L. Morales, C. Giachetti, Analytical characterization of the APTIMA® HPV Assay, J. Clin. Virol. 45 (2009) S39–S47. doi:10.1016/S1386-6532(09)70007-1.

[137] A.T. Hesselink, J. Berkhof, M.L. Van Der Salm, A.P. Van Splunter, T.H. Geelen, F.J. Van Kemenade, M.G.B. Bleeker, D.A.M. Heideman, Clinical validation of the HPV-Risk assay, a novel real-time PCR assay for detection of high-risk human papillomavirus DNA by

targeting the E7 region, J. Clin. Microbiol. 52 (2014) 890–896. doi:10.1128/JCM.03195-13.

[138] R. Wongsamart, P. Bhattarakasol, A. Chaiwongkot, D. Wongsawaeng, P.A. Okada, T. Palaga, A. Leelahavanichkul, W. Khovidhunkit, D. Dean, N. Somboonna, Multiplex recombinase polymerase amplification for high-risk and low-risk type HPV detection, as potential local use in single tube, Sci. Rep. 13 (2023) 1–11. doi:10.1038/s41598-023-28038-9.

[139] A. Wang, Y. Zhou, Y. Chen, J. Zhou, X. You, H. Liu, Y. Liu, P. Ding, Y. Qi, C. Liang, X. Zhu, Y. Zhang, E. Liu, G. Zhang, Electrochemical immunosensor for ultrasensitive detection of human papillomaviruse type 16 L1 protein based on Ag@AuNPs-GO/SPA, Anal. Biochem. 660 (2023) 114953. doi:10.1016/j.ab.2022.114953.

[140] L.D. Tran, D.T. Nguyen, B.H. Nguyen, Q.P. Do, H. Le Nguyen, Development of interdigitated arrays coated with functional polyaniline/MWCNT for electrochemical biodetection: Application for human papilloma virus, Talanta. 85 (2011) 1560–1565. doi:10.1016/j.talanta.2011.06.048.

[141] Z. Zhu, L.; Han, J.; Wang, Z.; Yin, L.; Zhang, W.; Peng, Y.; Nie, Competitive adsorption on gold nanoparticles for human papillomavirus 16 L1 protein detection by LDI-MS, Analyst. (2019) 6641–6646. doi:https://doi.org/10.1039/C9AN01612K.

[142] K.I. Ozoemena, N.S. Mathebula, J. Pillay, G. Toschi, J.A. Verschoor, Electron transfer dynamics across self-assembled N-(2-mercaptoethyl) octadecanamide/mycolic acid layers: Impedimetric insights into the structural integrity and interaction with anti-mycolic acid antibodies, Phys. Chem. Chem. Phys. 12 (2010) 345–357. doi:10.1039/b915930d.

[143] J.A. Goode, J.V.H. Rushworth, P.A. Millner, Biosensor Regeneration: A Review of Common Techniques and Outcomes, Langmuir. 31 (2015) 6267–6276. doi:10.1021/la503533g.